Étude expérimentale des mécanismes de cavitation à petite échelle

Kunpeng Long

HESAM UNIVERSITÉ

Arts et Métiers Sciences et Technologies

ÉCOLE DOCTORALE SCIENCES DES MÉTIERS DE L'INGÉNIEUR

[Laboratoire de Mécanique des Fluides de Lille – Campus de Lille]

THÈSE

présentée par : **Kunpeng LONG**

soutenue le : **13 Décembre 2022**

pour obtenir le grade de : **Docteur d'HESAM Université**

préparée à : **École Nationale Supérieure d'Arts et Métiers**

Spécialité : **Génie énergétique**

Étude expérimentale des mécanismes de cavitation à petite échelle

THÈSE dirigée par :
[M. COUTIER-DELGOSHA Olivier]

et co-encadrée par :
[Mme. BAYEUL-LAINE Annie-Claude]

Jury

M. Matevž DULAR,	Professeur, Université de Ljubljana	Rapporteur（Président）
M. Antoine DUCOIN,	Maître de Conférences HDR Ecole Centrale de Nantes/Laboratoire LHEEA	Rapporteur
Mme. Amélie DANLOS,	Maîtresse de Conférences, CNAM / Laboratoire LIFSE	Examinatrice
Mme. Shuhong LIU,	Professeure, Tsinghua Université	Examinatrice
Mme. Annie-Claude Bayeul-Lainé,	Maîtresse de Conférences HDR Émérite Arts et Métiers ParisTech / LMFL	Examinatrice
M. Olivier COUTIER-DELGOSHA,	Professeur, Arts et Métiers ParisTech/LMFL	Examinateur

THÈSE

ACKNOWLEDGMENTS

I want to, first of all, express my gratitude to my advisor, Dr. Olivier Coutier-Delgosha, for introducing me to this field of research. His invaluable guidance on the way to develop the work, his patience when I have difficulties, his experience of both academia and experimental that he is willing to share with me, and his warm personality felt by me all made my time in ENSAM and Virginia Tech a wonderful experience. Dr. Olivier has successfully made an experimental fluid mechanics expert out of me through five years of close cooperation. I also acknowledge that Dr. Annie-Claude Bayeul-Lainé, and Dr. Matevž Dular, Dr. Joseph Pierric provided significant help during my research.

Secondly, I wish to thank the professors who serve on my committee, Dr. Amélie Danlos, Dr. Antoine Ducoin, Dr. Shuhong Liu. I had great conversations with them when I had difficulties in research. Their insightful opinions, alerts, and instructions are undoubtedly assets to my research.

Thirdly, I want to thank my parents and my wife Yuanyuan for their great support. Although they are not able to provide me with technical help, their remote accompaniment and faith in me constitute the most powerful support I have been receiving throughout my Ph.D. life. Although they never complain, I owe them five years companion. I will give them lots of love for the rest of my life.

Finally, I want to thank the friendship I have enjoyed in Lille, Ljubljana, and Blacksburg. My colleagues in Lille, Dr. Guangjian Zhang, Dr. Lei Shi, Dr. Merouan Hamdi, Mr.Alberto Baretter, and Mr. Pierre Guiol, are very helpful when I have research and campus life difficulties. My research mate at Virginia Tech, Mr. Ben Zhao, and Dr. Ge Mingming, I will never forget the days we stay overnight for data collection. Also, I obtained lots of happiness in my friendship with Mr. Ce Zheng, Mr. Zhongshu Ren, Dr. Nan Si, and Miss. Xuning Zhao, Mr. Li Ren, Mr. Ye Wang, and Mr. Roshan Kumar Subramanian, I cherish our great friendship.

The last of the last, I want to thank my cat Xiaohua for being with me through the toughest times of the epidemic of COV-19, and I hope he is well wherever he is.

INTRODUCTION GENERALE(FRANÇAIS)

Ma thèse de doctorat présente des résultats expérimentaux qui visent à mieux comprendre le mécanisme de cavitation, avec l'objectif final de se concentrer sur la cavitation à petite échelle (c'est-à-dire à micro-échelle). Différents types d'installations expérimentales sont utilisés selon le cas, une installation de type venturi pour étudier la cavitation à grande échelle et un jet impactant une plaque plate pour étudier la cavitation à micro échelle. Les deux types d'installations sont relativement petits, avec un excellent contrôle des conditions de fonctionnement qui permet d'obtenir une assez bonne précision. La PIV et l'imagerie à grande vitesse sont utilisées pour développer de nouvelles techniques expérimentales dédiées à la mesure de la cavitation.

La principale originalité de mon travail est l'utilisation de la PIV pour la cavitation, qui conduit à une étude physique détaillée du mécanisme de cavitation par l'analyse des trois composantes des vitesses d'écoulement dans la section d'essai. Cela conduit à des investigations sur un mélange de physique de la cavitation bien connue qui confirme la précision de la mesure, mais aussi à de nouveaux concepts physiques sur ce qui se passe dans ou près des régions de vapeur, liés d'une certaine manière (mais pas seulement) à l'existence d'un jet rentrant/latéral couplé à la dynamique de la cavité. Une autre originalité est l'étude spécifique de la cavitation à petite échelle, qui est plus fondamentale, ce qui semble avoir un bon potentiel pour les recherches futures.

Le chapitre I est une introduction générale sur le phénomène de la cavitation, puis le mémoire est structuré en trois études distinctes. Le chapitre II étudie la cavitation sur une section 2D de type venturi, le chapitre III suit cette étude en se concentrant sur les effets 3D et le chapitre IV étudie la cavitation à micro-échelle. Le manuscrit se termine par une conclusion. Mon mémoire est structuré sous la forme de 3 articles scientifiques.

CONTENTS

CHAPTER I. INTRODUCTION

1. History of cavitation

Hydrodynamic cavitation is a phenomenon that specifically happens in liquid flows. It is a partial vaporization that occurs in high-speed flows, due to the pressure drop associated with local flow accelerations. In most engineering applications, cavitation has negative effects such as performance decrease, noise, vibrations, and erosion, which are extremely difficult to prevent. On the other hand, cavitation is also used as a positive phenomenon, for example in medical or chemical applications[1-4].

In the mid-18th century, the European mathematician Leonhard Euler had already theoretically demonstrated the possibility of cavitation in liquids. However, evidence of cavitation has been first reported at the end of the 19th century. Some English warships were found to speed down suddenly during some normal cruise. Once returned to the shipyard for investigation, engineers found that some blades of the propellers were damaged for some reason.

Later in 1895, English scientist Parsons built an experiment setup to observe the phenomenon of cavitation in laboratory. This was the first cavitation water tunnel experiment in the history of science. In 1897, in the scope of a collaboration with Parsons for the study of "ship propeller efficiency decrease," English scientist Barnaby named this kind of hydrodynamic phenomenon "Cavitation" by reference to the air-suction propeller study by Reynolds in 1873 and the word "cavitation" mentioned by Froude in 1887[5].

During the next century, the researchers have progressively classified cavitation into different categories, based on its cause and its aspect, such as traveling cavitation, sheet cavitation, cloud cavitation, supercavitation, or vortex cavitation. Some examples of these different patterns are shown hereafter in figure 1.1.

In most of these examples, the flow is not steady, which means that the cavitation area is submitted to some fluctuations at various scales and frequencies. In the specific case of "cloud cavitation, the so-called "sheet cavity" that develops on a solid surface is characterized by periodic

detachments of the rear part of the cavity, which are convected by the main flow before collapsing downstream.

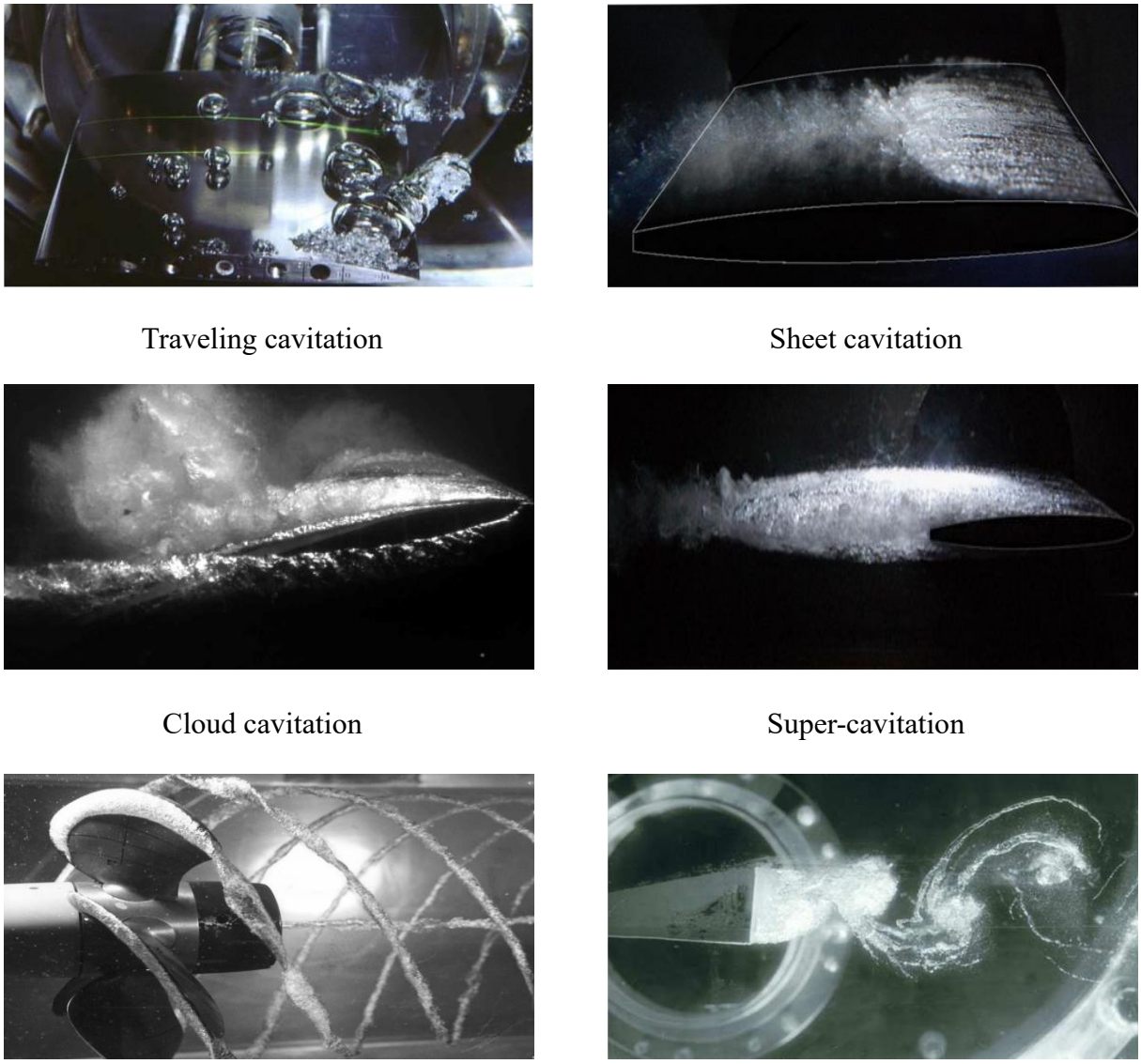

Traveling cavitation | Sheet cavitation

Cloud cavitation | Super-cavitation

Vortex cavitation | Vortex cavitation behind bluff body

Figure 1.1. Different types of cavitation

It was shown by multiple research groups in the eighties that the collapse of these clouds of vapor are strongly related to the erosion on the solid surfaces[6-10], in addition to the performance drops, noise emission and vibrations induced by the flow instabilities. It has become a recurrent issue in applications like naval propellers, pumps, and hydraulic devices in general. Although some progress

has been made in the last decades in the understanding of the erosion process and the cavitation instabilities, the mechanisms of these instabilities as well as the conditions of their development is far from being elucidated, and it is the main topic of this work.

2. Mechanisms of cavitation development

So, how exactly does cavitation occur? Like boiling, this is a liquid vaporization, but the thermodynamic processes are significantly different[1]. Cavitation is not based only on overheating but can be also generated in high speed liquid flows, especially on solid surfaces with a high local pressure gradient induced by high local speeds. So, two types of cavitation generation can be defined: superheated water cavitation and Stretched water cavitation[11].

Superheated water cavitation can generally be obtained from the following experimental methods, which were extensively used to study cavitation in water: heating in a capillary[12-15], heating in a host liquid[16-18], heat pulse[19-24], and laser induced cavitation[25-29].

Stretched water cavitation can be obtained usually from the following experimental methods: pull water[30-33], hydrodynamic flow[34-37], Berthelot method[38-40], quartz inclusions[41-44], centrifugation[45,46], shock waves[47-50], and acoustic cavitation[51-53].

The method used in this paper are hydrodynamic flow.

3. The effects of cavitation

Hydrodynamic cavitation generates various unwanted phenomena such as instabilities, noise, vibrations, and material erosion[54]. More specifically, it induces some efficiency loss in rotating machinery such as propellers, pumps, and water turbines, an increase of sonar signature for submarines and ships in general, and additional maintenance operations of hydraulic systems. Figure 1.2 shows some pictures of cavitation damage on a propeller.

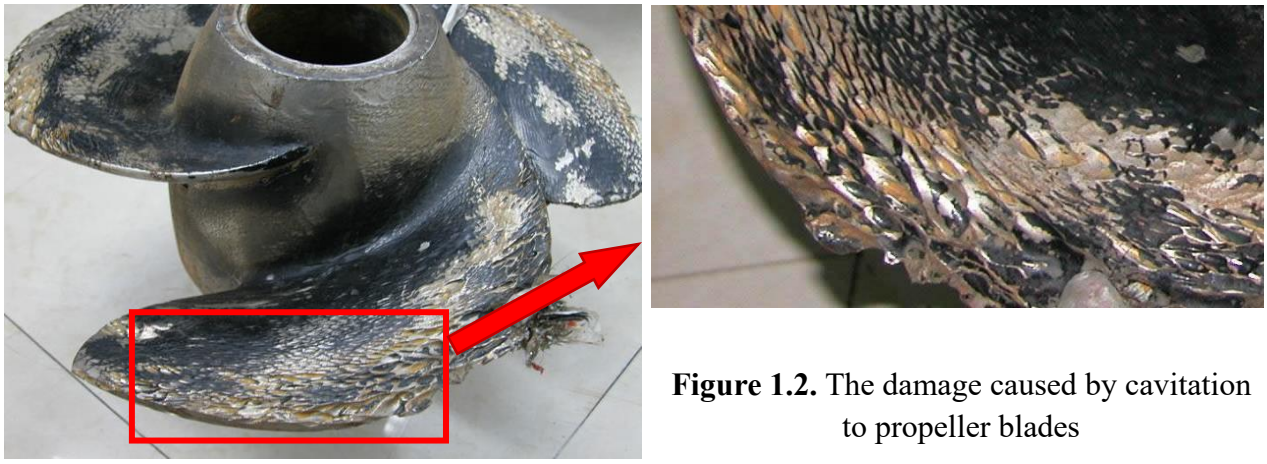

Figure 1.2. The damage caused by cavitation to propeller blades

However, cavitation also has some positive effects. In the middle of the 70s, Soviet military engineers developed a kind of super-cavitating high-velocity torpedo, which is able to accelerate up to a speed over 100 m/s, using the layer of vapor generated around the torpedo to decrease the friction with water and thus increase dramatically its speed. Typically, the use of super-cavitation enabled to reduce the resistance coefficient by a factor 10, compared to traditional torpedoes. Although it was not a successful project, it represents a milestone in the use of cavitation[55,56].

Besides, when the cavitation bubbles collapse, they generate a high pressure of several hundreds atmospheres and a high temperature that can reach several thousands of degrees, which has some applications in engineering. It can be used for example to replace some high speed liquid jets in order to increase the efficiency of cutting and cleaning solid surfaces. Besides, cavitation can also be used to increase chemical reaction rates in chemical engineering, effluent treatment, and medical treatments.

For all these reasons, studying cavitation and especially exploring the mechanisms of cloud cavitation, which is mostly involved in these different applications, is crucial to optimize the efficiency of these processes.

4. Challenges in the experimental study of cavitation

Cavitation erosion, i.e. the damage caused to the materials by the collapse of cavitation bubbles, has driven a large part of the research focused on cavitation, in the last decades[57-60]. However, many questions remain unresolved. For example, at the scale of single bubbles, each collapse is a violent

process that generates high-intensity shock waves and microjets. It is still unclear if these shock waves or the microjets are primarily responsible for the cavitation erosion. The situation is even more complex in the case of material surface damage by clouds of cavitation bubbles. Many aspects of both the bubble/material interactions and bubble/bubble interactions have not been explained yet, despite the improvements of the experimental equipment, especially the acquisition frequency of the high-speed cameras and the time response of the sensors.[61-64]

In actual flows, cavitation bubbles are extremely complex. Most of them are not spherical, due to the combined effects of pressure gradients, shear forces, and interactions with solid surfaces. As mentioned previously, in configurations of cloud cavitation they form a cloud-like structure that detaches periodically from the attached sheet cavity, and then is moved globally by the main flow, eventually generating erosion when it collapses. It is thus important, to understand and quantify erosion, to understand this collective behavior of bubbles, and the mechanisms of this flow instability. However, observing the internal structure of cavitating flows and getting some quantitative data such as velocities or pressures is a challenge, due to the opacity of cavitation, the multiple interfaces that reflect and disperse the light, the aggressiveness of the flow (erosion) that tends to break the intrusive sensors. Therefore, the studies have been limited during decades to qualitative descriptions of the macroscopic structure. At the turn of the last century, the improvement of high-speed photography, PIV technology, and the X-ray PIV techniques has enabled to observe the internal structure of cavitating flows, and obtain some quantitative information of their internal dynamics[65,66].

Another open question in cloud cavitation is the scale effects. In the 21st century, small underwater machines such as mini-submarines or diving robots have developed, and are used in various marine applications such as scientific investigations, wreck salvages, and underwear rescues. Industry also requires small-scale underwater machines, for pipeline maintenance, urban underground engineering, or for medical applications: the use of micro medical robots provides a new solution for surgeons to operate on their patients, more secure, more efficient, more accurate, and minimally invasive.

However, these applications involve cavitation at very small-scale (micrometer to millimeter),

which has received less attention over the years than cavitation at the centime or larger scale. For example, some devices require a micro propulsion system, which is powered by one or several micro propellers. Although some issues are similar to larger scales (such as efficiency loss, damage, and noise), it was also reported that cavitation at micro-scale is quite different from what happens on a large scale in terms of aspect and unsteady behavior.

5. Scale effects

The occurrence of scale effects with model tests has been reported for a long time: it was already mentioned in 1930 by Ackeret[67]. Unfortunately, there is no commonly accepted similarity law, neither for the transfer of model test results to the prototype nor for the tests of similar models investigated in different test facilities. In 1924, American scientist Thomas first suggested using a non-dimensional number to describe the state of cavitation in liquid[68]. This so-called cavitation number is usually defined as follows:

$$\sigma = \frac{p_\infty - p_\mathrm{v}}{\frac{1}{2}\rho \mathrm{u}_\infty^2}$$

with p_∞ the reference pressure in the flow field, u_∞ the reference velocity, p_v the saturated vapor pressure, and ρ the density of the liquid. This number provided a quantitative characterization of cavitation and thus facilitated the comparisons between different flow conditions. In the present work, we use mainly two non-dimensional numbers to describe cavitation: the Strouhal number (non-dimensional frequency), which characterizes the flow instabilities, and the cavitation number.

6. Proposed approach in this work

The study of cloud cavitation has shown that the periodical cloud shedding is impacted by several mechanisms, such as the re-entrant jet that flows under the sheet cavity up to its upstream, end, the bubbly condensation shock observed in some conditions in the rear part of the cavity, pressure waves travelling from downstream after the previous cloud of vapor has collapsed, or Kelvin-Helmholtz-type instabilities growing at the top interface of the cavity. The re-entrant jet is usually considered as the dominant mechanism responsible for cloud cavitation, but its actual dynamics and interaction with the incoming flow is not really understood yet. How the scale affects this process is

also unclear, despite some preliminary observations have been made by Dular et al.[36, 69], showing some similar patterns at scales between 3 millimeters and a few centimeters. However, the question of the extension of these conclusions to smaller scales, i.e. 1 millimeter and beyond, is still open.

Nowadays, both experimental works and numerical simulations are used to investigate cavitating flows and do some progress in the understanding of their physics. However, major limitations related to the modelling of turbulence, the simplifications made in the modelling of cavitation (usually based on the assumption of a homogeneous mixture with zero slip between the two phases), don't enable to use CFD to capture the detailed features related to the flow instability and draw some conclusions regarding the dominant mechanisms involved.

Experiments have beneficiated in the last decades on the improvements of the non-intrusive techniques used to measure the velocity fields, such as Particle Image Velocimetry (PIV) and Particle Tracking Velocimetry (PTV), thanks to higher frequency lasers, cameras, and also the development of new techniques based on the use of fluorescent particles in optical imaging, or other types of radiations such as x-ray imaging. However, strong limitations still apply to cavitating flows, due to the opacity of the liquid/vapor mixture, which does not enable to see the particles across the flow at a distance of more than a few millimeters.

In the present work, the use of a small-scale Venturi water channel (typically 5 mm depth) has enabled to overcome this difficulty and perform some accurate 2D3C time-resolved PIV measurements using laser illuminations, in the two phases. In other words, stereo PIV has been applied from both sides of the test section, using various filters to record both the particle motion (and get the velocity field in the liquid) and the grey level variations coming from the bubble motion (which will provide the same information for the gaseous phase). Stereo PIV performed in several vertical longitudinal planes will enable to get the 3 components of the velocity in the entire volume of the cavitating flow, and the use of high frequency lasers and cameras (from 2500 to 25,000 Hz) will enable to resolve the motion of the vapor structures.

To understand the impact of the small scale used in these experiments, a specific study has been conducted on a simpler geometry: radial cavitation in between two flat plates, resulting from the

impact of a jet on one of the plates). By changing the gap between sub-millimeter to 3 millimeters scale, the variations in the flow instabilities have been studied in detail.

7. Outline

Chapter 2 is focused on the analysis of the mechanisms of cloud cavitation in a 2D venturi type section, especially the respective dynamics of the liquid and gas phases, the various features of flow instability, and the dynamics and the structure of the re-entrant jet, using the stereo PIV in the two phases. Chapter 3 expands this analysis by investigating the role of the three-dimensional aspects of the flow field, based on the data obtained in nine different planes from the front side to the back side of the test section. After that, chapter 4 reports the analysis of the scale effects, using the measurements performed on the second device.

CHAPITRE I. INTRODUCTION(FRANÇAIS)

Dans le chapitre I, une revue de la littérature sur la cavitation sur des profils souligne la difficulté de développer des techniques expérimentales pour étudier l'effet de la cavitation sur les structures, en particulier pour la cavitation à petite échelle, où peu de littérature existe. Elle soulève également la question du mécanisme d'instabilité qui conduit aux différents types de cavitation, qui semble assez dépendant du mécanisme bien connu de la cavitation de type re-entrant. Celui-ci est sans doute très complexe à caractériser, car il peut être sujet à des interactions avec des instabilités hydrodynamiques et/ou de cavitation ainsi qu'à des interactions avec la turbulence. Il est alors nécessaire d'obtenir des mesures fines et détaillées des vitesses près de l'interface entre les régions liquide et vapeur.

1. Histoire de la cavitation

La cavitation hydrodynamique est un phénomène qui se produit spécifiquement dans les écoulements liquides. Il s'agit d'une vaporisation partielle qui se produit dans des écoulements à grande vitesse, en raison de la chute de pression associée aux accélérations locales de l'écoulement. Dans la plupart des applications techniques, la cavitation a des effets négatifs tels que la diminution des performances, le bruit, les vibrations et l'érosion, qui sont extrêmement difficiles à prévenir. D'autre part, la cavitation est également utilisée comme un phénomène positif, par exemple dans les applications médicales ou chimiques[1-4].

Au milieu du 18e siècle, le mathématicien européen Leonhard Euler avait déjà démontré théoriquement la possibilité de la cavitation dans les liquides. Cependant, les premières preuves de cavitation ont été rapportées à la fin du 19e siècle. On a constaté que certains navires de guerre anglais perdaient soudainement de la vitesse au cours d'une croisière normale. Une fois renvoyés au chantier naval pour enquête, les ingénieurs ont découvert que certaines pales des hélices étaient endommagées pour une raison quelconque.

Plus tard, en 1895, le scientifique anglais Parsons a construit une installation expérimentale pour observer le phénomène de la cavitation en laboratoire. Il s'agit de la première expérience de cavitation dans un tunnel d'eau dans l'histoire de la science. En 1897, dans le cadre d'une collaboration avec

Parsons pour l'étude de la "diminution de l'efficacité des hélices de navires", le scientifique anglais Barnaby a nommé ce type de phénomène hydrodynamique "Cavitation" en référence à l'étude sur les hélices à aspiration d'air de Reynolds en 1873 et au mot "cavitation" mentionné par Froude en 1887[5].

Au cours du siècle suivant, les chercheurs ont progressivement classé la cavitation en différentes catégories, en fonction de sa cause et de son aspect, comme la cavitation itinérante, la cavitation en nappe, la cavitation en nuage, la supercavitation ou la cavitation tourbillonnaire. Quelques exemples de ces différents modèles sont présentés dans la figure 1.1.

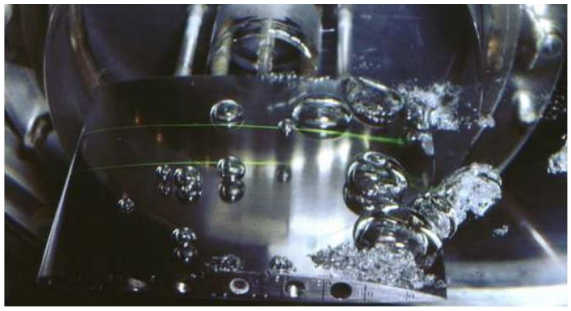

Cavitation itinérante

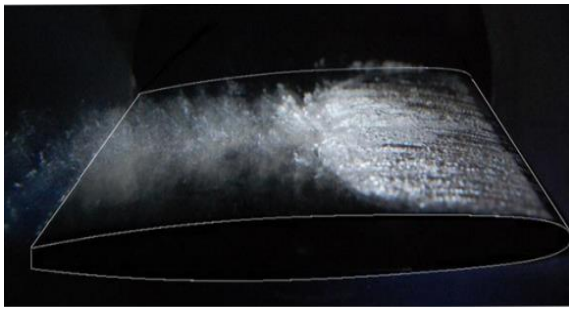

Cavitation en nappe

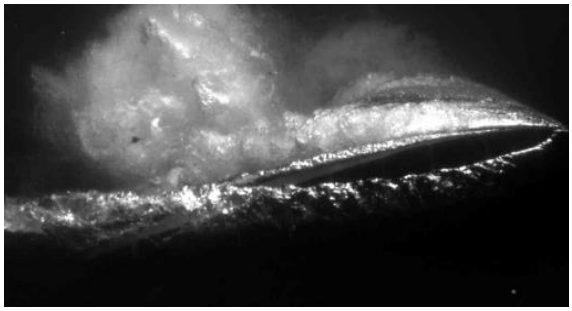

Cavitation en nuage

Super-cavitation

Cavitation tourbillonnaire

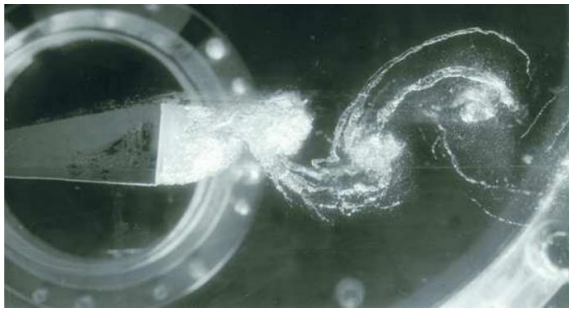

Cavitation tourbillonnaire derrière le corps de bluff

Figure 1.1. Les différents types de cavitation

Dans la plupart de ces exemples, l'écoulement n'est pas régulier, ce qui signifie que la zone de cavitation est soumise à des fluctuations à différentes échelles et fréquences. Dans le cas spécifique de la "cavitation en nuage", la "cavité en nappe" qui se développe sur une surface solide est caractérisée par des détachements périodiques de la partie arrière de la cavité, qui sont transportés par l'écoulement principal avant de s'effondrer en aval.

Il a été démontré par de nombreux groupes de recherche dans les années 80 que l'effondrement de ces nuages de vapeur est fortement lié à l'érosion des surfaces solides[6-10], en plus des baisses de performance, des émissions sonores et des vibrations induites par les instabilités de l'écoulement. C'est devenu un problème récurrent dans des applications telles que les hélices navales, les pompes et les dispositifs hydrauliques en général. Bien que certains progrès ont été réalisés au cours des dernières décennies dans la compréhension du processus d'érosion et des instabilités de cavitation, les mécanismes de ces instabilités ainsi que les conditions de leur développement sont loin d'être élucidés, et c'est le sujet principal de ce travail.

2. Mécanismes de développement de la cavitation

Alors, comment se produit exactement la cavitation comme l'ébullition, il s'agit d'une vaporisation de liquide, mais les processus thermodynamiques sont sensiblement différents[1]. La cavitation ne repose pas uniquement sur la surchauffe, mais peut également être générée dans des écoulements liquides à grande vitesse, notamment sur des surfaces solides présentant un gradient de pression local élevé induit par des vitesses locales élevées. Ainsi, deux types de génération de cavitation peuvent être définis : la cavitation par eau surchauffée et la cavitation par eau étirée[11].

La cavitation dans l'eau surchauffée peut généralement être obtenue à partir des méthodes expérimentales suivantes, qui ont été largement utilisées pour étudier la cavitation dans l'eau : chauffage dans un capillaire[12-15], chauffage dans un liquide hôte[16-18], impulsion thermique[19-24] et cavitation induite par laser[25-29].

La cavitation dans l'eau étirée peut être obtenue généralement à partir des méthodes

expérimentales suivantes : eau tirée[30-33], écoulement hydrodynamique[34-37], méthode de Berthelot[38-40], inclusions de quartz[41-44], centrifugation[45,46], ondes de choc[47-50], et cavitation acoustique[51-53].

La méthode utilisée ici est l'écoulement hydrodynamique.

3. Les effets de la cavitation

La cavitation hydrodynamique génère divers phénomènes indésirables tels que des instabilités, du bruit, des vibrations et l'érosion des matériaux[54]. Plus spécifiquement, elle induit une certaine perte d'efficacité des machines tournantes telles que les hélices, les pompes et les turbines hydrauliques, une augmentation de la signature sonar des sous-marins et des navires en général, et des opérations de maintenance supplémentaires des systèmes hydrauliques. La figure 1.2 montre quelques images de dommages causés par la cavitation sur une hélice.

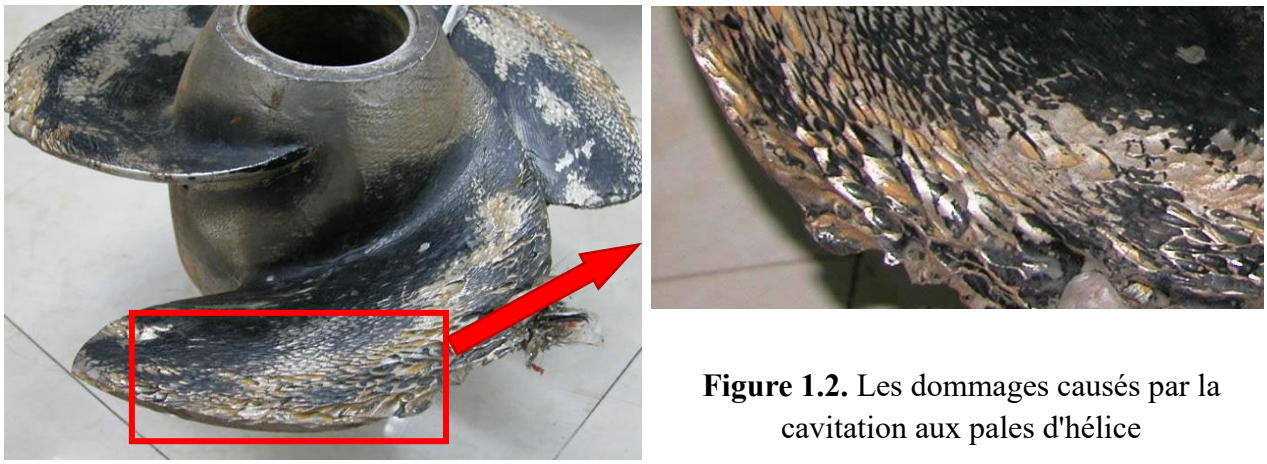

Figure 1.2. Les dommages causés par la cavitation aux pales d'hélice

Cependant, la cavitation a également des effets positifs. Au milieu des années 70, les ingénieurs militaires soviétiques ont développé une sorte de torpille super-cavitante à haute vitesse, capable d'accélérer jusqu'à une vitesse supérieure à 100 m/s, en utilisant la couche de vapeur générée autour de la torpille pour diminuer la friction avec l'eau et ainsi augmenter considérablement sa vitesse. Typiquement, l'utilisation de la super-cavitation a permis de réduire le coefficient de résistance d'un facteur 10, par rapport aux torpilles traditionnelles. Bien que ce projet n'ait pas été couronné de succès, il représente une étape importante dans l'utilisation de la cavitation[55,56].

Par ailleurs, lorsque les bulles de cavitation s'effondrent, elles génèrent une pression élevée de plusieurs centaines d'atmosphères et une température élevée pouvant atteindre plusieurs milliers de

degrés, ce qui a quelques applications en ingénierie. Elle peut être utilisée par exemple pour remplacer certains jets de liquide à grande vitesse afin d'augmenter l'efficacité de la découpe et du nettoyage des surfaces solides. En outre, la cavitation peut également être utilisée pour augmenter les taux de réaction chimique dans le génie chimique, le traitement des effluents et les traitements médicaux.

Pour toutes ces raisons, l'étude de la cavitation et en particulier l'exploration des mécanismes de la cavitation des nuages, qui est principalement impliquée dans ces différentes applications, est cruciale pour optimiser l'efficacité de ces processus.

4. Défis dans l'étude expérimentale de la cavitation

L'érosion par cavitation, c'est-à-dire les dommages causés aux matériaux par l'effondrement des bulles de cavitation, est à l'origine d'une grande partie de la recherche sur la cavitation au cours des dernières décennies[57-60]. Cependant, de nombreuses questions ne sont toujours pas résolues. Par exemple, à l'échelle des bulles individuelles, chaque effondrement est un processus violent qui génère des ondes de choc de haute intensité et des micro-jets. On ne sait toujours pas si ces ondes de choc ou les micro-jets sont les principaux responsables de l'érosion par cavitation. La situation est encore plus complexe dans le cas de l'endommagement de la surface des matériaux par des nuages de bulles de cavitation. De nombreux aspects des interactions bulle/matériau et bulle/bulle n'ont pas encore été expliqués, malgré les améliorations de l'équipement expérimental, notamment la fréquence d'acquisition des caméras à haute vitesse et la réponse temporelle des capteurs.[61-64]

Dans les écoulements réels, les bulles de cavitation sont extrêmement complexes. La plupart d'entre elles ne sont pas sphériques, en raison des effets combinés des gradients de pression, des forces de cisaillement et des interactions avec les surfaces solides. Comme mentionné précédemment, dans les configurations de cavitation en nuage, elles forment une structure en forme de nuage qui se détache périodiquement de la cavité en nappe attachée, puis est déplacée globalement par l'écoulement principal, générant finalement de l'érosion lorsqu'elle s'effondre. Il est donc important, pour comprendre et quantifier l'érosion, de comprendre ce comportement collectif des bulles, et les mécanismes de cette instabilité de l'écoulement. Cependant, observer la structure interne des écoulements cavitants et obtenir des données quantitatives telles que les vitesses ou les pressions est

un défi, en raison de l'opacité de la cavitation, des multiples interfaces qui réfléchissent et dispersent la lumière, de l'agressivité de l'écoulement (érosion) qui tend à briser les capteurs intrusifs. Par conséquent, les études ont été limitées pendant des décennies à des descriptions qualitatives de la structure macroscopique. Au début du siècle dernier, l'amélioration de la photographie à haute vitesse, de la technologie de PIV et des techniques de PIV à rayons X a permis d'observer la structure interne des écoulements cavitants et d'obtenir des informations quantitatives sur leur dynamique interne[65,66].

Une autre question ouverte dans la cavitation des nuages est celle des effets d'échelle. Au XXIe siècle, de petites machines sous-marines telles que des mini-sous-marins ou des robots de plongée se sont développées et sont utilisées dans diverses applications marines telles que les enquêtes scientifiques, le sauvetage d'épaves ... L'industrie a également besoin de machines sous-marines de petite taille, pour l'entretien des pipelines, le génie urbain souterrain, ou pour des applications médicales : l'utilisation de micro-robots médicaux offre aux chirurgiens une nouvelle solution pour opérer leurs patients, plus sûre, plus efficace, plus précise et peu invasive.

Cependant, ces applications impliquent une cavitation à très petite échelle (micromètre à millimètre), qui a reçu moins d'attention au fil des ans que la cavitation à l'échelle centimétrique ou supérieure. Par exemple, certains dispositifs nécessitent un système de micropropulsion, qui est alimenté par une ou plusieurs micro-hélices. Bien que certains problèmes soient similaires à ceux des grandes échelles (tels que la perte d'efficacité, les dommages et le bruit), il a également été signalé que la cavitation à l'échelle micro est assez différente de ce qui se passe à grande échelle en termes d'aspect et de comportement instable.

5. Effets d'échelle

L'apparition d'effets d'échelle dans les essais de modèles est signalée depuis longtemps : elle a déjà été mentionnée en 1930 par Ackeret[67]. Malheureusement, il n'existe pas de loi de similitude communément acceptée, ni pour le transfert des résultats d'essais de modèles au prototype, ni pour les essais de modèles similaires étudiés dans différentes installations d'essai. En 1924, le scientifique américain Thomas a suggéré pour la première fois d'utiliser un nombre non dimensionnel pour décrire l'état de cavitation dans un liquide[68]. Ce nombre est dit de cavitation. Il est défini comme suit:

$$\sigma = \frac{p_\infty - p_v}{\frac{1}{2}\rho u_\infty^2}$$

Ce nombre fournit une caractérisation quantitative de la cavitation et facilite ainsi les comparaisons entre différentes conditions d'écoulement. Dans le présent travail, nous utilisons principalement deux nombres non dimensionnels pour décrire la cavitation : le nombre de Strouhal (fréquence non dimensionnelle), qui caractérise les instabilités de l'écoulement, et le nombre de cavitation.

6. L'approche proposée dans ce travail

L'étude de la cavitation des nuages a montré que la perte périodique de nuages est influencée par plusieurs mécanismes, tels que le jet rentrant qui s'écoule sous la cavité de la feuille jusqu'à son extrémité amont, le choc de condensation bouillonnant observé dans certaines conditions dans la partie arrière de la cavité, les ondes de pression se déplaçant depuis l'aval après l'effondrement du nuage de vapeur précédent, ou les instabilités de type Kelvin-Helmholtz se développant à l'interface supérieure de la cavité. Le jet rentrant est généralement considéré comme le mécanisme dominant responsable de la cavitation des nuages, mais sa dynamique réelle et son interaction avec l'écoulement entrant ne sont pas encore vraiment comprises. La façon dont l'échelle affecte ce processus n'est pas claire non plus, bien que certaines observations préliminaires aient été faites par Dular et al.[36, 69], montrant des modèles similaires à des échelles comprises entre 3 millimètres et quelques centimètres. Cependant, la question de l'extension de ces conclusions à des échelles plus petites, c'est-à-dire 1 millimètre et au-delà, reste ouverte.

Aujourd'hui, des travaux expérimentaux et des simulations numériques sont utilisés pour étudier les écoulements cavitants et faire des progrès dans la compréhension de leur physique. Cependant, les limitations majeures liées à la modélisation de la turbulence, les simplifications faites dans la modélisation de la cavitation (généralement basée sur l'hypothèse d'un mélange homogène avec un glissement nul entre les deux phases), ne permettent pas d'utiliser la CFD pour capturer les caractéristiques détaillées liées à l'instabilité de l'écoulement et tirer des conclusions concernant les mécanismes dominants impliqués.

Au cours des dernières décennies, les expériences ont bénéficié de l'amélioration des techniques non intrusives utilisées pour mesurer les champs de vitesse, telles que la vélocimétrie par image de particules (PIV) et la vélocimétrie par suivi de particules (PTV), grâce à des lasers à plus haute fréquence, des caméras, et aussi au développement de nouvelles techniques basées sur l'utilisation de particules fluorescentes en imagerie optique, ou d'autres types de radiations telles que l'imagerie par rayons X. Cependant, de fortes limitations s'appliquent encore aux écoulements cavitants, en raison de l'opacité du mélange liquide/vapeur, qui ne permet pas de voir les particules à travers l'écoulement à une distance supérieure à quelques millimètres.

Dans le présent travail, l'utilisation d'un canal d'eau Venturi à petite échelle (typiquement 5 mm de profondeur) a permis de surmonter cette difficulté et de réaliser des mesures précises de PIV 2D3C à résolution temporelle en utilisant des illuminations laser, dans les deux phases. En d'autres termes, la PIV stéréo a été appliquée des deux côtés de la section d'essai, en utilisant divers filtres pour enregistrer à la fois le mouvement des particules (et obtenir le champ de vitesse dans le liquide) et les variations de niveau de gris provenant du mouvement des bulles (qui fourniront les mêmes informations pour la phase gazeuse). La PIV stéréo réalisée dans plusieurs plans verticaux longitudinaux permettra d'obtenir les 3 composantes de la vitesse dans tout le volume de l'écoulement cavitant, et l'utilisation de lasers et de caméras haute fréquence (de 2500 à 25 000 Hz) permettra de résoudre le mouvement des structures de vapeur.

Pour comprendre l'impact de la petite échelle utilisée dans ces expériences, une étude spécifique a été menée sur une géométrie plus simple : la cavitation radiale entre deux plaques plates, résultant de l'impact d'un jet sur l'une des plaques). En changeant l'écart entre l'échelle sub-millimétrique et l'échelle de 3 millimètres, les variations des instabilités de l'écoulement ont été étudiées en détail.

7. Plan d'ensemble

Le chapitre 2 est consacré à l'analyse des mécanismes de la cavitation d'un nuage dans une section 2D de type venturi, en particulier la dynamique respective des phases liquide et gazeuse, les différentes caractéristiques de l'instabilité de l'écoulement, et la dynamique et la structure du jet rentrant, en utilisant la PIV stéréo dans les deux phases. Le chapitre 3 élargit cette analyse en étudiant

le rôle des aspects tridimensionnels du champ d'écoulement, sur la base des données obtenues dans neuf plans différents, de l'avant à l'arrière de la section d'essai. Ensuite, le chapitre 4 rapporte l'analyse des effets d'échelle, en utilisant les mesures effectuées sur le second dispositif.

References

[1] C.E. Brennen, Cavitation and Bubble Dynamics, Oxford University Press, Oxford, 1995.

[2] T.G. Leighton, The Acoustic Bubble, Academic Press, London, 1994.

[3] F.R. Young, Cavitation, McGraw-Hill, London, 1989.

[4] Milton S. Plesset& Andrea Prosperetti, Bubble Dynamics and Cavitation, Ann. Rev. Fluid Mech. 1977.9: 145-85

[5] Weitendorf E A. On the history of propeller cavitation and cavitation tunnels[C]//Fourth International Symposium on Cavitation. Pasadena: California Institute of Technology, 2001.

[6] Bark G, Berlekom W B V. Experimental investigations of cavitation dynamics and cavitation noise[R]. SWEDISH STATE SHIPBUILDING EXPERIMENTAL TANK GOETEBORG, 1979.

[7] Shen Y T, Peterson F B. Unsteady Cavitation on an Oscillating Hydrofoil[R]. DAVID W TAYLOR NAVAL SHIP RESEARCH AND DEVELOPMENT CENTER BETHESDA MD SHIP PERFORMANCE DEPT, 1978.

[8] Franc J P, Michel J M. Unsteady attached cavitation on an oscillating hydrofoil[J]. Journal of Fluid Mechanics, 1988, 193: 171-189.

[9] Kubota A, Kato H, Yamaguchi H, et al. Unsteady structure measurement of cloud cavitation on a foil section using conditional sampling technique[J]. 1989.

[10] Kubota A, Kato H, Yamaguchi H. Finite difference analysis of unsteady cavitation on a two-dimensional hydrofoil[C]//International Conference on Numerical Ship Hydrodynamics, 5th. 1989.

[11] Caupin F, Herbert E. Cavitation in water: a review[J]. Comptes Rendus Physique, 2006, 7(9-10): 1000-1017.

[12] J.-A. De Luc, Introduction à la physique terrestre par les fluides expansibles, Paris, 1803, p. 93.

[13] F. Donny, Mémoire sur la cohésion des liquides, et sur leur adhérence aux corps solides, Ann. Chim. Phys. 16 (1846) 167–190.

[14] F.B. Kenrick, C.S. Gilbert, K.L. Wismer, The superheating of liquids, J. Phys. Chem. 28 (1924) 1297–1307.

[15] L.J. Briggs, Maximum superheating of water as a measure of negative pressure, J. Appl. Phys.

26 (1955) 1001–1003.

[16] H. Wakeshima, K. Takata, On the limit of superheat, J. Phys. Soc. Japan 13 (1958) 1398–1403.

[17] R.E. Apfel, Vapor nucleation at a liquid–liquid interface, J. Chem. Phys. 54 (1971) 62–63.

[18] R.E. Apfel, Water superheated to 279.5 ◦C at atmospheric pressure, Nature Phys. Sci. 238 (1972) 63–64.

[19] P.A. Pavlov, V.P. Skripov, Kinetics of spontaneous nucleation in strongly heated liquids, High Temp. (USSR) 8 (1970) 540–545; translated from Teplofiz. Vys. Temp. 8 (1970) 579–585.

[20] K.P. Derewnicki, Experimental studies of heat transfer and vapour formation in fast transient boiling, Int. J. Heat. Mass Trans. 28 (1985) 2085–2092.

[21] S. Glod, D. Poulikakos, Z. Zhao, G. Yadigaroglu, An investigation of microscale explosive vaporization of water on an ultrathin Pt wire, Int. J. Heat. Mass Trans. 45 (2002) 367–379.

[22] O.C. Thomas, R.E. Cavicchi, M.J. Tarlov, Effect of surface wettability on fast transient microboiling behavior, Langmuir 19 (2003) 6168–6177.

[23] C.T. Avedisian, W.S. Osborne, F.D. McLeod, C.M. Curley, Measuring bubble nucleation temperature on the surface of a rapidly heated thermal ink-jet heater immersed in a pool of water, Proc. R. Soc. London A 455 (1999) 3875–3899.

[24] K. Okuyama, S. Tsukahara, N. Morita, Y. Iida, Transient behavior of boiling bubbles generated on the small heater of a thermal ink jet printhead, Exp. Therm. Fluid Sci. 28 (2004) 825–834.

[25] P. Kafalas, A.P. Ferdinand Jr., Fog droplet vaporization and fragmentation by a 10.6-μm laser pulse, Appl. Opt. 12 (1973) 29–33.

[26] R.G. Pinnick, A. Biswas, R.L. Armstrong, S.G. Jennings, J.D. Pendleton, G. Fernandez, Micron-sized droplets irradiated with a pulsed CO2 laser: measurement of explosion and breakdown thresholds, Appl. Opt. 29 (1990) 918–925.

[27] O. Yavas, P. Leiderer, H.K. Park, C.P. Grigoropoulos, C.C. Poon, W.P. Leung, N. Do, A.C. Tam, Optical reflectance and scattering studies of nucleation and growth of bubbles at a liquid–solid interface induced by pulsed laser heating, Phys. Rev. Lett. 70 (1993) 1830–1833.

[28] H.K. Park, C.P. Grigoropoulos, C.C. Poon, A.C. Tam, Optical probing of the temperature transients during pulsed–laser induced boiling of liquids, Appl. Phys. Lett. 68 (1996) (1993) 596–598.

[29] S.I. Kudryashov, K. Lyon, S.D. Allen, Photoacoustic study of relaxation dynamics in multibubble systems in laser-superheated water, Phys. Rev. E 73 (2006) 055301(R) (1–4).

[30] G.S. Kell, Early observations of negative pressures in liquids, Am. J. Phys. 51 (1983) 1038–1041.

[31] A.T.J. Hayward, The role of stabilized gas nuclei in hydrodynamic cavitation inception, J. Phys. D 3 (1970) 574–579.

[32] A.T.J. Hayward, Mechanical pump with a suction lift of 17 metres, Nature 225 (1970) 376–377.

[33] Coutier-Delgosha O. Temperature measurements in cavitation bubbles[C]//APS Division of Fluid Dynamics Meeting Abstracts. 2016: M1. 004.

[34] O. Reynolds, Experiments showing the boiling of water in an open tube at ordinary temperatures (1894), in: Scientific Papers on Mechanical and Physical Subject, vol. II, Cambridge Univ. Press, Cambridge, 1900–1903, pp. 578–587 (Chapter 63).

[35] J.-P. Franc, J.-M. Michel, Fundamentals of Cavitation, Kluwer Academic Publishers, Dordrecht, Boston, London, 2004.

[36] Dular M, Khlifa I, Fuzier S, et al. Scale effect on unsteady cloud cavitation[J]. Experiments in fluids, 2012, 53(5): 1233-1250.

[37] Zhang G, Khlifa I, Coutier-Delgosha O. A comparative study of quasi-stable sheet cavities at different stages based on fast synchrotron x-ray imaging[J]. Physics of Fluids, 2020, 32(12): 123316.

[38] S.J. Henderson, R.J. Speedy, A Berthelot–Bourdon tube method for studying water under tension, J. Phys. E: Sci. Instrum. 13 (1980) 778–782.

[39] S.J. Henderson, R.J. Speedy, Temperature of maximum density in water at negative pressure, J. Phys. Chem. 91 (1987) 3062–3068.

[40] K. Hiro, Y. Ohde, Y. Tanzawa, Stagnations of increasing trends in negative pressure with repeated cavitation in water/metal Berthelot tubes as a result of mechanical sealing, J. Phys. D: Appl. Phys. 36 (2003) 592–597.

[41] E. Roedder, Metastable superheated ice in liquid–water inclusions under high negative pressure, Science 155 (1967) 1413–1417.

[42] J.L. Green, D.J. Durben, G.H.Wolf, C.A. Angell, Water and solutions at negative pressure:

Raman spectroscopic study to −80 megapascals, Science 249 (1990) 649–652.

[43] A.D. Alvarenga, M. Grimsditch, R.J. Bodnar, Elastic properties of water under negative pressures, J. Chem. Phys. 98 (1993) 8392–8396.

[44] M. Takahashi, E. Izawa, J. Etou, T. Ohtani, Kinetic characteristic of bubble nucleation in superheated water using fluid inclusions, J. Phys. Soc. Japan 71 (2002) 2174–2177.

[45] L.J. Briggs, Limiting negative pressure of water, J. Appl. Phys. 21 (1950) 721–722.

[46] H.W. Strube, W. Lauterborn, Untersuchung der Kavitationskeime an der Grenzfläche Quarzglas–Wasser nach der Zentrifugenmethode, Z. Angew. Phys. 29 (1970) 349–357.

[47] S.A. Sedgewick, D.H. Trevena, Limiting negative pressure of water under dynamic stressing, J. Phys. D: Appl. Phys. 9 (1976) 1983–1990.

[48] J. Staudenraus,W. Eisenmenger, Fibre-optic probe hydrophone for ultrasonic and shock-wave measurements in water, Ultrasonics 31 (1993) 267–273.

[49] P.R.Williams, R.L.Williams, On anomalously low values of the tensile strength of water, Proc. Roy. Soc. London A 456 (2000) 1321–1332.

[50] J.M. Boteler, G.T. Sutherland, Tensile failure of water due to shock wave interactions, J. Appl. Phys. 96 (2004) 6919–6924.

[51] W.J. Galloway, An experimental study of acoustically induced cavitation in liquids, J. Acoust. Soc. Am. 26 (1954) 849–857.

[52] M. Greenspan, C.E. Tschiegg, Radiation-induced acoustic cavitation apparatus and some results, J. Res. Nat. Bur. Stand. C 71 (1967) 299–312.

[53] E. Herbert, S. Balibar, F. Caupin, Cavitation pressure in water, Phys. Rev. E 74 (2006) 041603 (1–22).

[54] Karimi A, Martin J L. Cavitation erosion of materials[J]. International Metals Reviews, 1986, 31(1): 1-26.

[55] Kadivar E, Kadivar E, Javadi K, et al. The investigation of natural super-cavitation flow behind three-dimensional cavitators: Full cavitation model[J]. Applied Mathematical Modelling, 2017, 45: 165-178.

[56] Choi J H, Penmetsa R C, Grandhi R V. Shape optimization of the cavitator for a supercavitating torpedo[J]. Structural and Multidisciplinary Optimization, 2005, 29(2): 159-167.

[57] Hobbs J. Experience with a 20-kc cavitation erosion test[M]//Erosion by cavitation or impingement. ASTM International, 1967.

[58] Thiruvengadam A. Theory of erosion[M]. Hydronautics, Incorporated, 1967.

[59] McGuinness T, Thiruvengadam A. Cavitation Erosion--Corrosion Modeling[M]. ASTM International, 1974.

[60] Knapp R T, Daily J W, HAMMITT F. G. 1970 Cavitation[J]. McGraw-Hill Book Company, London.

[61] Naude C F, Ellis A T. On the mechanism of cavitation damage by nonhemispherical cavities collapsing in contact with a solid boundary[J]. 1961.

[62] Benjamin T B, Ellis A T. The collapse of cavitation bubbles and the pressures thereby produced against solid boundaries[J]. Philosophical Transactions for the Royal Society of London. Series A, Mathematical and Physical Sciences, 1966: 221-240.

[63] Tomita Y, Shima A. Mechanisms of impulsive pressure generation and damage pit formation by bubble collapse[J]. Journal of Fluid Mechanics, 1986, 169: 535-564.

[64] Tomita Y, Shima A. High-speed photographic observations of laser-induced cavitation bubbles in water[J]. Acta Acustica united with Acustica, 1990, 71(3): 161-171.

[65] Ilyass Khlifa1, Alexandre Vabre, Marko Hočevar, Kamel Fezzaa, Sylvie Fuzier1, Olivier Roussette, Olivier Coutier-Delgosha, Fast X-ray imaging of cavitating flows, Exp Fluids (2017) 58:157

[66] G Zhang, I Khlifa, O Coutier-Delgosha, Experimental investigation of internal two-phase flow structures and dynamics of quasi-stable sheet cavitation by fast synchrotron x-ray imaging, Physics of Fluids 32 (11), 113310

[67] Ackeret J. Experimentelle und theoretische Untersuchungen über Hohlraumbildung (Kavitation) im Wasser[J]. Technische Mechanik und Thermodynamik, 1930, 1(1): 1-22.

[68] H Fujita, H Perez-Meana, Cavitation Flow Simulation and Experiment Research in Inducer, IOS Press, Amsterdam, 2021

[69] Dular M, Bachert R. The issue of Strouhal number definition in cavitating flow[J]. Journal of Mechanical Engineering, 2009, 55(11): 666-674.

CHAPTER II. ANALYSIS OF THE CAVITATION INSTABILITIES WITH TIME-RESOLVED STEREO AND MULTIPLANE PARTICLE IMAGE VELOCIMETRY

Kunpeng Long[1], *Olivier Coutier-Delgosha[1, 2], Mingming Ge[2], Annie-Claude Bayeul-Lainé[1]

[1] *Univ. Lille, CNRS, ONERA, Arts et Metiers Institute of Technology, Centrale Lille, UMR 9014 - LMFL - Laboratoire de Mécanique des Fluides de Lille - Kampé de Fériet, F-59000 Lille, France*

[2] *Virginia Tech, Kevin T. Crofton Dept of Aerospace & Ocean Eng., Blacksburg VA 24060, USA*

Abstract

The present paper is devoted to the analysis of the various instabilities of cavitation attached to a two-dimensional (2D) profile. Time resolved stereo Particle Image Velocimetry (PIV) was conducted in a small-scale 2D venturi type section, in different vertical planes in the streamwise direction, located at varying positions in the depth of the channel. These experiments enabled to obtain the time evolution of the three components of the velocity field in the cavitation area, and to derive the time-averaged gradients in the spanwise direction. Test cases at various Reynolds number were conducted, maintaining either the pressure or the cavitation number constant, to discuss the impact of these parameters on the flow. Then, the attention was focused on three distinct flow dynamics, namely sheet cavitation, where no large-scale instability can be detected, single cloud cavitation, where a large cloud of vapor is shed periodically at the rear of the cavity, and multi-cloud cavitation, where the process is more complex, as more than one clouds are shed downstream. The data reveal that the structure of the re-entrant jet, which is one of the primary mechanisms of cloud cavitation, is more complex than reported in the previous studies. Although the jet can be detected as an intermittent low speed reverse flow in the streamwise direction, it is actually made of successive vortices along the channel depth, which are convected downstream while expanding in the vertical direction, causing the cavity lift and thus contributing to its final split and the cloud shedding.

Keywords: Cavitation, instability, flow imaging, PIV, re-entrant jet

Chapitre II. Analyse des instabilites de cavitation a l'aide de la velocimetrie par images de

* Corresponding author, ocoutier@vt.edu

particules stereo et multiplans resolue dans le temps(Français)

Le deuxième chapitre traite de l'analyse physique de la cavitation sur une section de test 2D de type venturi en utilisant la PIV, qui permet d'obtenir un niveau de détail assez élevé de l'écoulement à l'intérieur des régions de cavitation. Trois types de cavitations sont obtenus, de la cavitation en nappe à la cavitation simple et multi-nuages. La revue de la littérature met en évidence la difficulté de mesurer la vitesse à l'intérieur de la cavité en feuille/des bulles avec les techniques expérimentales existantes classiquement utilisées. Bien que la combinaison des techniques X-ray et PIV ait permis d'étudier le mécanisme de cavitation, la mesure de l'ensemble de l'écoulement pour les deux phases reste un défi, ce qui amène à l'originalité du travail qui est capable par la combinaison de 2 ensembles distincts de caméras de mesurer les vitesses du liquide et du gaz.

Ce chapitre a fait l'objet d'un article de journal : » *Kunpeng Long, Olivier Coutier-Delgosha, Mingming Ge, Annie-Claude Bayeul-Lainé, Analysis of the cavitation instabilities with time-resolved stereo and multiplane Particle Image Velocimetry Physics of Fluids (in press) (2022); Accepted Manuscript Online: 28 November 2022,* https://doi.org/10.1063/5.0126317

Résumé*:*

Le présent article est consacré à l'analyse des différentes instabilités de cavitation attachées à un profil bidimensionnel (2D). Une vélocimétrie par images de particules (PIV) stéréo résolue dans le temps a été réalisée dans une petite section 2D de type venturi, dans différents plans verticaux dans le sens du courant, situés à des positions variables dans la profondeur du canal. Ces expériences ont permis d'obtenir l'évolution temporelle des trois composantes du champ de vitesse dans la zone de cavitation, et de dériver les gradients moyennés dans le sens de l'envergure. Des cas d'essai à différents nombres de Reynolds ont été réalisés, en maintenant constante la pression ou le nombre de cavitation, afin de discuter de l'impact de ces paramètres sur l'écoulement. Ensuite, l'attention a été portée sur trois dynamiques d'écoulement distinctes, à savoir la cavitation en nappe, où aucune instabilité à grande échelle ne peut être détectée, la cavitation à nuage unique, où un grand nuage de vapeur est déversé périodiquement à l'arrière de la cavité, et la cavitation à nuages multiples, où le processus est plus complexe, car plusieurs nuages sont déversés en aval. Les données révèlent que la

structure du jet rentrant, qui est l'un des principaux mécanismes de la cavitation nuageuse, est plus complexe que celle rapportée dans les études précédentes. Bien que le jet puisse être détecté comme un écoulement inverse intermittent à faible vitesse dans le sens du courant, il est en fait constitué de tourbillons successifs autour de la profondeur du canal, qui sont convexes en aval tout en se dilatant dans la direction verticale, provoquant le soulèvement de la cavité et contribuant ainsi à sa division finale et au déversement des nuages.

Conclusions :

Dans cet article, la structure et l'instabilité des écoulements cavitants formés dans la partie divergente d'un venturi bidimensionnel ont été analysées en utilisant les champs de vitesse obtenus par PIV stéréo à grande vitesse. Il a été montré que malgré les petites dimensions de la section d'essai, l'écoulement est tout à fait bidimensionnel, et les champs de vitesse obtenus dans différents plans verticaux du centre au côté du canal étaient assez identiques.

L'accès à la vitesse locale de l'écoulement a permis de proposer une nouvelle définition objective de la longueur de la cavité attachée, basée sur la longueur du jet rentrant ou la valeur de la vorticité. L'importance de mesurer la pression au plus près de la zone de cavitation pour définir le nombre de cavitation a été démontrée : dans le cas présent, il s'est avéré nécessaire de prendre la moyenne des pressions amont et aval pour obtenir tous les points de données tombant sur la même courbe pour les évolutions de la longueur de la cavité ou du jet rentrant selon .

La comparaison des vitesses moyennes dans le temps du liquide et de la vapeur à différentes positions a révélé deux zones principales de vitesse de glissement significative entre les deux phases : (i) dans la moitié supérieure de la cavité de la feuille, où les plus grandes structures de vapeur ne sont pas parfaitement entraînées par l'écoulement liquide et ont une vitesse plus faible, et (ii) la zone du jet rentrant, où la nature intermittente du jet, combinée à la condensation de l'écoulement à son extrémité, entraîne des vitesses moyennes dans le temps plus importantes dans la vapeur, par rapport au liquide.

L'analyse de l'évolution temporelle de l'écoulement a permis de caractériser trois types différents

de cavitation feuille/nuage, et d'effectuer certaines caractérisations quantitatives et analyses qualitatives. Sur la base de cette étude, un aperçu de ces résultats est proposé ici, en se concentrant sur les principaux mécanismes impliqués. Comme le montre la figure 29, la cavitation des nuages est généralement divisée en quatre étapes principales : La croissance, le soulèvement, le détachement du nuage et la convection du nuage. À toutes les étapes, conformément au modèle de cellule de recirculation[13], le jet rentrant joue un rôle crucial, puisque sa structure et son élan déclenchent l'évolution de l'écoulement vers les différents comportements.

Dans le prolongement du jet rentrant lui-même, la région rentrante peut être définie comme la zone située entre la mi-hauteur de la cavité et la paroi inférieure, où la vitesse est généralement opposée à celle de l'écoulement principal, ou encore dans la même direction mais beaucoup plus faible (généralement moins de 10 % de l'écoulement liquide au-dessus de la cavité en feuille). Dans cette région, par conséquent, la forte interaction du jet rentrant avec l'écoulement principal forme un fort tourbillon près du bord d'attaque de la cavité (juste en aval de la gorge du venturi, comme le montre la figure 29a). Le frottement entre l'écoulement principal et la région rentrante induit un détachement périodique de ce tourbillon et des transferts en aval pour former une série de tourbillons dans la région rentrante. Cette série de tourbillons soulève la cavité supérieure au-dessus de la paroi inférieure, maintenant ainsi une région de cavité presque stable. C'est le premier stade de la cavitation des nuages : le stade de croissance.

Si le jet inverse disparaît (cas de l'instabilité non périodique de la figure 29c), le tourbillon au bord d'attaque de la région rentrante manque d'énergie et disparaît. Cette zone est alors comprimée par l'intrusion du flux principal et s'effondre. Au contraire, si le jet rentrant reste fort pendant un temps suffisant, le tourbillon détaché va croître de manière spectaculaire en se déplaçant vers l'aval, formant un renflement (figure 29b), qui initie la phase de soulèvement. Pendant cette phase, la vitesse globale de la région rentrante diminue en raison de la croissance du tourbillon et du renflement, pour devenir presque nulle au milieu de la cavité (sous le renflement).

Lorsque le tourbillon ou le renflement détaché croît jusqu'à une certaine échelle, il réduit la section transversale de l'écoulement liquide principal au-dessus de la cavité, ce qui augmente la

pression locale et fait dévier cet écoulement liquide vers l'espace entre ce tourbillon et le tourbillon du bord avant de la région rentrante, ce qui entraîne la formation d'une région rentrante en forme de marche. La situation de cavitation à nuage unique se produit lorsque ce mécanisme perturbe le jet rentrant en un point où aucun tourbillon du bord d'attaque de la région rentrante n'est détaché pendant une courte période. Cependant, lorsque le jet rentrant est suffisamment fort, l'action du flux principal n'est pas suffisante pour bloquer le détachement du tourbillon suivant, qui formera un deuxième tourbillon de forte intensité. Ensuite, en raison des effets de soulèvement simultanés induits par ces deux tourbillons, on obtient une structure en escalier de la région ré-entrante, comme le montre la figure 29e. Il s'agit du double détachement de nuage typique de la cavitation multi-nuages. Dans certains cas, trois nuages peuvent même apparaître simultanément, mais cette situation est rare.

Ensuite, dans les deux cas de cavitation à nuage unique et à nuages multiples, la structure en escalier est poussée vers l'aval, et une nouvelle région rentrante est créée en amont. Cette étape de "convection nuageuse" est la phase finale du cycle (figure 29f).

The dynamics of cavitating flows has been studied extensively in the last decades, to elucidate its mechanisms and be able to mitigate its adverse effects in various engineering applications, such as naval propulsion, rocket engine pumps, or industrial hydraulic systems. Most of these effects are related to the unsteady character of cavitation: the sheet cavities attached to solid bodies or walls are often characterized by periodical or non-periodical large-scale oscillations. At the same time, the collapse of the cavitation bubbles generates some large amplitude pressure waves and micro-jets, so the condensation areas are submitted to complex unsteady mechanisms involving high-pressure fluctuations[1]. It results in phenomena like vibrations, noise, erosion of solid surfaces, an increase of hydrodynamic drag, and unsteady forces potentially prejudicial for the other components of the system. In order to reduce these effects, a good understanding of the small-scale mechanisms involved in these instabilities is required.

Therefore, cavitation has been extensively studied in cavitation tunnels in configurations of simple geometries such as two-dimensional (2D) foil sections or Venturi-type sections in order to improve the knowledge about the structure of the two-phase flow and the mechanisms that control its unsteady features2-8. It is a consensus that cavitating flows are systematically unsteady at some scale, as the area of condensation, i.e. where the vapor bubbles collapse, is intrinsically submitted to continuous phase changes, pressure waves, and velocity fluctuations. In addition, cavitation attached to solid bodies, which forms a so-called "cavity", is often characterized by instabilities at larger scales, such as an intermittent detachment of its downstream part, forming clouds of vapor bubbles, which are then convected downstream until they collapse under the action of higher pressure9-10.

Although several mechanisms have been mentioned to explain this large-scale instability, a re-entrant jet flowing intermittently from the cavity closure to its leading edge, in the vicinity of the wall, is believed to be one of the primary causes of the cloud shedding phenomenon (see figure 2.1). Forty years ago, Knapp, Daily, and Hammitt11 provided a quite precise description of the flow at the rear end of a cavity, where the external flow re-attaches to the wall. This flow, which initially moves along the cavity, has locally the structure of a jet impinging obliquely upon the wall. The falling stream divides into two parts flowing parallel to the wall. One forms the so-called re-entrant jet, which moves upstream and contributes to the cavity break-off and cloud shedding[2, 3, 8, 12, 13]. The other one

makes the flow re-attach to the wall[14].

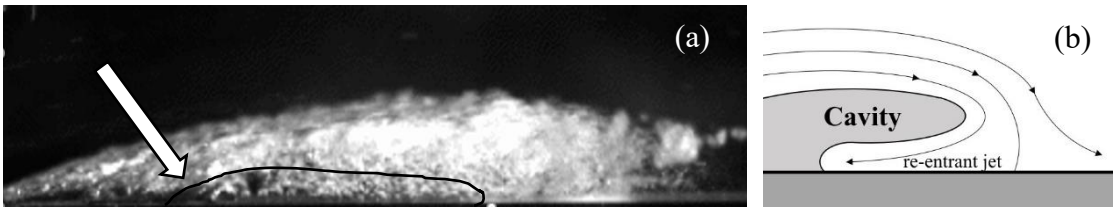

Figure 2.1. Re-entrant jet forming at the bottom of an attached cavity (flow from left to right) (a) snapshot of the jet, as it is flowing upstream, (b) Schematic representation of the jet inception in the closure region

To study the mechanisms of cloud cavitation, various intrusive sensors have been used in the eighties and nineties, such as electrical probes9, optical probes3,15, and endoscopic visulizations16. More recently, non-intrusive techniques such as Particle Image Velocimetry (PIV), X-ray imaging, and infrared imaging have been also applied. Optical PIV based on illuminations with short pulses of laser light sheets faces some major challenges, when it is conducted at the most usual scale of the test sections, i.e. between 5 and 20 cm of characteristic dimension. Indeed, the tracers illuminated by the light sheet at the middle of the test section are masked by all the bubbles in between the middle and the side, so they can be hardly detected by the cameras. In addition, the laser light sheet is significantly disturbed by the bubble light reflections. These issues obviously become worse as the void fraction increases. Using fluorescent particles combined with filters that record only the fluorescent signal emitted by the tracers but not the laser light enables to partially fix them, but the quality of the images of particles is still poor inside the cavity. Conversely, an extensive analysis of the turbulence in the wake of the cavity, where the void fraction is small, have been conducted by Gopalan & Katz17, and the flow dynamics outside from the cavity and in the cavity closure were also investigated18-19. The experiments performed by Dular et al.20-21 have shown that setting the light sheet at a small distance from the side wall (typically a few millimeters) could enable to visualize the fluorescent particles inside the cavitation area and thus access the entire flow dynamics. However, in that case the measurements are limited to the boundary layers of the side walls, and thus do not reflect the most interesting dynamics of the flow.

X-ray imaging is an interesting alternative to optical PIV, which enables to get rid of some of

the limitations mentioned hereabove, since x-rays penetrate straight into the liquid/vapor mixture. Therefore, all issues related to the reflections on the bubbles are suppressed. Combining fast x-ray imaging with PIV has enabled to obtain some first measurements of velocity inside the high void fractions areas[21], for both the liquid phase and the vapor one. However, this technique suffers from several limitations as well, such as the small field of view, imposed by the size of the beam cross section, which does not enable to capture the entire dynamics of the sheet cavities. Another drawback is the quite small number of pictures that can be recorded in a row, imposed by the constraints related to the scintillator integrity, and also the integration of the results in the beam direction, which means that both the far field and the boundary layers are included in the particle motion recorded on the pictures.

These various experimental studies, either based on optical or x-ray imaging, have confirmed the presence of the re-entrant jet in configurations of periodical cloud cavitation, and the correlation between its propagation upstream, up to the cavity leading edge, and the cloud detachment[20, 22, 23]. Some other works have revealed the importance of other mechanisms to explain the cavity break-off, such as a condensation shock that propagates from the cavity closure to its upstream end, as shown by Ganesh et al.[24]. Perturbations at the cavity top interface have been also discussed for a long time[25] and the evidence of the development of Kelvin-Helmholtz instabilities has been recently provided by Dular et al.[26]. Three types of driving mechanisms have been identified by Zhang et al.[27], using a combination of x-ray and laser-based illuminations: the re-entrant jet, the condensation shock mentioned previously, and a pressure wave generated by the collapse of the clouds of vapor.

Some other investigations have also shown the existence of more complex instability modes, where the frequency of the jet is not necessarily equal to the frequency of the cloud shedding[28]. More generally, it has been shown that the re-entrant jet is present at the bottom of the cavity even in the case no large-scale fluctuation is observed. Some authors have suggested that a sufficient momentum of the jet was required to reach the cavity upstream end, and thus trigger the break-off[23], but the exact mechanisms that lead to the different flow instabilities observed in the experiments (a rather stable cavity or regular cloud cavitation, or irregular cloud shedding with multiple small clouds) are still unclear.

In addition, these previous works have been performed using single point acquisition tools or 2D field velocity measurements. The three-dimensional character of the flow structures involved in the re-entrant jet motion and the cavity break-off has not been properly characterized, yet. Callenaere et al.[11] have observed the re-entrant jet and the cavity oscillations, using top and side views, but no quantitative measurements of the 3D effects in sheet/cloud cavitation are available, to the best of our knowledge. In the present paper, the objective is to remedy to this situation by performing time-resolved 2D3C PIV based on laser illumination, to characterize the three-dimensional structures generated by cavitation and analyze their dynamics for different types of instability regimes.

Section 2 presents the experimental setup, the PIV acquisition settings, and the post-processing to obtain the three components of the velocity fields; section 3 is focused on the characterization of the different regimes that were identified, while section 4 discusses the 3D structures observed in these different cases, and their dynamics.

2. Experimental setup and image post-processing

2.1 Test Rig

Cavitation tests were conducted in the small-scale cavitation tunnel schematically represented in figure 2.2. Water circulation is obtained with a Salmson type Multi HE1602-SE-T/2-2G pump with variable rotation speed controlled by a micro-AC Variable Frequency Drive (VFD) model GS2-45P0 to set the flow rate. A tank partially filled with circulation water is used for water cooling at the pump delivery to maintain a constant temperature, using a secondary cooling loop. The volume flow rate is measured by a Bürkert type SE32 turbine flow meter (uncertainty 0.15 l/min after in situ calibrations), and the temperature is obtained with a type K thermocouple, directly in contact with the circulation water.

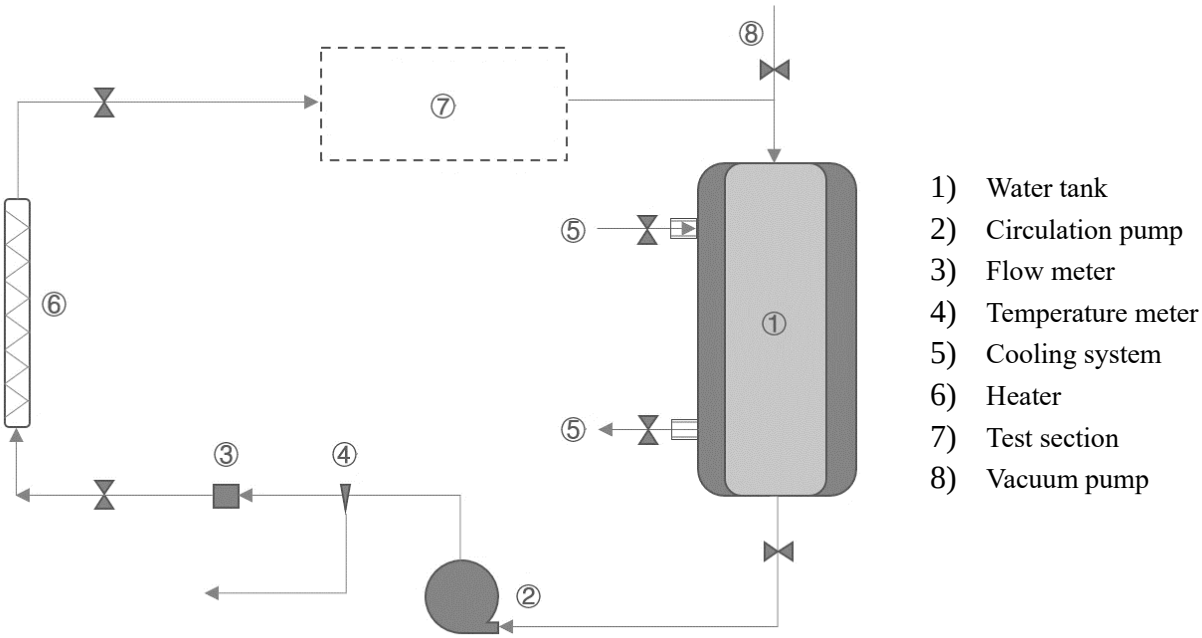

Figure 2.2. Cavitation tunnel

Upstream from the test section, a noise attenuation device is used to filter the periodical pressure fluctuations due to the passage of the pump blades. The reference pressure is measured 10 mm upstream from the venturi test section with a Series 6M/S(C) OEM pressure transducer connected to a EV 94 EB digital indicator. The uncertainty on the measurements was of the order of 50 Pa. Another pressure meter measures the downstream pressure 10mm downstream from the test section. The partially filled tank is connected to a compressor and a vacuum pump, which enables to vary the pressure in this tank between 0.1 bar and 3.5 bar, thus adjusting the pressure in the test section.

2.2 Venturi-type Section

The main body of the test section is 3D printed, while the bottom, top, and side walls of the convergent / divergent nozzle are inserts made of transparent optical glass (figure 2.3). The venturi shape (bottom wall) is a simple wedge: the flow is accelerated in the convergent part of the venturi, which has a 18° angle. The maximum speed at the throat (width 5 mm, height 10 mm) is in the range of 10 to 20 m/s. Cavitation is initiated immediately downstream from the edge of the Venturi, which

has an 8° divergence angle, and it collapses abruptly as the fluid moves outwards, since the pressure re-increases downstream.

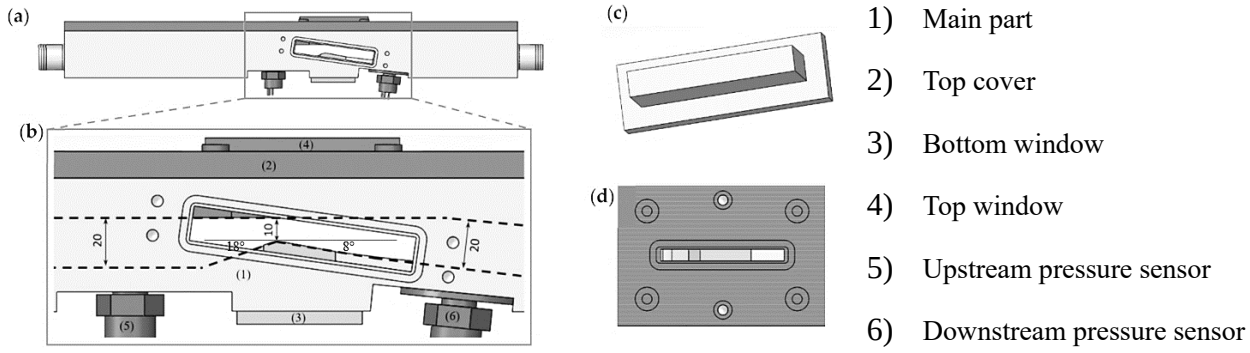

Figure 2.3. Venturi-type section: (a, b) side views, (c) side window, (d) top window

2.3 PIV measurements

The flow field is illuminated from the top with a vertical light sheet generated with a Nd:YAG 300 mJ/ pulse dual-head laser (figure 2.4). The light sheet is about 1 mm thick and is located at the middle of the test section. The flow is seeded with PMMA-RhB-Frak Fluorescent tracers with an average 10 µm diameter, which re-emit light at a wavelength 584 nm, significantly higher than the original 527 nm of the laser.

Two Photron FASTCAM SA1.1 and two Phantom VEO 710 high-speed cameras were used to capture images from the two sides of the test section, as shown in figure 2.4. The cameras on the front side are equipped with a notch filter that eliminates the wavelengths around 527 nm, in order to capture only the light emitted by the particles, while the cameras in the back have density filters that attenuate the light reflected by the cavitation bubbles, to avoid over-illumination. So, images of particles are recorded at the front for velocimetry in the liquid phase, while images of cavitation are obtained at the back, for velocimetry in the gas phase. On each side, the two cameras are oriented with an angle around 25 to 30 degrees from the direction perpendicular to the windows, which was found to be the best compromise between the accuracy of the velocity 3rd component and the sharpness of the images.

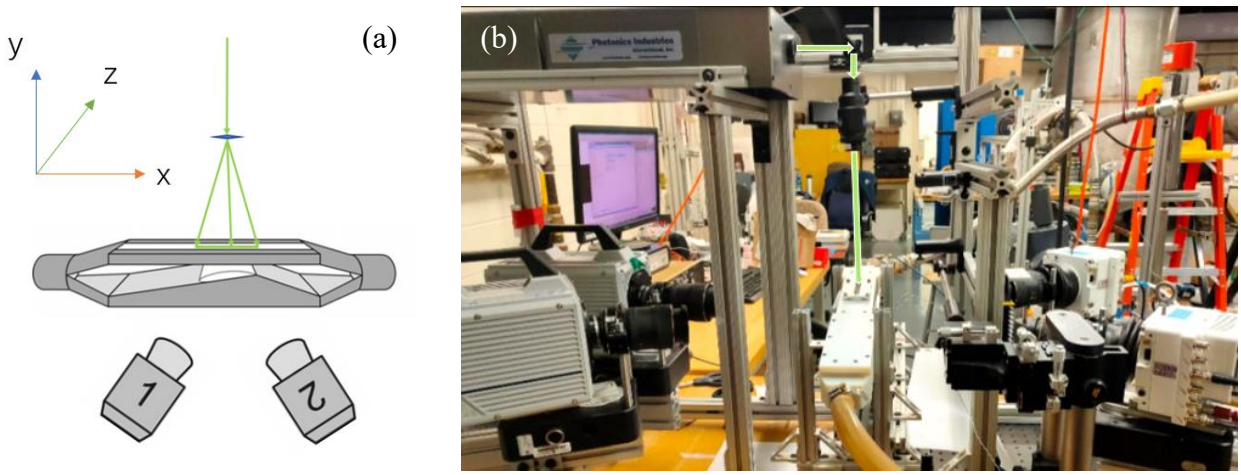

Figure 2.4. PIV setup

The laser generates two short pulses with a 7µs time interval, at a repetition rate of 2500 Hz. The four cameras and the light sheet were synchronized using a high-speed controller operated with the LaVision Davis 8.4 software, so 8-bit images were recorded at the same frequency with resolution of 1024×512 pixels (figure 2.5). The images of particles obtained with the notch filter still include the trace of the sheet cavity (see on the left), while the images of cavitation recorded with the density filter do not capture the tracers, due to the much lower intensity of the emitted fluorescence, compared with the light reflected by the bubbles.

The bright spot generated by each particle is typically 20 to 50 µm, i.e. 1 to 3 pixels on the images. Note that it's about 2 to 5 times the size of the particles only, as the spot is due to the fluorescence emitted by the particles, not the reflection of the incident light, so the halo generated by each particle is significantly smaller.

On the images of the vapor phase, the bubble interfaces cannot be clearly visualized: the smallest gas structures that can be seen are conglomerates of several bubbles. However, these vapor structures generate some significant gradients of brightness, which will enable efficient post-processing to get the velocity fields, as explained hereafter in section 2.5.

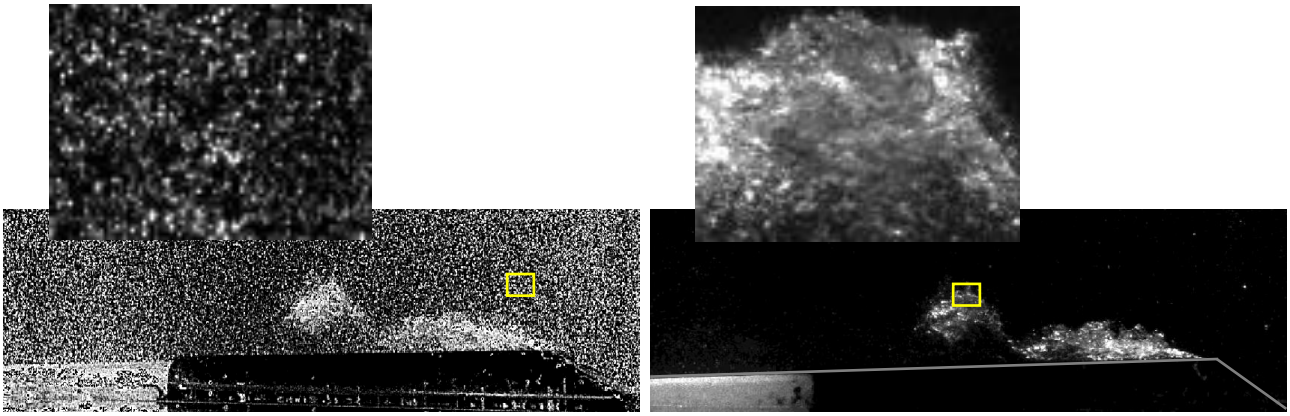

Figure 2.5. PIV raw images: water phase (left) and vapor phase (right)

In order to perform measurements in different planes in the z direction (see figure 2.4), the test section is mounted on a sliding frame controlled with a micrometric screw of precision 0.01 mm, to adjust precisely the laser light sheet position, from the front side to the back side (5 mm distance with 0.5 mm between two successive positions). This setup enables moving only the test section without changing anything in the PIV setup. Note that the test section was fixed rigidly to the frame, so that only the entire frame could slide, but no other motion was enabled, which was critical for the accuracy of the calibration.

A thorough calibration process was performed, once the laser light sheet, camera fields of view and image sharpness were adjusted: the test section was moved so that the light sheet was at the middle of the channel, then the top (see figure 2.3b) was open to the air, but still maintained full of water. A micro calibration plate from LaVision (200 µm distance between the dots, covering the 25×10 mm^2 surface of the field of view) was inserted into the test section and used to record the calibration data. The micrometric screw was used to move the test section to the front and the back, for the need of the stereo PIV calibration. Once the process was completed, the test section was closed for measurements.

2.4 Test cases

A first experimental campaign (not used in the present paper) has enabled to identify different types of cavitation regimes for various Reynolds numbers between 10^5 and 2×10^5, by varying the flow rate from 30 up to 60 l/min, and for various cavitating numbers from 0.85 (large cloud cavitation) up to 1.4 (cavitation inception). The Reynolds number is $Re = h \times V_{th}/\nu$ where h = 10 mm is the channel height at the venturi throat, V_{th} is the average flow velocity at the throat, and ν is the liquid kinematic viscosity at the ambient temperature. The cavitation number is $\sigma = (P_{in} - P_v)/\frac{1}{2}\rho V_{th}^2$, with P_v the vapor pressure, P_{in} the pressure measured upstream from the test section, and ρ the liquid density.

Based on this preliminary investigation, two different sets of data are eventually used in this paper. In data set #1 (table 2.1), the pressure in the tank downstream from the test section is the atmospheric pressure, so the cavitation number is varied with the flow rate. For each flow condition, five positions of the laser light sheet were investigated every 0.5mm, from the center line of the test section to 0.5 mm from the front wall.

Conversely, in data set #2 (table 2.2), the pressure is varied with the flow rate, using a vacuum pump/compressor, to keep the cavitation number the same at various flow rates. Nine positions of the laser light sheet were investigated (every 0.5 mm on both sides of the center plane of the test section).

Note that the test rig does not have any control of the density of nuclei or the amount of dissolved air. This could induce some spurious effect of the water quality on cavitation, especially when the installation is operated at low pressure. To avoid that, all the tests in each of the tables below were performed in a period of a few days, without changing the water, and after having operated the test rig continuously for several hours. This process was found to considerably reduce the risks of altering the sheet cavity at constant cavitation numbers. In the present study, no noticeable change in the sheet cavity length and oscillation frequency could be detected for identical flow conditions tested at the beginning and the end of the measurements.

Test case	T (°C)	P_v (Pa)	ρ (kg/m^3)	V_{th} (m/s)	Q (l/min)	Area (mm^2)	σ	P_{in} (Pa)	P_{out} (Pa)
1	28	3850	995.9	13	39	50	1.40	121500	92600
2	28	3850	996.2	14	42	50	1.23	123800	92400
3	28	3850	996.2	15	45	50	1.10	127300	92100
4	28	3850	996.2	16	48	50	1.00	131800	91700
5	28	3850	996.2	17	51	50	0.92	137100	90700
6	28	3850	996.2	18	54	50	0.87	144800	89500
7	28	3850	996.2	19	57	50	0.84	155000	87700

Table 2.1. Investigation flow conditions - data set #1

Test case	T (°C)	Pv (Pa)	ρ (kg/m^3)	V_{th} (m/s)	Q (l/min)	Area (mm^2)	σ	P_{in} (Pa)	P_{out} (Pa)
8	28	3850	996.2	17	51	50	0.85	126300	65700
9	28	3850	996.2	18	54	50	0.85	141000	69100
10	28	3850	996.2	19	57	50	0.85	156700	91400
11	28	3850	996.2	15	45	50	0.9	104700	61900
12	28	3850	996.2	17	51	50	0.9	133400	83600
13	28	3850	996.2	19	57	50	0.9	165800	109500
14	28	3850	996.2	15	45	50	1	115900	80300
15	28	3850	996.2	17	51	50	1	148000	104700
16	28	3850	996.2	19	57	50	1	183700	132200

Table 2.2. Investigated cavitation conditions – data set #2

2.5 PIV post-processing

The images of particles are used to get the velocity fields in the liquid phase, while the images of the vapor bubbles are used for the determination of the vapor velocity fields (these 2 velocity fields detailed discussed section 3.4). In both cases, the calculations are performed using the Davis 8.4 software from LaVision, and the embedded calibration process described in section 2.3.

For calculations in the liquid phase, a preliminary pre-processing of the images is applied to eliminate the trace of the cavitation. It consists of particle brightness standardization and background filter to remove the effects of spurious global brightness variations. An example of the final images is shown in figure 2.6. As can be seen, in the final images, only the particles are visible, and the signal to noise ratio has been significantly improved, compared with the original images of particles shown in figure 2.5.

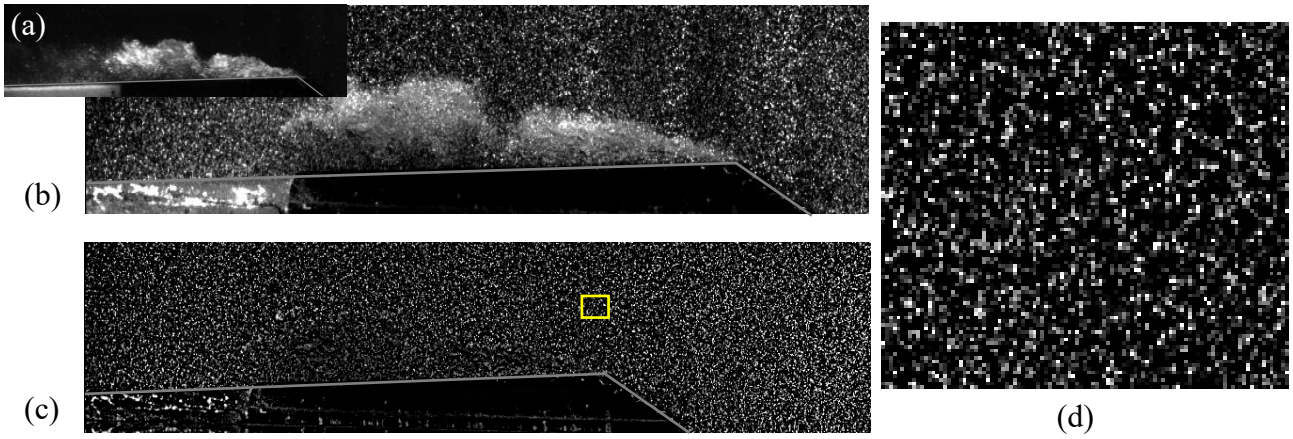

Figure 2.6. Pre-processing of the images of particles: (a) image of cavitation, (b) original image of particles, (c) final image of particles, (d) zoom

For calculations in the vapor phase, the image intercorrelation is not based on illuminated particles, but the gradients of brightness induced by the vapor bubbles. This specific application of PIV algorithms to velocimetry in the vapor phase has been tested and validated in previous works, using both optical imaging[29,30] and x-ray imaging[22,23]. An uncertainty of the order of 3% to 7% was generally obtained in these previous studies. It was found that such accuracy can be obtained only if local brightness intensity gradients are present in the bubbles, while post-processing based on images of interfaces only results in much lower accuracy. Note that this technique provides the speed of the bubbles, not the details of the internal flow inside them, although we will call these speeds "vapor velocities" hereafter in this paper.

For both the liquid and the vapor phases, five passes were performed, with interrogation windows of 64×64 pixels and 50% overlap for the first 2 passes, and 32×32 pixels windows and 75% overlap for the next 3 passes. Vectors with a correlation factor lower than 0.6 or a Q factor lower than 1.3 were discarded. The final results are smoothed by applying a 3×3 Gaussian kernel.

Figure 2.7 shows the typical uncertainty and correlation factor distributions that are obtained for the amplitude of the velocity, in both phases. As for the liquid velocity field, the correlation is about 0.8 in pure water, and it drops significantly in the mixture area, down to about 0.4 in the densest cavitation regions. Regarding the vapor phase, the correlation factor varies between 0.6 and 0.9 in the mixture, with most of the cavity in the range 0.7 – 0.8. Above the cavity, it drops to 0.3, as only a

3limited number of vapor bubbles are travelling in this region.

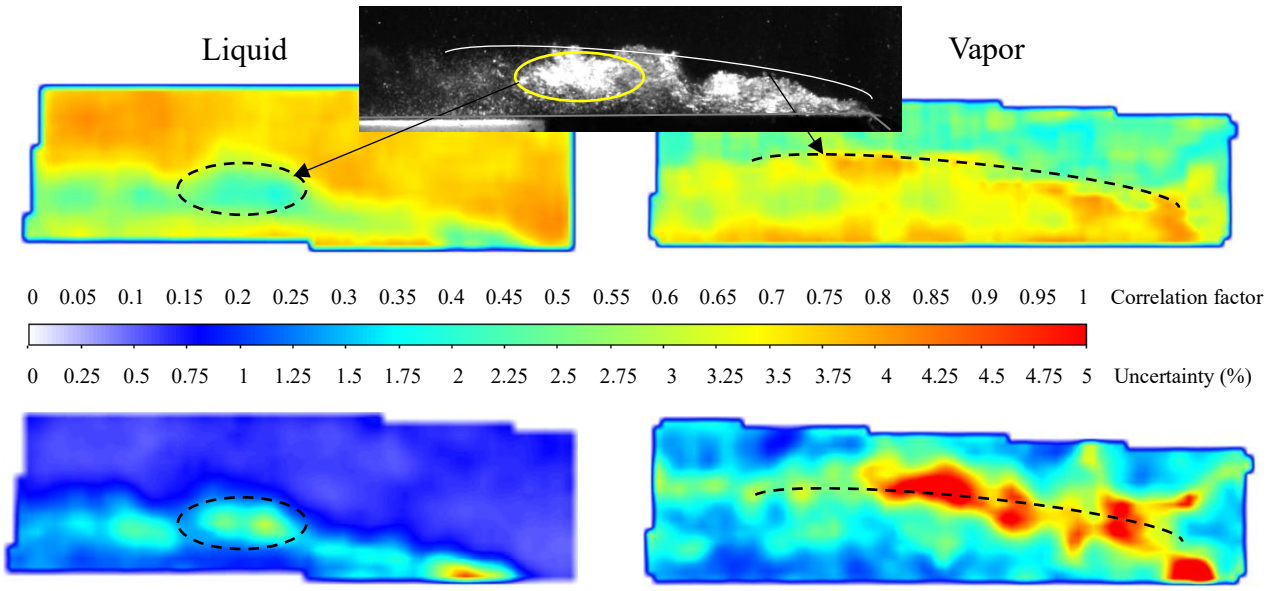

Figure 2.7. Typical correlation factor and uncertainties obtained in the liquid phase (left) and in the vapor phase (right)

Uncertainty is consistent with the variations of the correlation factor. Note that it is calculated by applying half of the calculated velocity field to the first frame of the pair, and -half to the second frame, and performing an intercorrelation of the two resulting images. The results are made non-dimensional using the local calculated velocities, which results in the uncertainties shown here. As can be seen, it is generally in the range of 0.5 to 2%, except in specific areas: the upstream end of the cavity for the liquid phase, due to the large void fraction that does not enable to detect as many particles as in the other areas, and the cavity interface for the vapor phase, as this is where the void fraction is and thus the correlation factor abruptly drops.

It can be observed in figure 2.8 that this uncertainty in the liquid phase is mainly driven by the z component (perpendicular to the light sheet), while the x and y components have uncertainties lower than 1% in most of the cavitation area, and even lower than 0.5% in the half part the closest to the wall. The exact same trend can be observed for the vapor phase as well (not shown here). Note that the conclusions drawn from figures 2.7 and 2.8 generally apply to all the velocity calculations (with some space modifications due to the time evolution of the cavity) and to all the test cases listed in section 2.4.

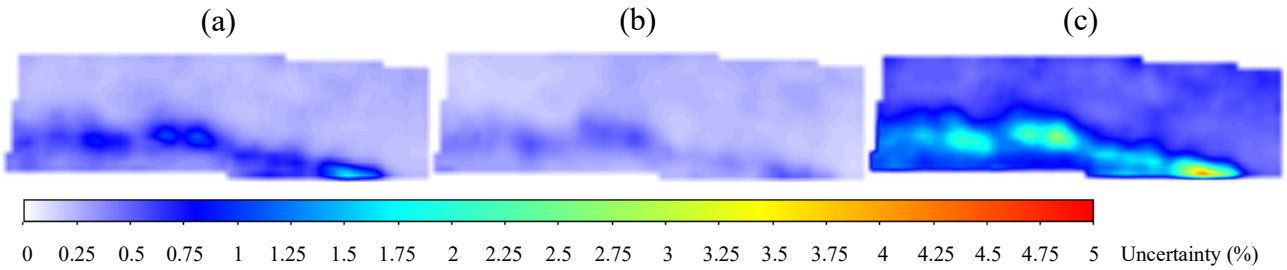

Figure 2.8. Uncertainty on the three components of the velocity in the liquid phase (a) V_x, (b) V_y, (c) V_z

2,500 pairs of images (1 s of time) were recorded for each position of the laser light sheet. This number was found to be appropriate regarding the convergence of the time-averaged components of the velocity, as can be seen in figure 2.9. Obviously, the z-component is the one that requires the largest time to converge, especially in the re-entrant jet area where the flow is highly fluctuating.

The time-averaged values of velocities will be analyzed first in section 3 to characterize the general structure of the flow, then the instantaneous flow fields will be used in section 4 to discuss the different modes of instabilities. In addition, Proper Orthogonal Decomposition (POD) will be applied to help identifying the flow dynamics in section 4. Typically, the flow based on the first 400 first modes will be examined. It enables taking into account 90% of the flow energy, while filtering out the most chaotic part of the flow fluctuations in order to isolate the periodical structures.

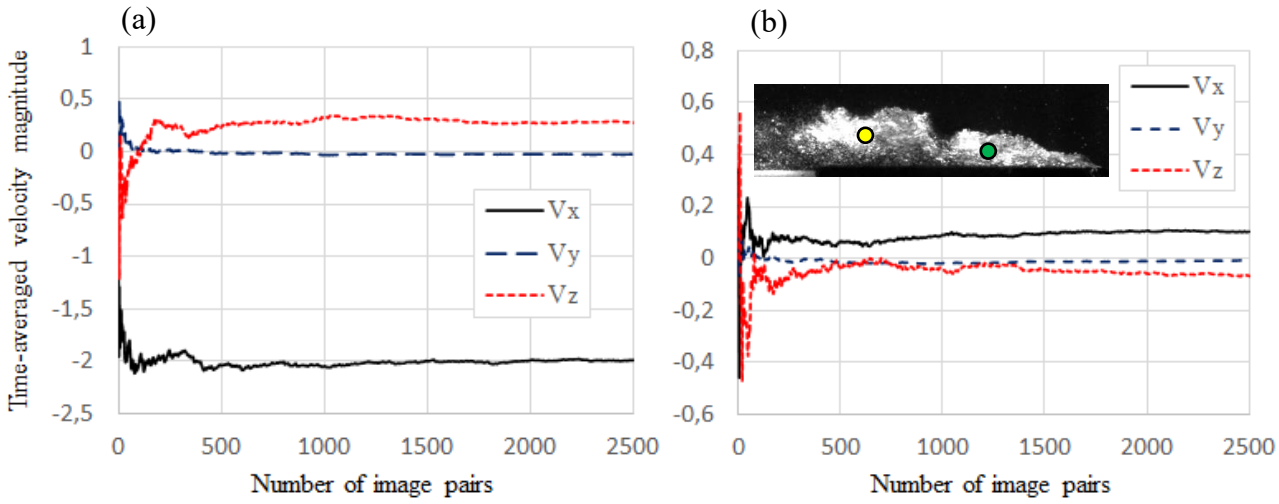

Figure 2.9. Convergence of the time averaged velocity components according to the number of image pairs: (a) at the location of the cloud detachment (yellow dot), (b) in the re-entrant jet (green dot).

3. Flow structure and general dynamics

3.1 General flow structure

The incoming flow was characterized by measuring the time-averaged V_x velocity component and the turbulence intensity along a vertical profile located at the throat of the Venturi. Two flow rates (45 l/min and 57 l/min) are considered, to check the influence of this parameter on the velocity distribution. At 57 l/min, measurements were done in five different vertical planes, from the center of the test section to the front side, to check the flow homogeneity both vertically and horizontally.

Figure 2.10 shows that the flow is pretty homogeneous in both directions and both flow rates: the velocity is almost constant in the top half of the test section, while it slightly increases down to the bottom, by about 3% at 45 l/min and 7% at 57 l/min, due to the local flow acceleration. Horizontally, the velocity decrease from the center to the last position on the side is less than 5%, so it is concluded that the incoming flow is quite two-dimensional and uniform.

The turbulence intensity is mostly in the range 2 to 3.5%, except at the very bottom and in the top boundary layer, where it increases up to 5 to 6%. No major effect of the flow rate on these values is noticed, but the fluctuations are significantly enhanced close to the side wall, compared with the center of the test section, due to the influence of the boundary layer.

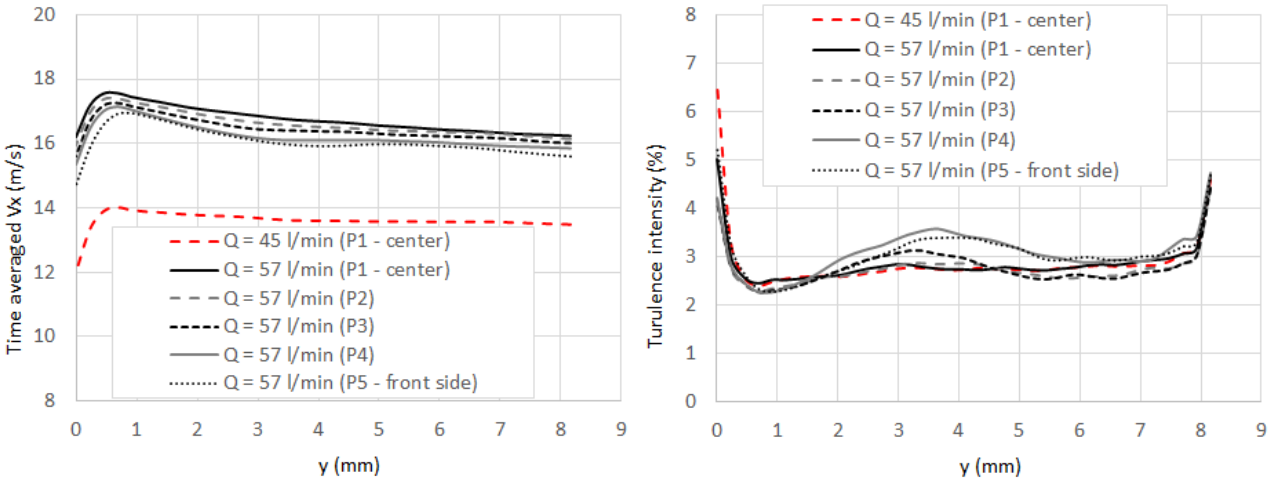

Figure 2.10. Inflow time-averaged velocity (x component) and turbulence intensity for flow rates of 45 l/min (center of the channel only) and 57 l/min (5 planes from the center of the channel to 0.5 mm to the side window, the distance between two successive planes is 0.5 mm).

3.2. Cavitating behavior

In data set #1, as various flow rates were applied at atmospheric pressure, the cavitation region increased progressively, and different behaviors were obtained (see figure 2.11). At the smallest flow rates (test cases 1 to 3), a small sheet cavity is observed with non-organized fluctuations and random cloud detachments in its rear part. As the flow rate is increased (test cases 4 and 5), the cavity significantly increases and the fluctuation becomes regular, with a large-scale periodical shedding. At the two largest flow rates (test cases 6 and 7), some irregularity affects these shedding, as multiple clouds are sometimes generated, which might merge or interact together. As a result, the oscillation frequency is not so clear anymore. These three distinct behaviors will be called sheet cavity, cloud cavitation, and multiple cloud cavitation hereafter, which is consistent with the names usually given in the literature.

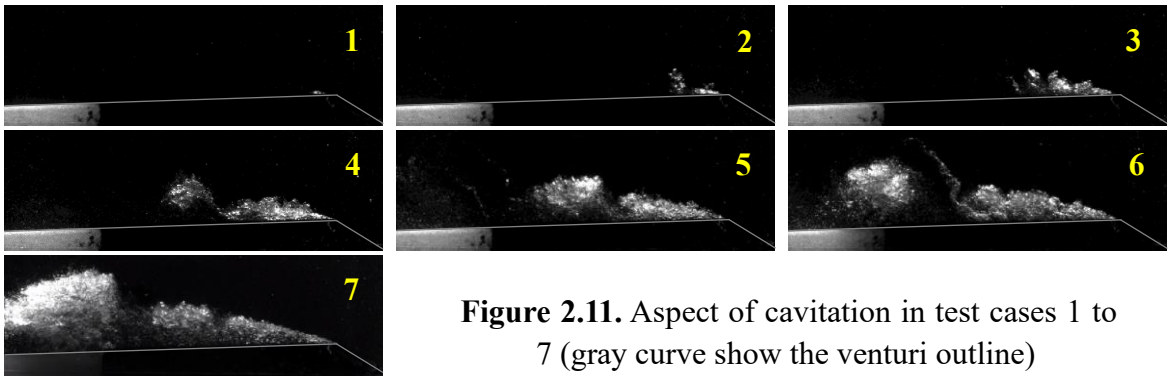

Figure 2.11. Aspect of cavitation in test cases 1 to 7 (gray curve show the venturi outline)

The flow field generated by the cavity is generally characterized by a large-scale recirculation, inducing a re-entrant jet in the vicinity of the bottom wall, as can be seen in figure 2.12. This is just a time-averaged behavior here, the flow unsteadiness will be discussed later. Also, note that only the liquid flow velocity is shown here, but the vapor flow is qualitatively very similar. A quantitative comparison between the dynamics of the two phases will be shown hereafter.

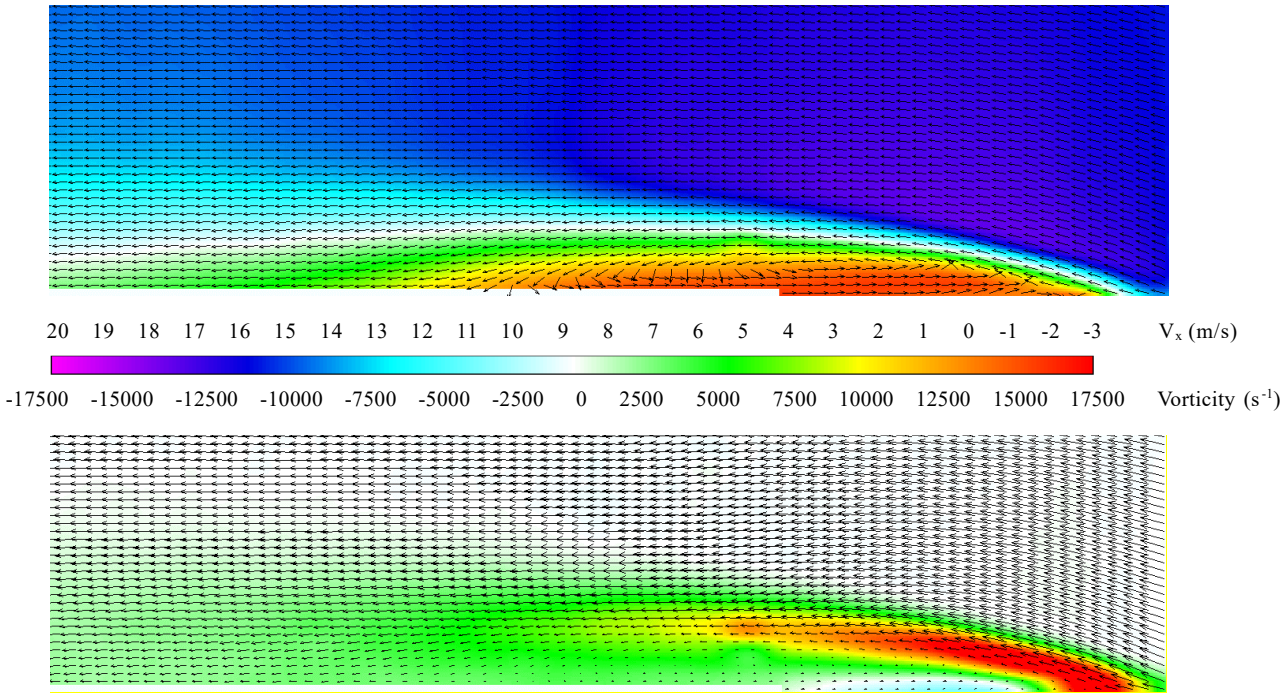

Figure 2.12. Example of the time averaged flow structure (test case #6, liquid phase). V_x velocity component with same length velocity vectors (up) and vorticity field with real vectors (down)

3.3. Effect of the flow non-dimensional numbers on cavitation

To discuss the flow dynamics at various conditions of operation, it is necessary to identify first which parameters impact cavitation. In that regard, the precise determination of the cavity length has always been a challenge in experiments focused on cloud cavitation, because of the fluctuating nature of the flow and the difficulty of finding a "limit" to the cavity. In addition, the flow illumination does significantly impact the conclusions: typically, in the case of laser light sheet illumination, the spanwise location of the light sheet is important, due to the three-dimensional shape of the sheet cavity. figure 2.13a shows that different grey levels evolutions in the x direction are obtained in the 5 vertical planes located from the center to the front side of the test section: if this information had to be used to define a mean cavity length, the value would depend significantly on the selected position. The same can be said about the cameras: the four cameras used in the setup record different levels of brightness, even if they were tuned to be similar. In conclusion, using this information to define the cavity length is very subjective.

In the present study the use of PIV has enabled to find a new appropriate way to define the mean cavity length. Indeed, figure 2.13b shows that the evolutions of both the maximum (in each cross-section) vorticity in the z direction, and the maximum speed of the re-entrant jet (note that everywhere the value is negative, there's no re-entrant jet) are very similar in the five vertical planes. Therefore, these quantities can be used, assuming that an objective threshold can be defined. Here, the location where the re-entrant jet vanishes downstream, i.e. the x value where there is no positive velocity in figure 2.13b, is selected as the end of the mean cavity.

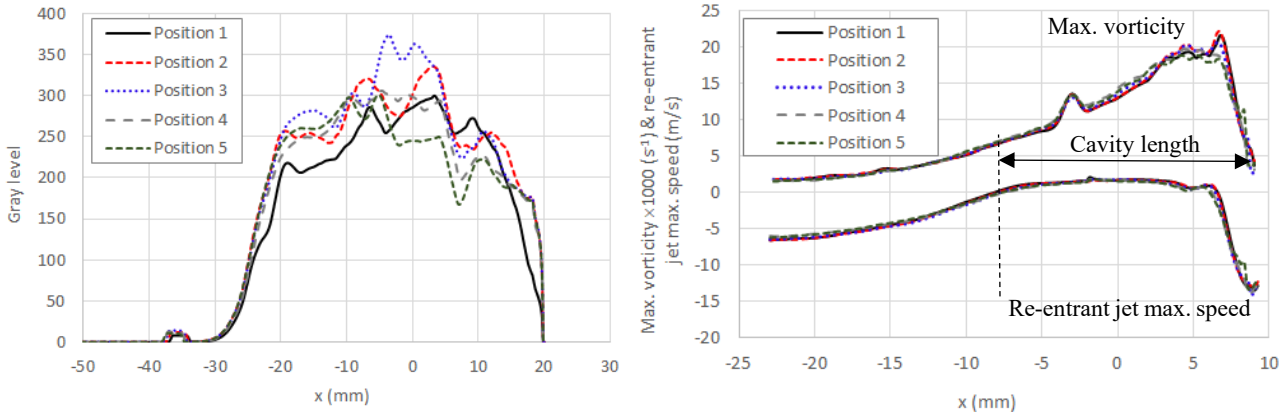

(a) (b)

Figure 2.13. (a) Max. gray level evolution in the flow direction, in the 5 vertical planes from center (position 1) to front side (position 5) of the test section; (b) Max vorticity and re-entrant jet max. speed evolutions, in the same 5 planes (test case #5).

The analysis of the effect of the flow parameters on the cavitation development has also generated a lot of contradictory conclusions in the last decades: the cavitation number is supposed to primarily determine it, however it depends significantly on the pressure used to calculate it, and it is also well known that the Reynolds number and the water quality, especially the amount of dissolved gas, also affect cavitation.

Typically, in the present study, it was found in the series of tests performed at constant σ number that increasing the Reynolds number systematically leads to a receding of the cavitation area (see figure 2.14). But the opposite effect was found by Coutier-Delgosha et al. 2005, for example.

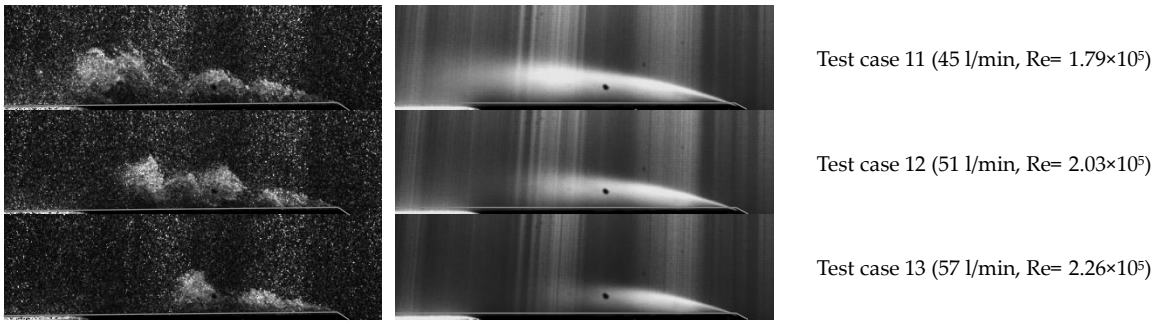

Figure 2.14. cavity length for σ = 0.9 and different flow rates – example of raw image (left), time-averaged brightness (right)

To get a better idea of the differences between the 3 cavities shown in figure 2.14, the time-averaged flow field was investigated in more details. Although the general structure is very similar in the three cases, two significant modifications can be noticed (see figure 2.15): the amplitude of vorticity distribution increases with the flow rate, and the magnitude of the V_z component, i.e. the transverse recirculation, is also increasing. It suggests that the increase of the Reynolds number results in an amplification of the local pressure gradients that induce the vorticity and secondary flow in the z direction, also leading to the increase of the void fraction and the amplification of the periodical shedding intensity, as reported in previous studies by Coutier-Delgosha et al.[8]. However, this effect is hidden here, at first sight, behind a cavity shrinking, which has a different explanation.

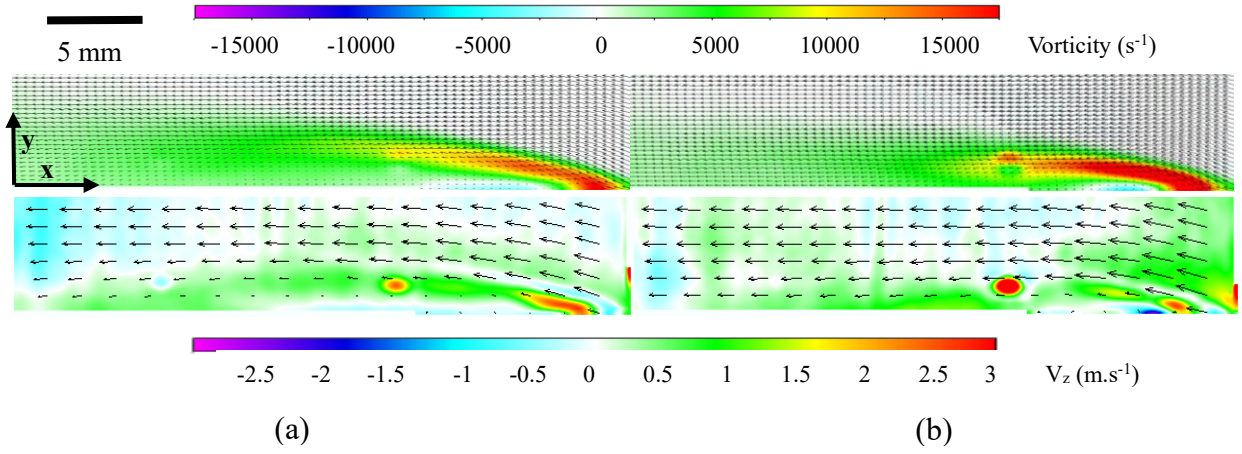

Figure 2.15. Comparison between cases (a) #11 (45 l/min) and (b) #13 (57 l/min) at σ = 0.9: the time-averaged vorticity field at the top, the time-averaged V_z velocity component at the bottom

It is believed by the authors that the exact position where the pressure is measured makes a significant difference in the impact of the flow rate on the cavity. Basically, any head loss induced by the hydraulic loop in between the pressure tap and the cavitation area will vary with the flow rate and induce some bias in the calculation of the cavitation number, and thus in the way the cavity length will change according to the Reynolds number.

To avoid that bias in the present study, the average upstream and downstream pressure measurements (see figure 2.3 for their locations) are used instead of the upstream value. It is assumed that the resulting pressure is much closer to the one that would be measured downstream from the venturi throat, above the sheet cavity. The corrected cavitation number can be defined as $\sigma_{corrected} = \left((P_{up} + P_{down})/2 - P_v\right)/\frac{1}{2}\rho V_{th}^2$

As a result, it can be observed in figure 2.16 that all data of cavity lengths and re-entrant jet lengths collapse to a single curve, for all values of Reynolds and $\sigma_{corrected}$ (see figures 2.16b, c), while it was not the case with the initial σ calculation (see figure 2.16a).

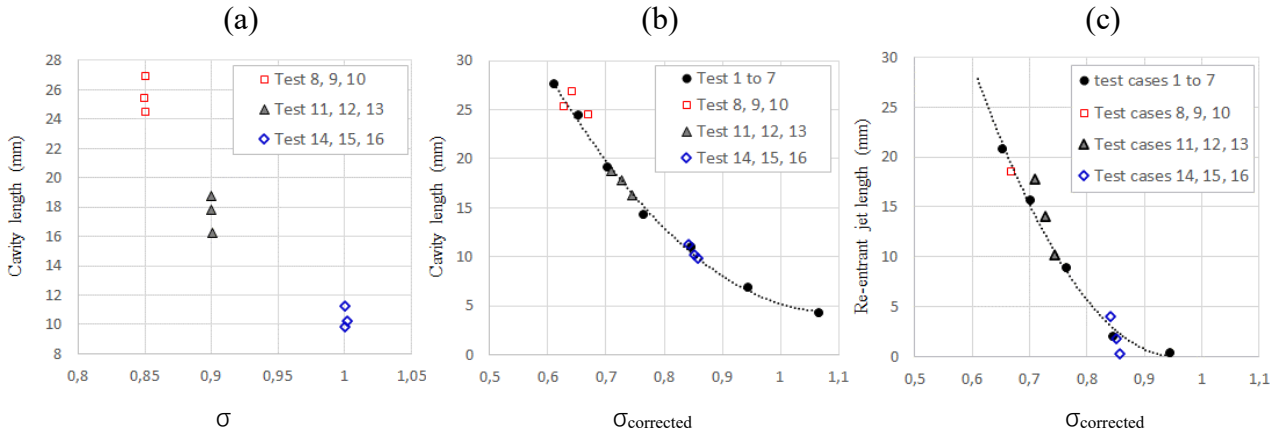

Figure 2.16. (a) Mean cavity length in all test cases, according to σ based on the upstream pressure, (b) same when $\sigma_{corrected}$ is calculated based on the average upstream / downstream pressure, (c) length of the re-entrant jet for $\sigma_{corrected}$ calculated based on the average pressure

3.4 Dynamics of the liquid and gas phases

It was usually assumed, until recently, that the liquid and gas phases have identical behaviors in cavitating flows. It was a reasonable hypothesis, as the size of most of the entrained bubbles are sufficiently small (a few microns to a few hundred of microns) to assume that they will be carried by the liquid flow without any slip.

However, it was found in the last ten years, using velocimetry based on x-ray imaging, that a significant slip between the two phases does exist in configurations of cloud cavitation[22,23]. It was suggested that the presence of big bubbles (typically up to 1 mm radius), the density of bubbles in such flows, which promotes bubble / bubble interactions and bubble cloud behaviors, and the superposition of instabilities at different scales (from the large scale periodical shedding to the high-frequency turbulent fluctuations) could be responsible for this slip velocity.

No detailed information about this mechanism has been reported, yet, so the objective of this section is to use the present measurements to quantify in a better way how different the dynamics between the two phases are, and to discuss the reasons for these differences.

Test case #6 is primarily used hereafter, as it relates to a large sheet cavity, characterized with an intense and pretty regular cloud cavitation behavior, so it is a good candidate to identify the main features of the slip velocity field. Figure 2.17 shows a basic comparison between the liquid and velocity time averaged V_x and V_y components, respectively. Four profiles perpendicular to the bottom wall, located at x = 3 mm, 12 mm, 16 mm, and 24 mm downstream from the venturi throat, are used to draw the velocities. These 4 stations correspond typically to areas of (1) separation of the initial pure vapor zone into bubbles, (2) strong re-entrant jet progression, (3) detachment of the clouds of vapor, (4) convection of the clouds, according to the present observations and the conclusions previously reported by Zhang et al. (2020) in the same flow configuration, using high-speed x-ray imaging.

Note that the cavity shown in figure 2.17 is just a snapshot at a given time to show where the velocity profiles are located, but it does not reflect the entire area where vapor can be. The sheet

cavity is highly fluctuating, so its shape changes over time, and bubbles and even bigger structures are travelling sometimes at higher y positions than what is shown here. It explains why a vapor velocity can be calculated up to 7.5 mm above the bottom wall, at stations 2, 3, 4.

Regarding the V_x velocity component, three main areas exhibit a significant slip velocity:

(i) the top half of the sheet cavity, where the vapor speed is lower than the liquid one. This is the main effect observed in the previous studies, which is related to the fact that the biggest vapor structures in this area are sometimes moving at a lower speed than the liquid. In other words, the biggest bubbles and the agglomerates of bubbles are not perfectly carried out by the main flow.

(ii) the very top of the profiles, where the vapor speed looks higher than the liquid one. It is believed that this is due to the time-averaging of the data, not to a physical mechanism. Indeed, at such height, vapor structures are only present from time to time, when the attached cavity gets temporarily thicker and/or generates a larger cloud detachment. In such a case, the liquid flow above the cavity experiences a reduction of the actual section of passage, and thus an acceleration, which impacts both the liquid and vapor phases. But on average, this effect only slightly impacts the liquid velocity, while it is the main part of the vapor velocity.

(iii) the vicinity of the wall, specifically at stations 2 and 3, where a larger vapor speed is also observed (either positive or negative). This might not be very clear in figure 2.17, but it will be confirmed hereafter in other vertical planes and for other flow rates. This third effect is related to the nature of the re-entrant jet. Indeed, it was reported in many previous studies, both from CFD and experiments, that the tip of the jet is an area of intense recondensation, while it flows upwards. It means that the front of the jet, where the speed is the highest, has a large density of vapor bubbles. Once these bubbles have collapsed, the velocity is lower, and that lower velocity is reflected only in the liquid velocity, not the vapor one. So, on average, it makes sense that the re-entrant jet area shows a larger vapor velocity.

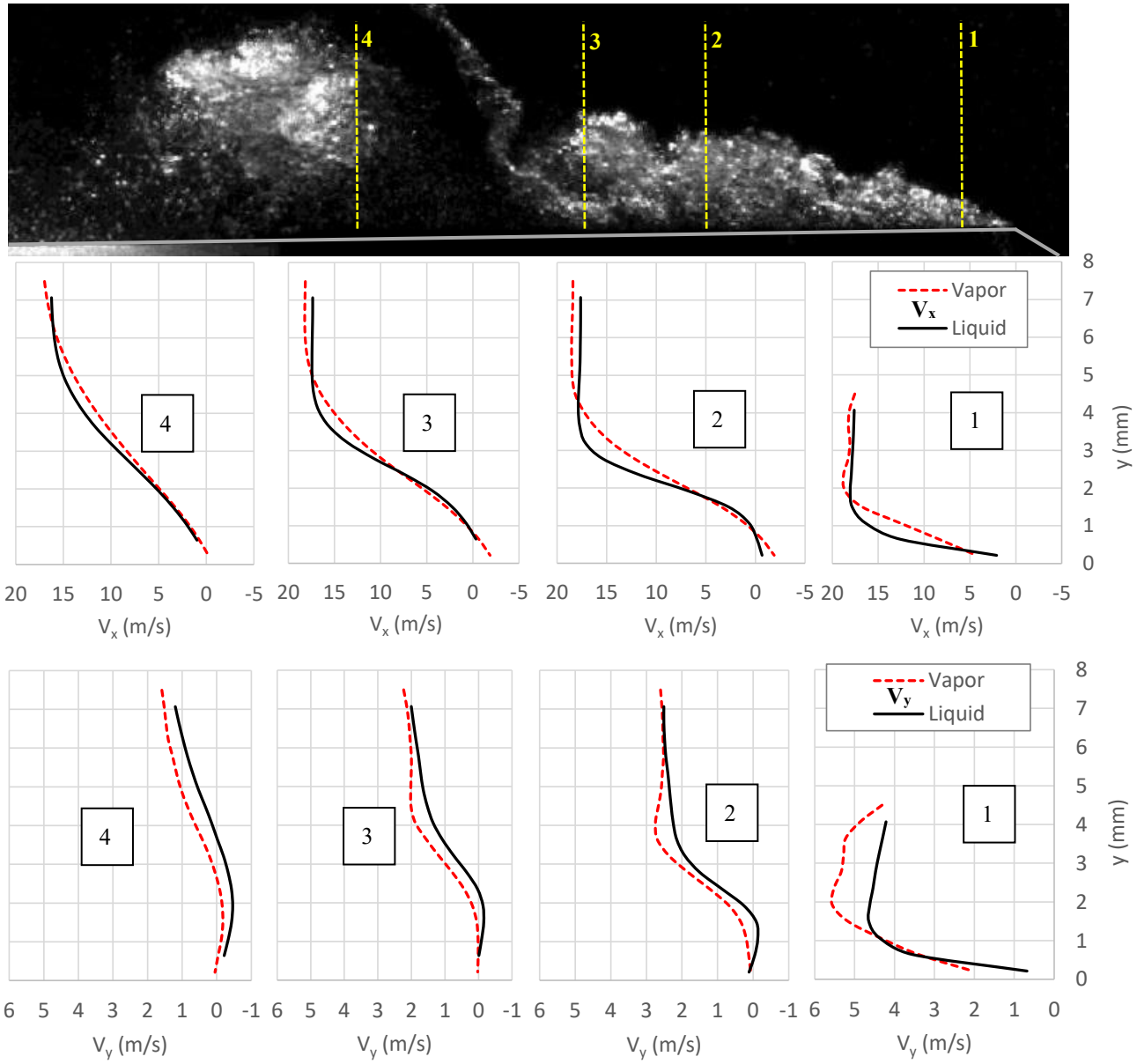

Figure 2.17. Time-averaged liquid and vapor Vx (top) and V_y (bottom) velocity components along the 4 profiles indicated at the top (Test case #6)

The V_y component generally shows a larger vapor speed as well, towards the positive y direction. It is related to the specific motion of the vapor structures which are moving up while transported by the main flow, and eventually form the large cloud of vapor, as can be seen by the global shape of the cavitation area. Conversely, the liquid flow is just following the basic expansion of the venturi section.

Figure 2.18 shows the non-dimensional slip velocity in the x direction, along the same vertical

profiles, in four different vertical planes located from the center of the channel (P1 in black) to 5 mm off the front side (P4), again for test case #6. Generally, the observations reported here above in the middle plane also apply to the 3 other planes. The additional information provided here is that the slip velocity obtained close to the wall is more intense close to the side wall, compared with the center of the channel, at stations 2, 3, 4. It suggests that the side boundary layers do not slow down the bubbles as much as the liquid. In other words, the three-dimensional cavitation structures, as they are carried out by the main flow, are not completely responding to the local liquid speed variations: instead, their dynamics is impacted by the global motion of the vapor, such as the convection of the cloud of vapor.

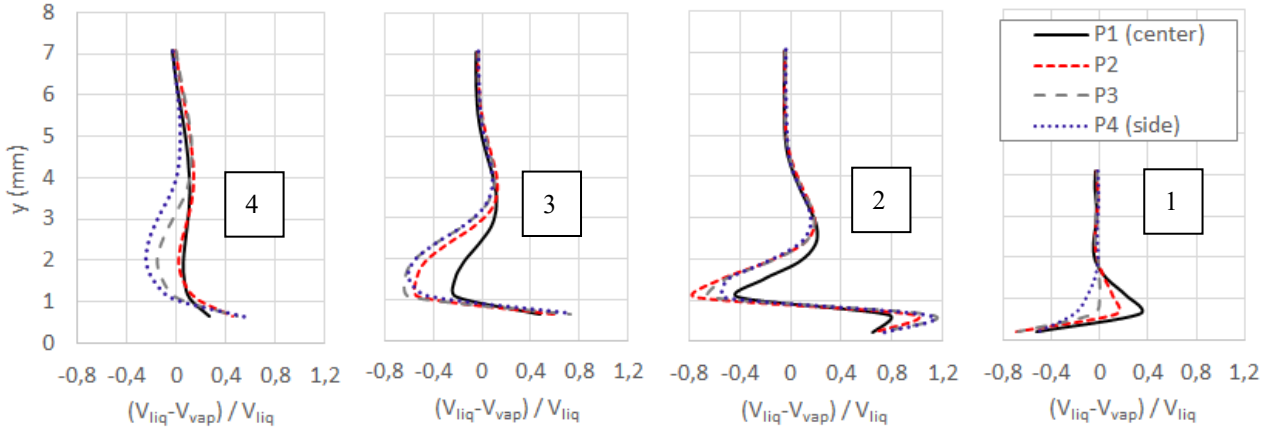

Figure 2.18. Time-averaged non-dimensionalized liquid and vapor Vx velocity component along the 4 profiles, in four different vertical planes located from the channel center (P1) to the front side (P4), 5 mm from each other (Test case #6)

The non-dimensional slip velocity variations obtained for V_x with test case #6 are very similar for all the flow rates investigated in this study. Figure 2.19 shows the data for test cases 1 to 6. When looking at this figure, we should keep in mind that the cavity size is not the same in these different test cases (see figure 2.11). At the lowest flow rates, only a small density of bubbles are convected downstream and generate the vapor velocity on these graphs, so it makes sense that the slip velocity is very small along profiles 3 and 4, and progressively increases with the flow rate. More upstream, the same trend observed before repeats for all flow rates (positive slip velocity in the top half of the

cavity and negative slip velocity close to the bottom wall), but it amplifies with the flow rate (although the values here are non-dimensional). It means that bigger cavities tend to enhance the specific dynamics of the vapor phase. This is also consistent with the explanation proposed for the slip velocity at the wall, since this effect should be stronger when the flow instability, and thus the re-entrant jet, is strong and regular, i.e. in typical cloud cavitation at flow rates 48 l/min and above.

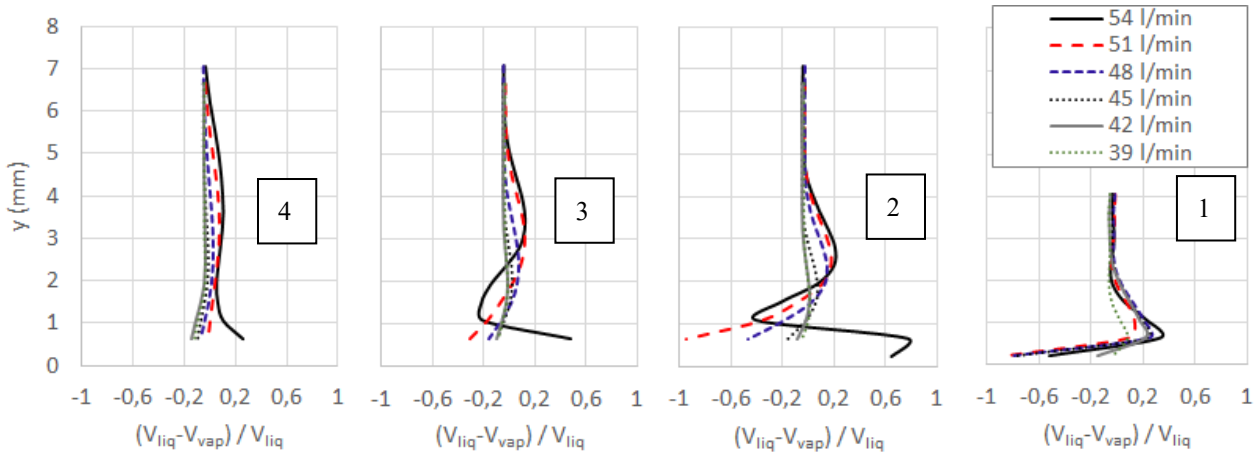

Figure 2.19. Time-averaged non-dimensionalized liquid and vapor V_x velocity component along the 4 profiles, in the vertical plane located at the center of the channel, for 6 different flow rates (test cases 1 to 6)

4. Investigation of the unsteady mechanisms

Generally, cavitation obtained in the present experiments can be divided into three different regimes: (i) typical cloud cavitation, where the cavity breaks off periodically and a single cloud of vapor is shed downstream, (ii) multi-clouds cavitation, where this instability generates more than one cloud, and (iii) sheet cavitation where the rear end of the cavity is affected by random fluctuations without shedding or just small non-periodical shedding. The present section is focused on these three regimes, using the PIV results to discuss the mechanisms involved in each of them.

4.1 Single cloud cavitation

In the typical single cloud cavitation cases, the periodical unstable behavior of the cavity can be divided into four main stages, as shown in figures 2.20 to 2.23, which display the shape of the cavity, the velocity fields (both in x and y directions) and the vorticity field at four different stages of a periodical cycle(for a clear and concise description of the four main stages, only liquid phase results are presented hereafter).

The first stage is the growing of the sheet cavity (figure 2.20). At this time, the previous cloud of vapor has detached from the main cavity and is convected downstream, while the remaining part of the sheet cavity is re-growing (see figure 2.20a). As shown in figure 2.20b, which displays the velocity field in the X direction inside the yellow dashed box indicated in figure 2.20a, a re-entrant jet (flowing from the left to the right with a positive velocity, see the red arrow) is clearly visible inside in the bottom half of the cavity, close to the wall. Note that the velocity vectors have all identical lengths, while the colors provide the magnitudes. Velocities up to 3 m/s are obtained in this area, while the main flow outside the cavitation area has a speed close to -20 m/s, and the rest of the cavity (in between the re-entrant jet and the pure liquid flow) is characterized by a sharp transition from -20 m/s up to a positive velocity.

The re-entrant jet brings energy from the downstream area back to the upstream end of the cavity. It has been shown in previous studies[23,27] that the tip of the jet (see the red circle) is characterized by a significant recondensation of the flow, meaning that the vapor bubbles collapse, so the front of the jet is mostly liquid. It suggests that the tip of the jet is an area of higher pressure that triggers this recondensation (also called bubble shock wave by Ceccio et al.[5,6]). Most of the previous experimental data have identified the re-entrant jet as a time-averaged negative velocity along the main flow direction, just as we observe in figure 2.20b (see Stutz et al.[15]). However, it can be seen from the velocity field in the Y direction (figure 2.20c) that the re-entrant jet has a more complex structure. It is composed of a series of small vortices or small circulations (as shown in figure 2.20c and also on the vorticity field in figure 2.20d) about the Z direction, which are moving downstream along with the main cavity cloud vortex at speed from -6m/s (at the front end) to -19m/s (at the middle section), while expanding in the Y direction. Note that the velocity vectors have also an identical length, like

in figure 2.20a, but fewer vectors are represented for the sake of clarity.

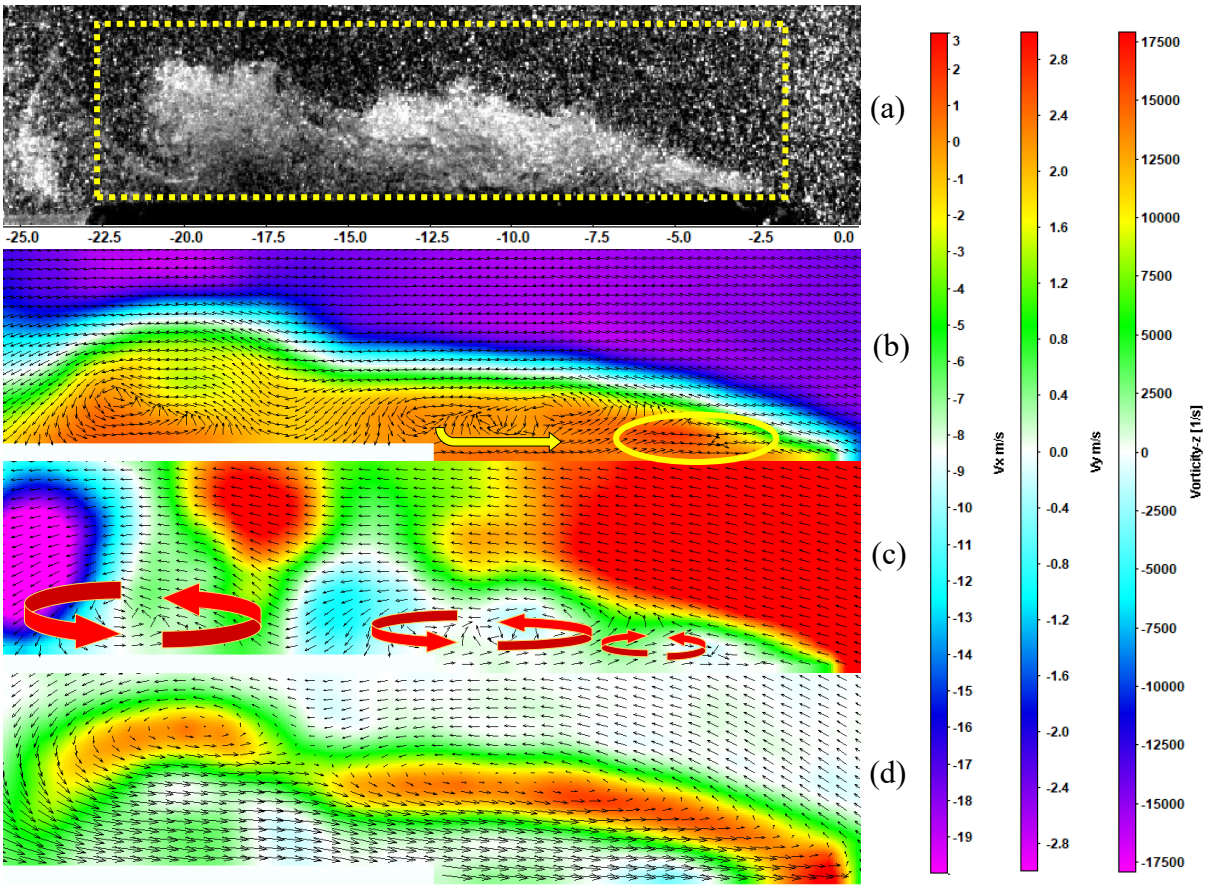

Figure 2.20. Stage 1 (cavity growing, T_0) in single cloud cavitation (test case #5). (a) Image of the cavity, (b, c) velocity field in the x and y directions, (d) vorticity fields. The velocity vectors are shown in pictures b, c, d with equal sizes, just to show the flow structure. In figure (d), it shows the relative velocity, so the time averaged velocity has been subtracted.

The second stage of the cycle is the up lift of the sheet cavity. As shown in figure 2.21a, a bulge of cavitation bubbles is formed in the second half of the cavity and starts to detach from the main cavity. At the same time, the re-entrant jet velocity decreases significantly (see figure 2.21b), becoming almost zero at the tip, which means that it nearly stops. This is due to the generation of a new intense vortex at the leading edge of the sheet cavity (see the blue circle in figure 2.21d), which blocks the progression of the jet. The series of vortices mentioned in step 1 are still moving downstream (see the red circle superimposed with the vorticity field in figure 2.21d), while the one at the most upstream position is pushed up, which initiates the break-off of the cavity. It can be assumed that the high pressure already mentioned at the tip of the re-entrant jet, combined with the

additional increase due to the stopping of the jet, is responsible for this lift, which results in the formation of a local bulge in the cavity, and eventually its break-off.

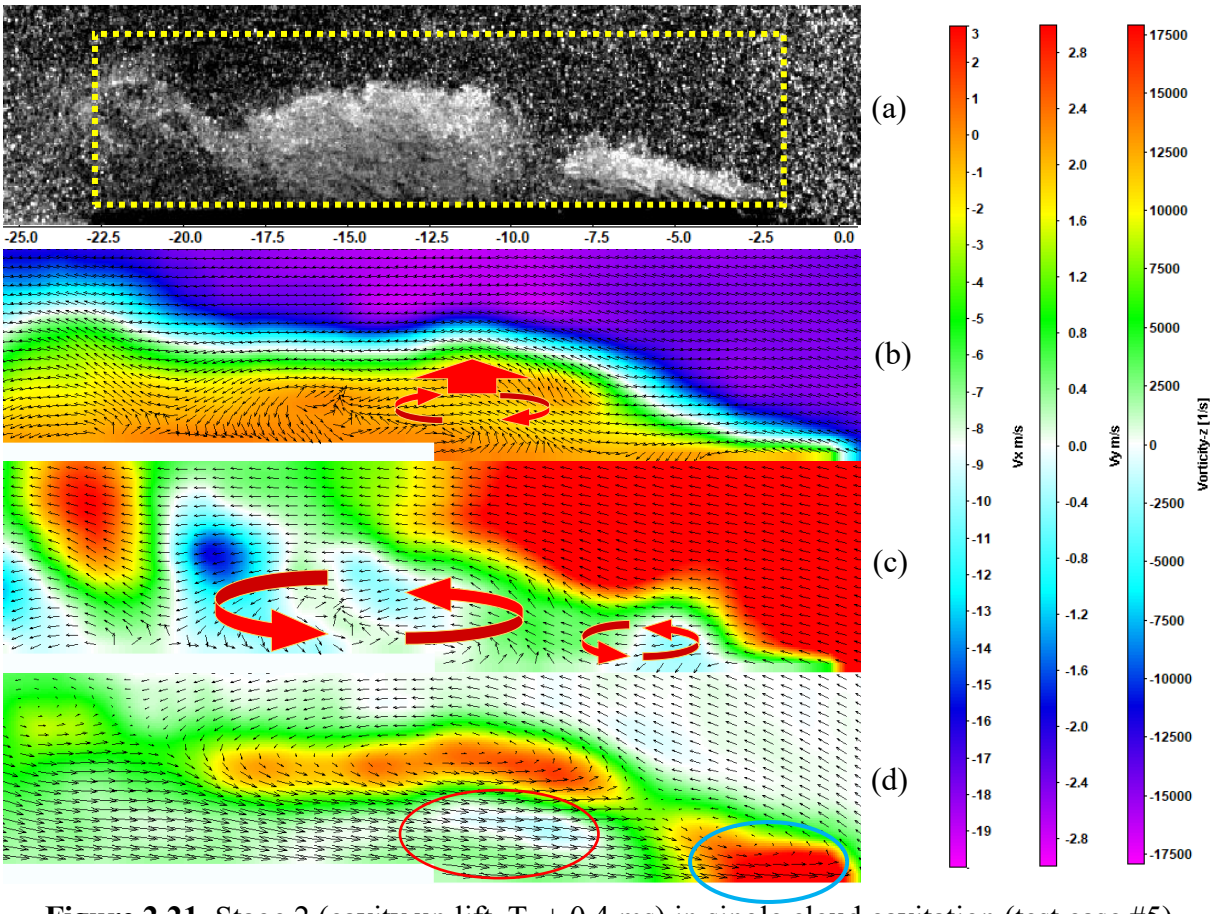

Figure 2.21. Stage 2 (cavity up lift, T_0 + 0.4 ms) in single cloud cavitation (test case #5). (a) image of the cavity, (b, c) velocity field in the x and y directions, (d) vorticity fields. The velocity vectors are shown in pictures b, c, d with equal sizes, just to show the flow structure. In figure (d), it shows the relative velocity, so the time averaged velocity has been subtracted.

The 3rd stage is the cavity break-off. As shown in figure 2.22a, the bulge continues to detach from the main cavity. Its front end is more and more lifted, while its back (downstream) starts to move to the bottom wall direction, resulting in a counterclockwise rotation. This rotation is due to the joint actions of a stronger re-entrant jet under the cavitation cloud (see the white circle in figure 2.22b) and the main flow above the cavity (see the yellow circle), which pushes the top of the cloud downwards.

As a result of this rotation, the bulge begins to roll up inwards, gradually forming a cloud-like

structure, which is thus called a vapor cloud. At the same time, because of the blockage generated by this cloud, the flow above the cavity decelerates (see the left area inside the yellow circle) and deviates up and down, thus cutting the cavity interface and promoting the complete detachment of the cloud from the main cavity (as shown in the vorticity field in figure 2.22d). This "cut in" process can be used as a clear marker to distinguish a full cycle from a simpler cavity oscillation without any major cloud generation. Moreover, this stage also shows how the re-entrant jet vortex system is formed and interacts with the main flow region.

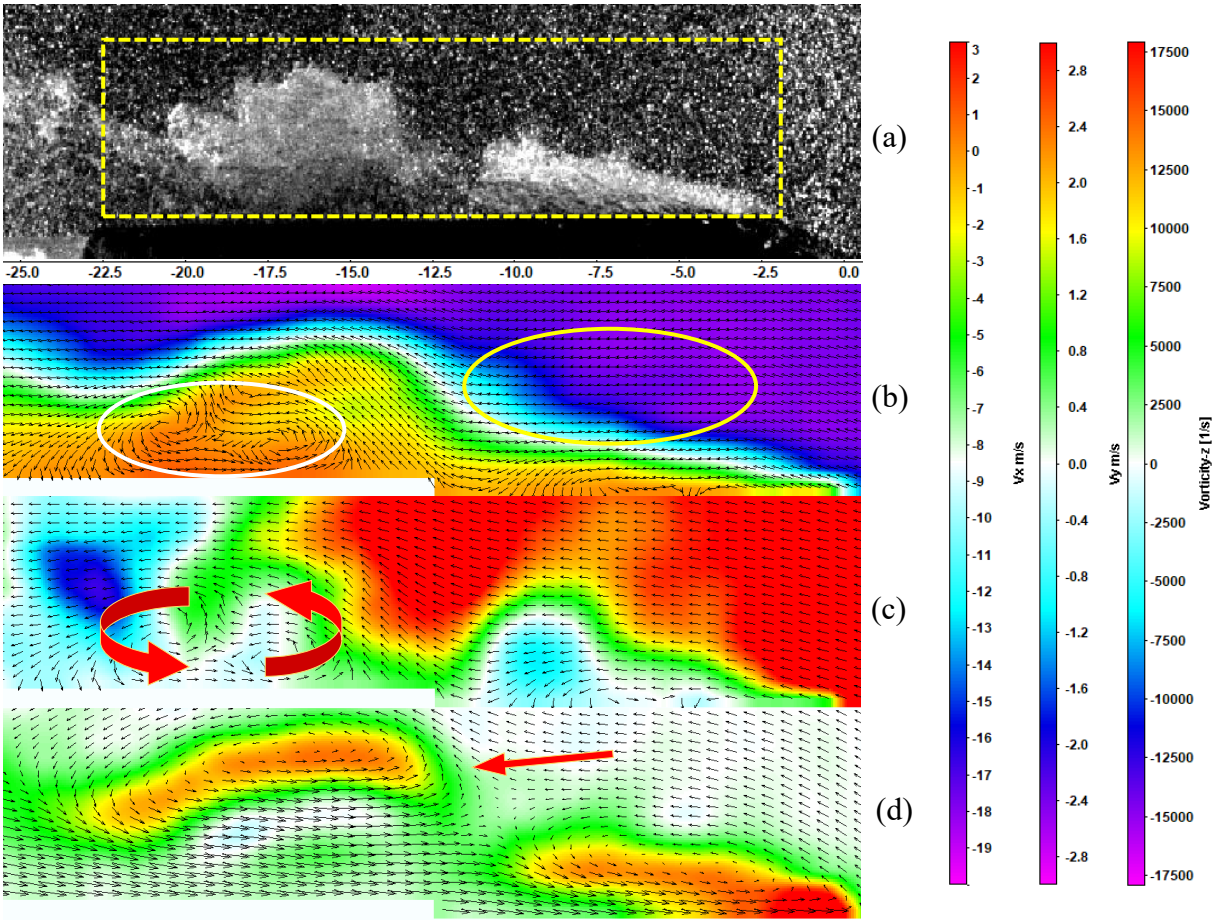

Figure 2.22. Stage 3 (cavity break off, $T_0 + 0.8$ ms) in single cloud cavitation (test case #5). (a) Image of the cavity, (b, c) velocity field in the x and y directions, (d) vorticity fields. The velocity vectors are shown in pictures b, c, d with equal sizes, just to show the flow structure. In figure (d), it shows the relative velocity, so the time averaged velocity has been subtracted.

The 4th stage consists of the convection of the detached cavity cloud. As shown in figure 2.23a,

the cloud has already completely separated from the main cavity, and a new cycle is about to start. The velocity field in the x-direction (see figure 2.23b) shows that the re-entrant jet below the cavity cloud is almost completely suppressed by the vortex system, with only a tiny backflow far downstream (as shown by the yellow circle), while a new strong re-entrant jet is created at the back of the attached cavity (as shown by the blue circle). This implies that the re-entrant jet has the same periodic pattern as the cavity cloud shedding, in this flow configuration. The velocity in the y direction (see figure 2.23c) and the vorticity field (see figure 2.23d) show that the vortices in the re-entrant region below the cloud of vapor are generating a shear flow between the cloud and the main liquid flow, which might contribute to the slip velocity observed in the previous section.

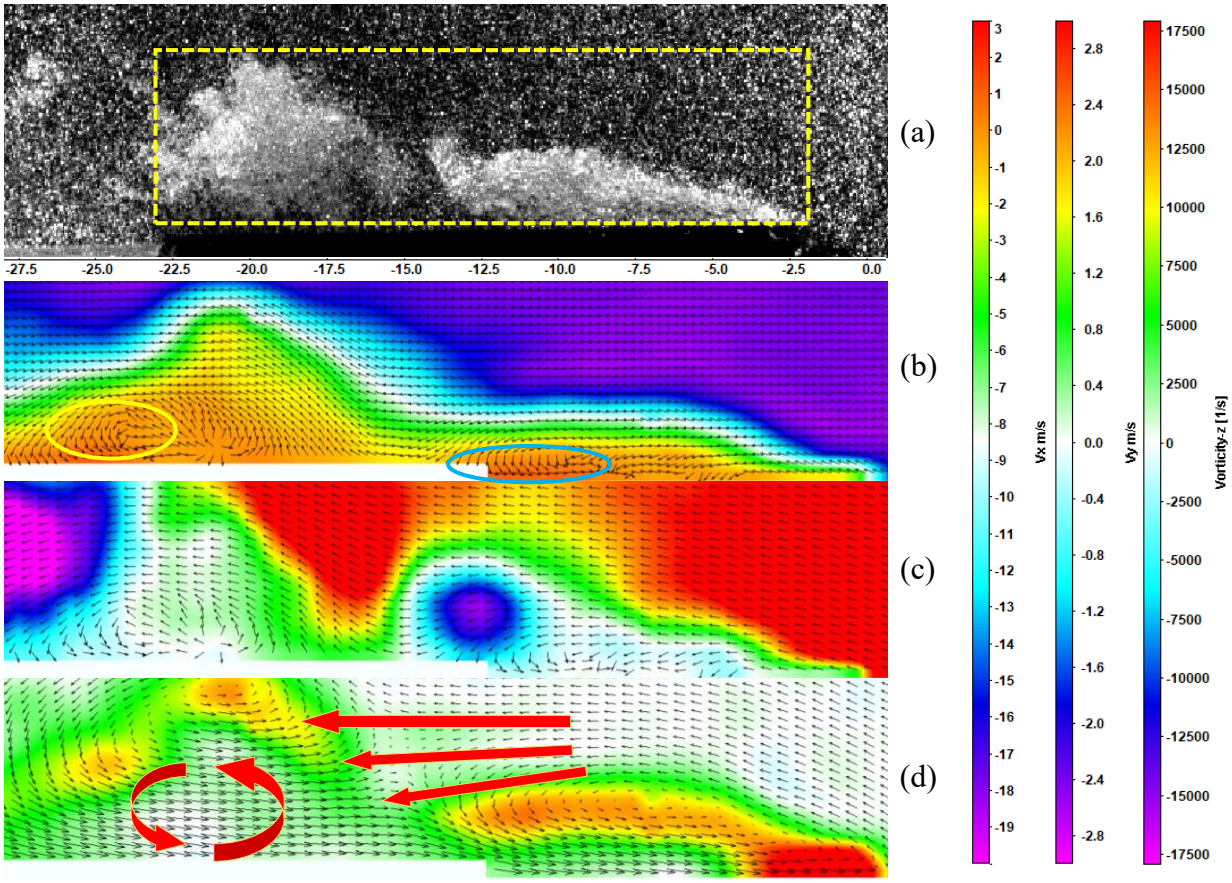

Figure 2.23. Stage 4 (cloud convection, T_0 + 1.2 ms) in single cloud cavitation at flow rate (test case #5). (a) Image of the cavity, (b, c) velocity field in the x and y directions, (d) vorticity fields. The velocity vectors are shown in pictures b, c, d with equal sizes, just to show the flow structure. In figure (d), it shows the relative velocity, so the time averaged velocity has been subtracted

4.2 Multi-clouds cavitation

In cases of large sheet cavities, several clouds are often generated and shed simultaneously, which is called here a multi-clouds configuration. In such cycles, the four stages described in the previous section still exist, but they are more complex and difficult to identify. Figure 2.24 shows a sequence of some raw images (in the middle), vorticity fields (left), and velocity fields in the x direction (right) to illustrate first the growing of the attached cavity.

At time T_0, it can be seen in the raw image that the previous cloud of vapor detached from the main cavity has been convected downstream and are collapsing, while the remaining part of the sheet cavity is re-growing. Frame 2 (T_0 + 0.4 ms) shows the growth of the new sheet cavity, but unlike the typical single cloud cavitation, the sheet cavity does not create a distinct bulge: the whole sheet cavity is compact and thinner, attached to the bottom wall without any significant lifting effect. As the sheet cavity continues to grow (T_0 + 0.8 ms), a small bulge is created at the rear of the cavitation area (red circled area) and tends to detach from the main cavity area (see the yellow arrow). However, in the next frames 4 and 5, it is found that the detachment did not occur; instead, the bulge and the main cavity stretched, forming a long wavy single cavity. From T_0 to T_0 + 1.6 ms, the velocity field in the x-direction (on the right) shows a strong re-entrant jet close to the bottom wall, with a maximum velocity of about 3m/s. In contrast to the single cloud cavitation (figure 2.20b), this re-entrant jet is much thinner and has a higher speed, which is quite constant from the rear end of the sheet cavity to its leading edge. So, the jet does not slow down, which is likely related to the fact that its cross-section does not significantly increase, since the large bulge was not formed, in contrary to the single cloud case. Therefore, the cavity does not encroach too much into the main flow region, which allows cavitation to continue to grow throughout the entire process.

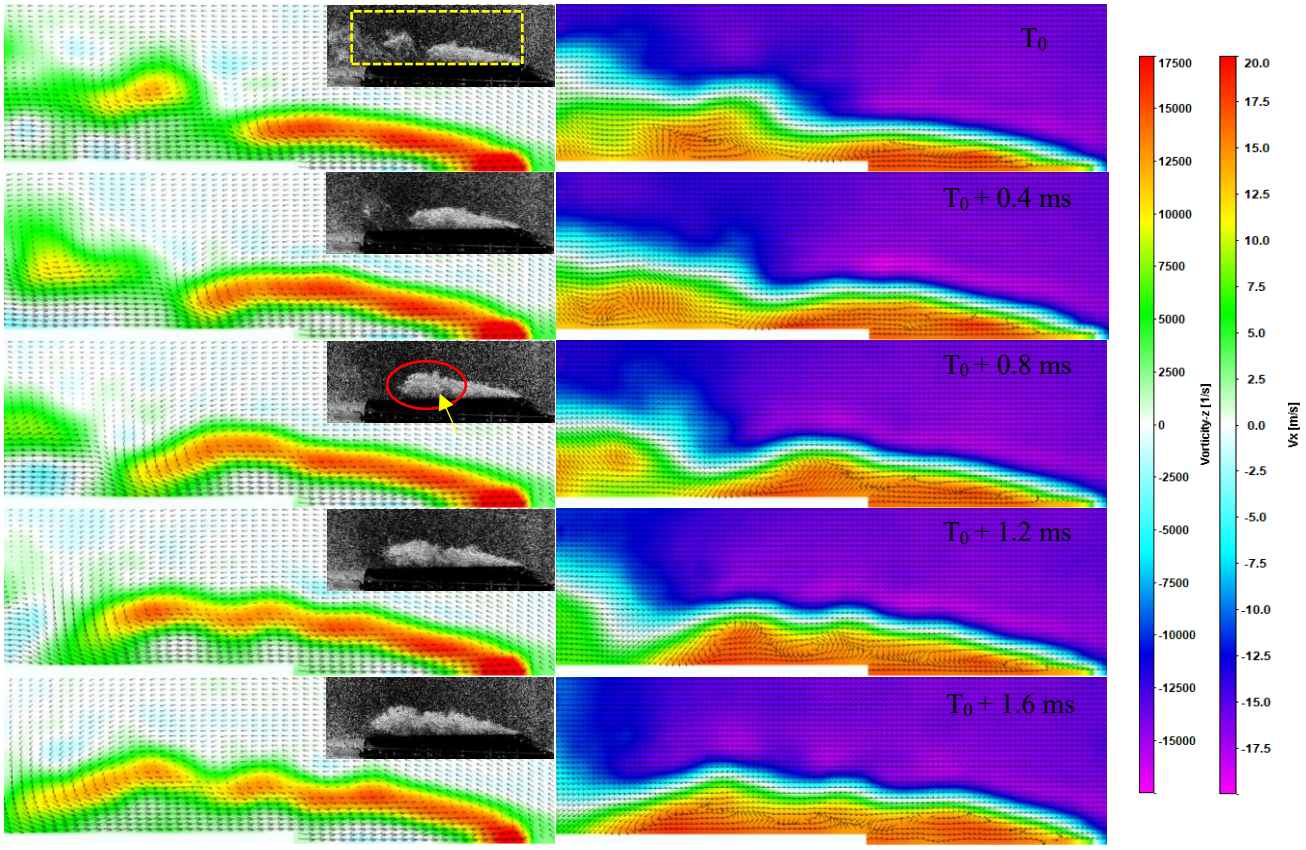

Figure 2.24. Growing of the attached cavity in the multi-cloud cavitation cycle at flow rate 54 l/min (test case #6) - Vorticity field (left), image of particles (middle), x-component of velocity (right) every 0.4 ms (T_0 is the start of the cycle, one period of the entire cycle is typically 5 ms)

In the next stage of the cycle (shown in figure 2.25 at T_0 + 2 ms), the situation starts to change, and a bulge can be observed in the middle of the wavy sheet cavitation (see the white circle in figure 2.25a). The velocity field in the x direction shows that at this point, the intensity of the re-entrant jet has severely decreased, and it has almost dropped to zero in the middle of the cavity (shown by the red circle). Due to this reduction of velocity, the local pressure rises, so a zone of relatively high pressure is formed in the middle of the cavity, like during the up-lift phase in single cloud cavitation (see figure 2.21b). This zone of high pressure creates a lifting effect (visible on the velocity field in the y direction in figure 2.25c, as shown with the blue circles) and therefore the bulge is created. Also, the vorticity field (figure 2.25d) shows in the bottom part of the cavitation region, a series of vortices that generate the wavy shape of the sheet cavity. This stage can be considered as the up-lift stage in the case of multi-clouds cavitation. However, unlike single cloud cavitation, due to the higher

intensity of the re-entrant jet, this process continues for a larger time, until the clouds of vapor are pushed completely downstream, which will be discussed in the following stage.

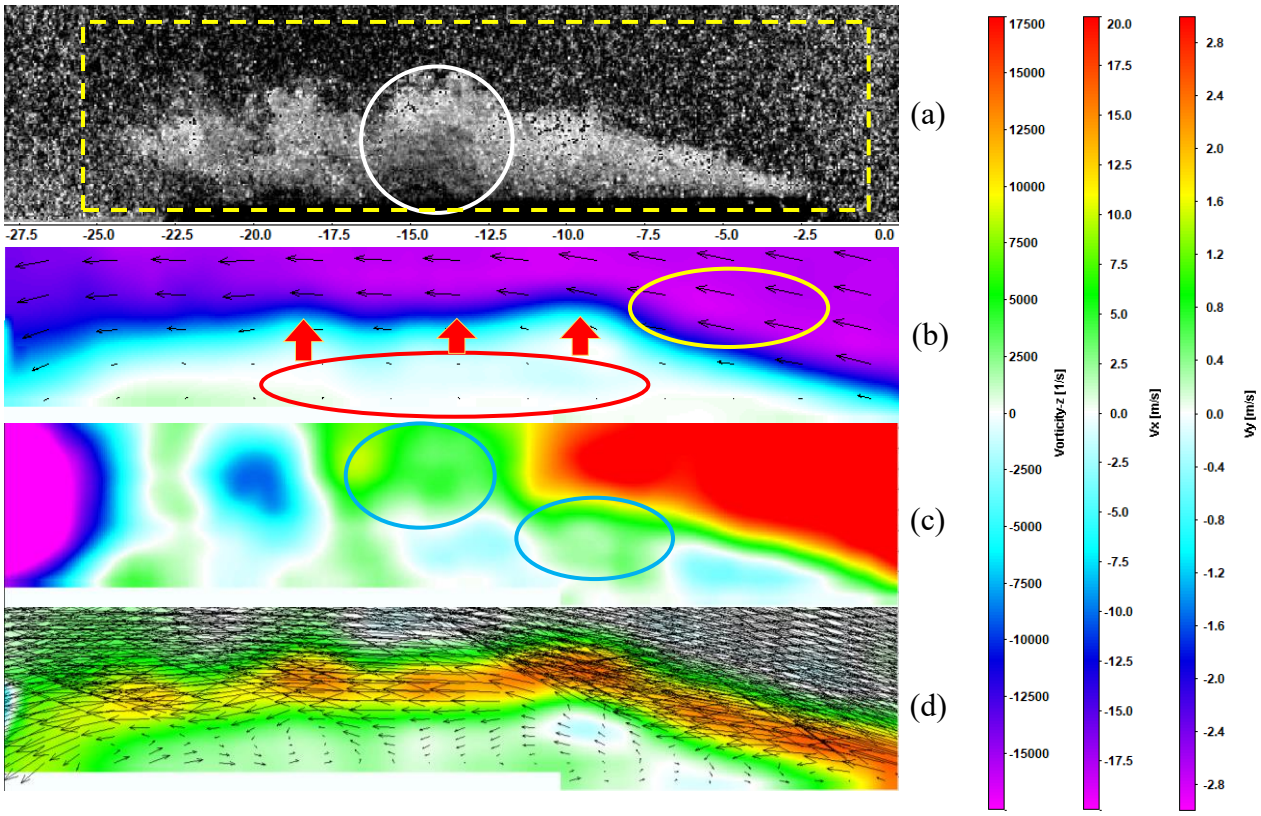

Figure 2.25. Cavity at time T_0 + 2 ms in the case of multi-clouds cavitation (test case #6). (a) Image of the cavity, (b, c) velocity field in the x and y directions, (d) vorticity fields. The velocity vectors are shown in pictures b and d to show the flow structure.

Like in the case of single cloud cavitation, the re-entrant jet thickens rapidly after the bulge is created and the main flow is slightly compressed (see figure 2.25b), creating a high-pressure zone on the upper right side of the bulge (yellow circle), and thus the break-off of the cavity as shown in figure 2.26 at T_0 + 2.4 ms and after. Figure 2.26a shows that the wavy sheet cavity is stretched rapidly, like in the growing process shown for single cloud cavitation in figures 2.23d and 2.23e. The difference, however, is that two clouds start to detach from the main cavity at almost the same time at T_0 + 2.8 ms (figure 2.26b), and the two clouds are both detached simultaneously at T_0 + 3.2 ms (figure 2.26c). They are eventually pushed downstream and start to collapse around T_0 + 3.6 ms (figure 2.26d).

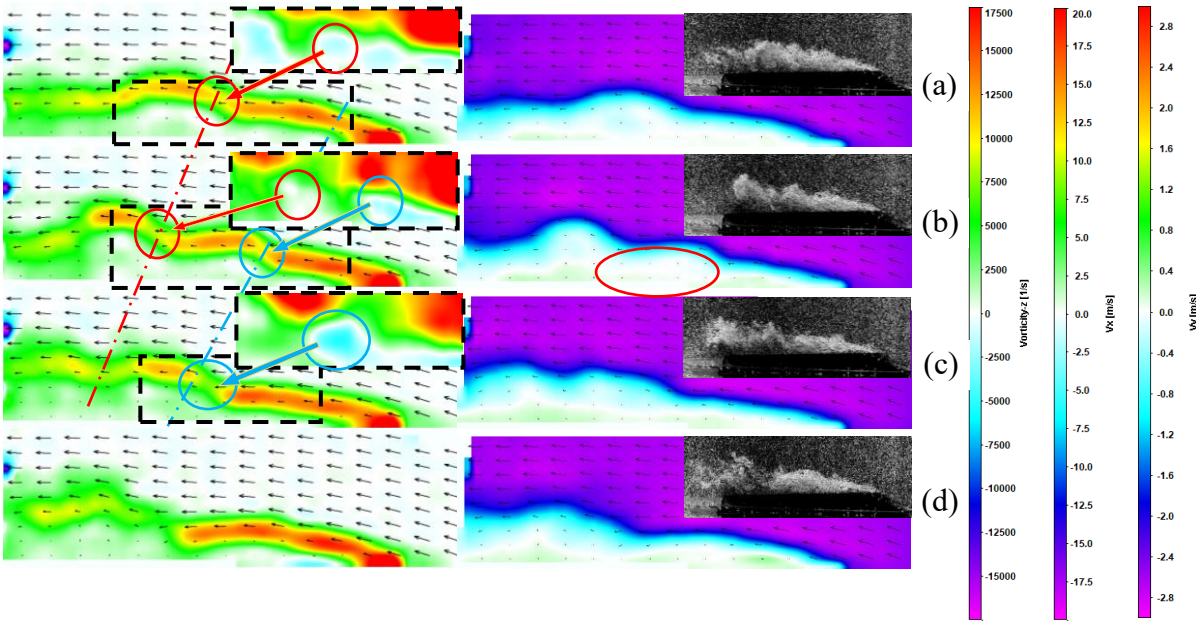

Figure 2.26. Break-off and convection of multi clouds cavitation (Test case #6)

Left: vorticity field and velocity vectors, V_y velocity component in the top image

Right: V_x velocity component and velocity vectors

Times T_0 + 2.4 ms (a), T_0 + 2.8 ms (b), T_0 + 3.2 ms (c) and T_0 + 3.6 ms (d)

These observations suggest that the slowdown of the re-entrant jet is the trigger for the cavity break-off: as the jet becomes unable to sustain a longer wavy sheet cavity, the main flow tends to intrude at the weakest point, i.e., at the middle of the re-entrant jet, thus cutting it as shown with the red circle on the vorticity field (figure 2.26a, left), and also the negative V_y in the same location. As can be seen from the V_x distribution (figure 2.26b, right), a small new re-entrant jet (red circle) is generated at the bottom wall.

During the break-off, as said previously, two clouds are formed. To explain it, let's take a closer look at the re-entrant jet evolution. In the previous section focused on single cloud cavitation, it has been found that the re-entrant jet is not a pure reverse flow in the x direction, it is also composed of vortices in the z direction. Here at T_0 + 2.8 ms, three strong vortices are detected on both V_y and the vorticity field (figures 2.27b&c), which will generate the two cloud detachments. The first vortex was formed at the cavity leading edge during the growing phase (from T_0 to T_0 + 1.6 ms), by the interaction between the re-entrant jet and the main flow. At time T_0 + 2 ms (figure 2.25), the vortex has become strong enough to create a significant lift and form the bulge. In addition, it is pushed downstream by

the main flow (see the local speed of about 7 m/s at T_0 + 2.4 ms). At the same time, a second vortex is created at the same initial position. At time T_0 + 2.8 ms, this second vortex is also pushed downstream, while a third vortex begins to form. The presence of the re-entrant jet creates favorable conditions for the convection of these 3 vortices, as it provides them with some additional energy en route. The strength of each vortex varies to some extent, depending on the magnitude of the re-entrant jet. When the vortex is not strong enough, as shown, for example at times T_0 + 1.2 ms and T_0 + 1.6 ms in figure 2.24, it will not generate a sufficient lifting effect to form a large bulge and lead to cloud shedding.

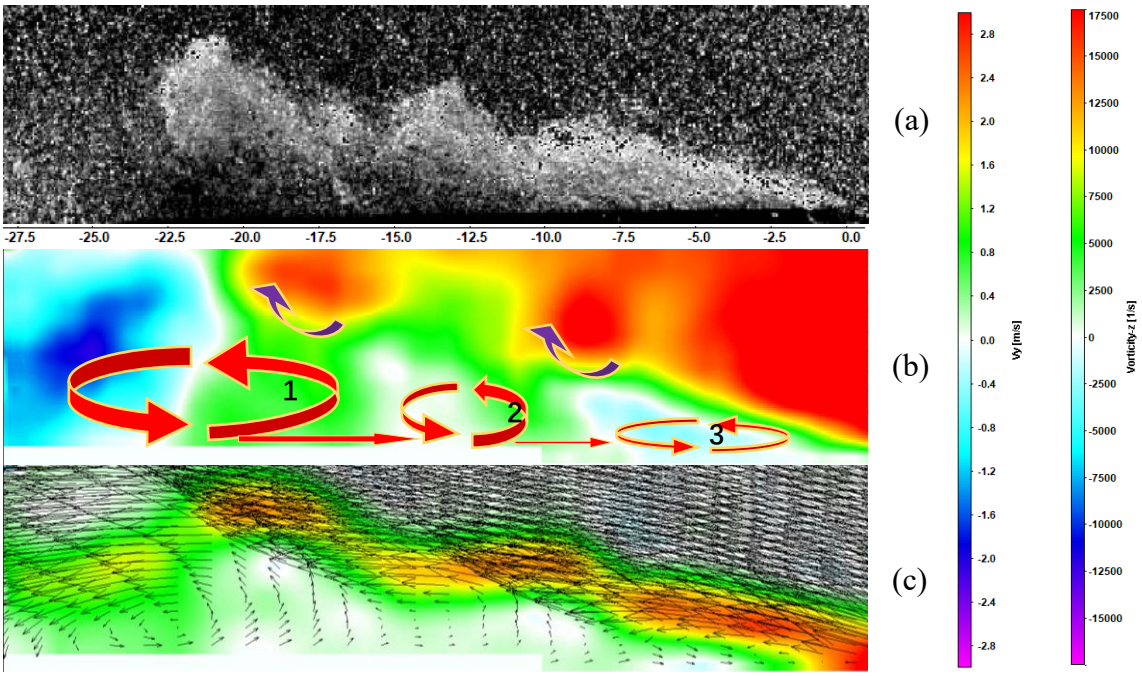

Figure 2.27. Structure of the re-entrant jet in a multi clouds configuration (test case #6) at T_0 + 2.8 ms, showing the mechanism of cloud formation. (a) shape of the sheet cavity, (b) V_y component, (c) vorticity field with velocity vectors.

As shown by the velocity field in the y direction, there is a strong lifting effect in the upper right of each vortex and a downward velocity component on the left side. This combination results in a stepped structure shown in the vorticity field, which enables the main flow to cut the cavity in between two vortices. At T_0 + 2.8 ms, this process has started as indicated by the red and blue circles (see the left of figure 2.26b), and it is completed at T_0 + 3.2 ms, when the clouds are detached. At time T_0 + 3.6 ms, the clouds of vapor have moved downstream, and the re-entrant flow has turned into a stronger

and thinner jet, as can be seen in the velocity field in the x direction (figure 2.26d), which is the starting point of a new cycle. Multi clouds cavitation is an extremely unstable situation that usually lasts for a few cycles. After that, the flow resumes to a single cloud periodical shedding configuration.

4.3 sheet cavitation

When the cavity is small, i.e. for test cases #1 to #3, no periodical instability is obtained, or the rear part of the cavity collapses before being detached, which makes the understanding of the flow evolution more challenging. Figure 2.28 shows a typical cavity evolution and V_x component of the velocity field from T_0 (start of the cavity growth) up to T_0 + 1.6 ms, for test case #3. Note that for these specific results, the interrogation window in the image post-processing has been decreased down to 16×16 pixels, to get more details in the area of the sheet cavity, which induces a significant increase of the uncertainty, up to 5 to 10%.

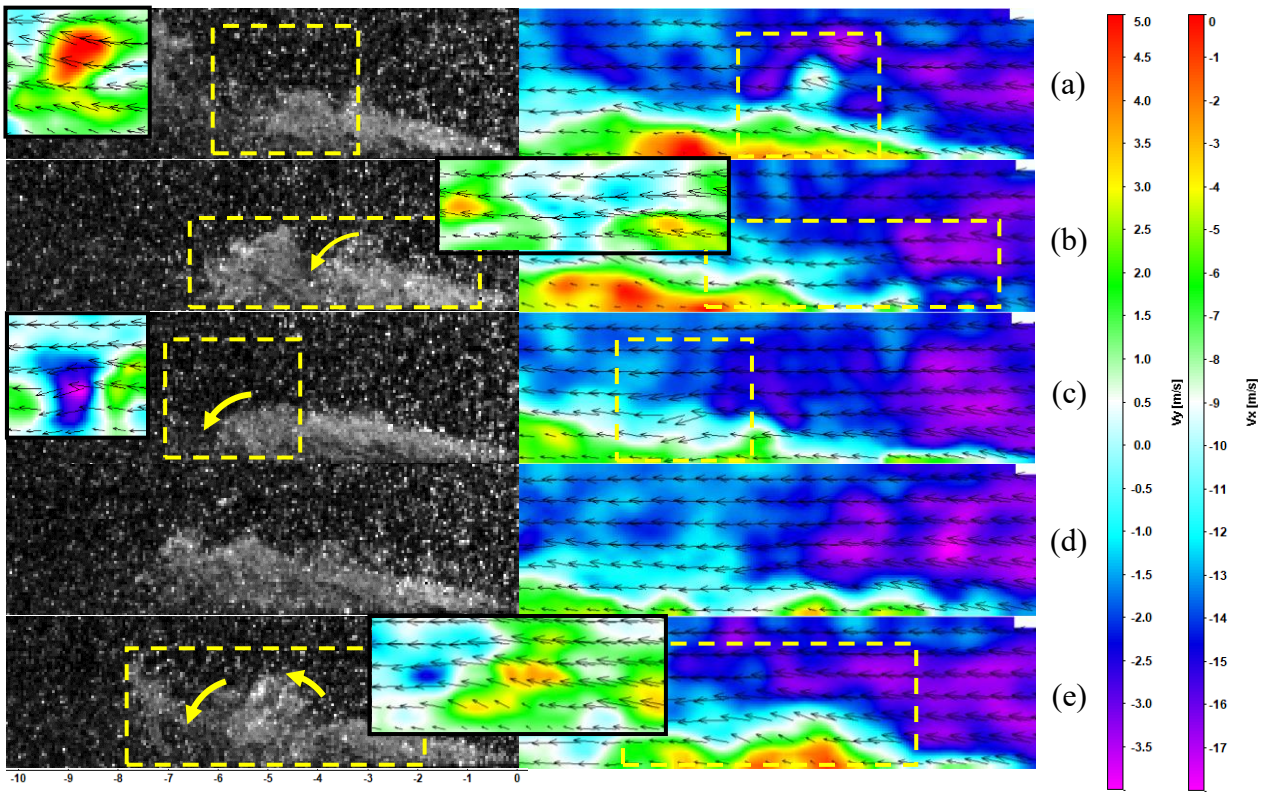

Figure 2.28. Sheet cavitation (test case #3): image of particles (left), V_x velocity component and velocity vectors (right) and V_y component (inserts).
(a) T_0, (b) T_0 +0.4 ms, (c) T_0 + 0.8 ms, (d) T_0 + 1.2 ms, (e) T_0 + 1.6 ms

It can be observed that the sheet cavity starts to grow at T_0 (figure 2.28a), forming a bulge-like structure at T0 + 0.4 ms (figure 2.28b). However, this bulge-like structure does not continue to develop into a detached, rotating cloud of vapor persisting during a significant time, like in the previous single- and multi-cloud cavitation cases. At T0 + 0.8 ms (figure 2.28c), this bulge-like structure is already detached from the main cavity and collapses before it can form a cloud (the collapse happens in less than 0.4 ms, so it is not captured at the 2500 fps frequency applied in PIV). Then it goes into the next "cycle" (figures 2.28d&e).

The velocity field in the x direction shows that during this process, there is no formation of re-entrant jet formation at all; however, there is a low (but still positive) velocity area close to the bottom wall. At T_0, a high-pressure is generated in this low-velocity area, resulting in a significant upward V_y component (see the yellow insert in figure 2.28a), which contributes to the formation of the bulge-like structure. At T_0 + 0.4 ms, a slightly downward V_y velocity component is generated between the bulge and the upstream part of the cavity (yellow insert in figure 2.28b), so the main flow begins to intrude into the low-speed region at the wall. At T_0 + 0.8 ms, this V_y flow velocity becomes stronger (yellow insert in figure 2.28c), which marks the full intrusion of the main flow, causing the low-speed area to shrink and eventually disappear. This mechanism prevents the production of vortices in the vicinity of the bottom wall. As a result, the cavity stays compressed against the bottom wall, and no detached cloud of vapor can be generated.

In this configuration, as the instability is milder and no re-entrant jet is generated, cavitation basically consists of an attached cavity at the venturi throat, and the downstream flow where some bubbles are just travelling and collapsing, with only minor effects on the baseline liquid flow. Note that a re-entrant jet is still generated intermittently, leading to minor shedding from time to time. However, these events do not induce any specific frequency, and are likely related to flow perturbations, such as fluctuations coming from the system of local roughness effects.

5. Conclusions

In this paper, the structure and instability of cavitating flows formed in the divergent part of a two-dimensional venturi have been analyzed using the velocity fields obtained from high-speed stereo PIV. It was shown that in spite of the small dimensions of the test section, the flow is quite two-dimensional, and the velocity fields obtained in different vertical planes from the center to the side of the channel were fairly identical.

Having access to the local flow velocity has enabled to propose a new objective definition for the length of the attached cavity, based on the length of the re-entrant jet or the value of the vorticity. The importance of measuring the pressure as close as possible to the cavitation area to define the cavitation number has been shown: in the present case, taking the average of the upstream and downstream pressures was found necessary to obtain all data points falling on the same curve for the evolutions of the cavity length or re-entrant jet length according to σ.

The comparison of the liquid and vapor time-averaged velocities at different positions has revealed two main areas of significant slip velocity between the two phases: (i) in the top half of the sheet cavity, where the largest vapor structures are not perfectly entrained by the liquid flow and have a lower speed, and (ii) the re-entrant jet area, where the intermittent nature of the jet, combined with the flow condensation at its tip, results in larger time-averaged velocities in the vapor, compared with the liquid.

By analyzing the flow time evolution, three different types of sheet/cloud cavitation were characterized, and some quantitative characterizations and qualitative analyses were carried out. Based on this study, an overview of these results is proposed here, focused on the primary mechanisms involved. As shown in figure 2.29, cloud cavitation is generally divided into four main stages: Growing, up-lift, cloud detachment, and cloud convection. At all steps, consistently with the recirculation cell model[13], the re-entrant jet plays a crucial role, since its structure and momentum trigger the flow evolution to the different behaviors.

As an extension to the re-entrant jet itself, the re-entrant region can be defined as the area between the mid-height of the cavity and the bottom wall, where the velocity is usually opposite to

the main flow, or still in the same direction but much lower (typically less than 10% of the liquid flow above the sheet cavity). In this region, therefore, the strong interaction of the re-entrant jet with the main flow forms a strong vortex close to the cavity leading edge (just downstream of the venturi throat, as shown in figure 2.29a). The friction between the main flow and the re-entrant region induces a periodical detachment of this vortex and transfers downstream to form a series of vortices within the re-entrant region. This series of vortices lift the upper cavity above the bottom wall, thus maintaining an almost steady cavity region. This is the first stage of cloud cavitation: the growing stage.

If the reverse jet vanishes (case of the non-periodical instability in figure 2.29c), the vortex at the leading edge of the re-entrant region runs out of energy and disappears. This area is then compressed by the intrusion of the main flow and collapses. On the contrary, if the re-entrant jet remains strong for a sufficient time, the detached vortex will grow dramatically as it moves downstream, forming a bulge (figure 2.29b), which initiates the up-lift stage. During this stage, the overall velocity of the re-entrant region decreases due to the growth of the vortex and bulge, becoming almost zero in the middle of the cavity (below the bulge).

As the detached vortex or bulge grows up to a certain scale, it reduces the cross-section of the main liquid flow over the cavity, thus increasing the local pressure and causing this liquid flow to deviate towards the gap between this vortex and the vortex at the leading edge of the re-entrant region, which results in the formation of a step-shaped re-entrant region. The single-cloud cavitation situation occurs when this mechanism perturbs the re-entrant jet at a point where no vortex at the leading edge of the re-entrant region is detached for a short period. However, when the re-entrant jet is strong enough, the action of the main flow is not sufficient to block the detachment of the next vortex, which will form a second high-intensity vortex. Then, because of the simultaneous lifting effects induced by these two vortices, a stair-stepping structure of the re-entrant region is obtained, as shown in figure 2.29e. This is the double cloud detachment typical of multi-cloud cavitation. In some cases, three clouds can even occur simultaneously, but this is a rare situation.

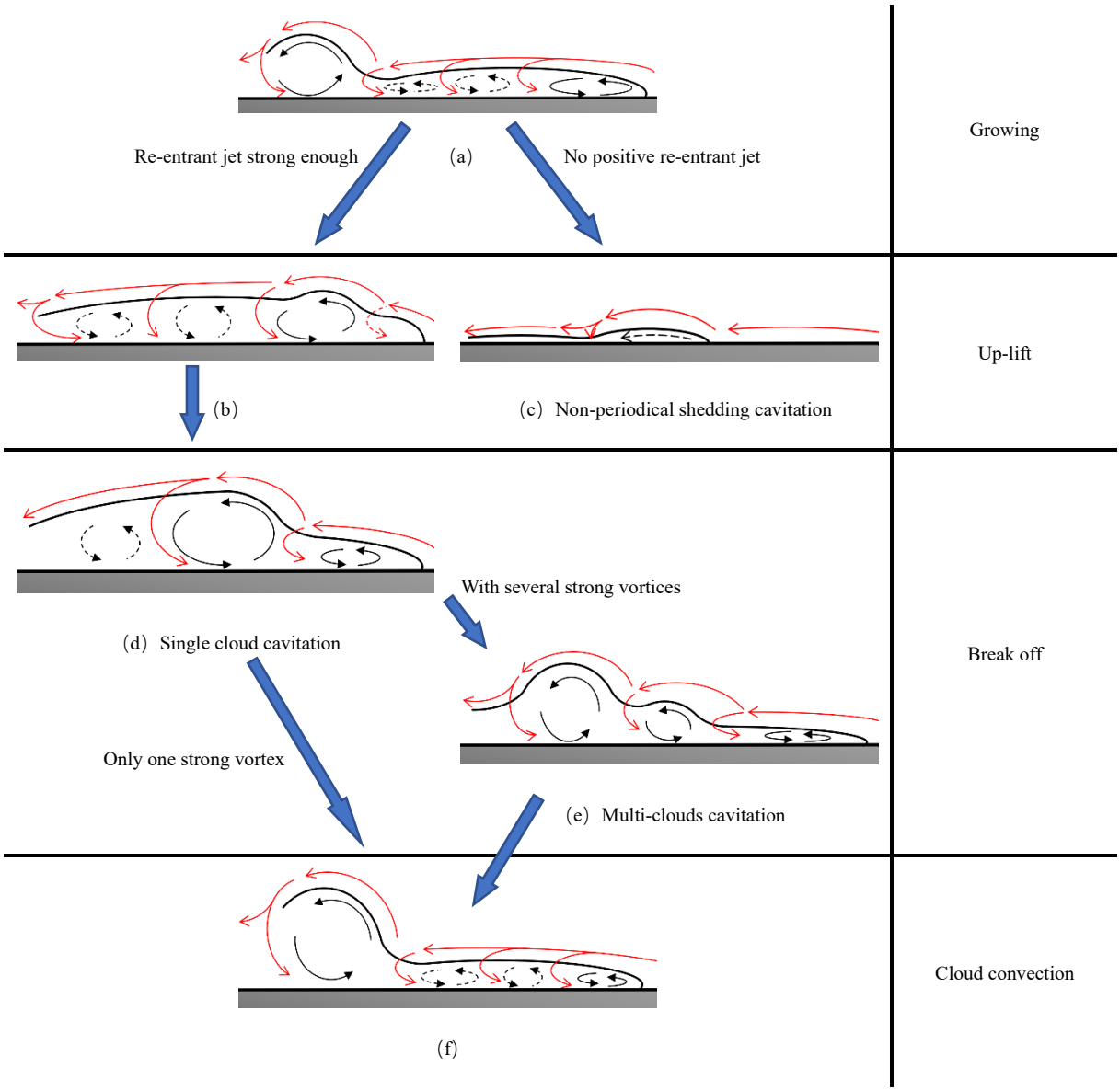

Figure 2.29. Schematic representation of the different steps in the three different types of behaviors shown in section 4

(a) growing stage, (b) bulge forming, (c) non-periodical shedding cavitation, (d) single cloud cavitation, (e) multi-clouds cavitation, (f) cloud convection

After that, in both cases of single-cloud and multi-cloud cavitation, the step-like structure is pushed downstream, and a new re-entrant region is created upstream. This “cloud convection” step is the final stage of the cycle (figure 2.29f).

References

[1] Dular M, Khlifa I, Fuzier S, et al. Scale effect on unsteady cloud cavitation[J]. Experiments in fluids, 2012, 53(5): 1233-1250.

[2] Furness R A, Hutton S P. Experimental and theoretical studies of two-dimensional fixed-type cavities[J]. 1975.

[3] Stutz B, Reboud J L. Experiments on unsteady cavitation[J]. Experiments in fluids, 1997, 22(3): 191-198.

[4] Arndt R E A, Song C C S, Kjeldsen M, et al. Instability of partial cavitation: a numerical/experimental approach[J]. 2000.

[5] Laberteaux K R, Ceccio S L. Partial cavity flows. Part 1. Cavities forming on models without spanwise variation[J]. Journal of Fluid Mechanics, 2001, 431: 1-41.

[6] Laberteaux K R, Ceccio S L. Partial cavity flows. Part 2. Cavities forming on test objects with spanwise variation[J]. Journal of Fluid Mechanics, 2001, 431: 43-63.

[7] Dular M, Bachert B, Stoffel B, et al. Relationship between cavitation structures and cavitation damage[J]. Wear, 2004, 257(11): 1176-1184.

[8] Coutier-Delgosha O, Stutz B, Vabre A, et al. Analysis of cavitating flow structure by experimental and numerical investigations[J]. Journal of Fluid Mechanics, 2007, 578: 171-222.

[9] Pham T M, Larrarte F, Fruman D H. Investigation of unsteady sheet cavitation and cloud cavitation mechanisms[J]. 1999.

[10] Park J T, Cutbirth J M, Brewer W H. Hydrodynamic performance of the large cavitation channel (LCC)[C]//Fluids Engineering Division Summer Meeting. 2003, 36975: 87-100.

[11] Knapp R T, Daily J W, HAMMITT F. G. 1970 Cavitation[J]. McGraw-Hill Book Company, London.

[12] Stanley C, Barber T, Rosengarten G. Re-entrant jet mechanism for periodic cavitation shedding in a cylindrical orifice[J]. International Journal of Heat and Fluid Flow, 2014, 50: 169-176.

[13] Zhang H, Zuo Z, Mørch K A, et al. Thermodynamic effects on Venturi cavitation characteristics[J]. Physics of Fluids, 2019, 31(9): 097107.

[14] Callenaere M, Franc J P, Michel J M, et al. The cavitation instability induced by the development of a re-entrant jet[J]. Journal of Fluid Mechanics, 2001, 444: 223-256.

[15] Stutz B, Reboud J L. Experiments on unsteady cavitation[J]. Experiments in fluids, 1997, 22(3): 191-198.

[16] Leroux J B, Coutier-Delgosha O, Astolfi J A. A joint experimental and numerical study of mechanisms associated to instability of partial cavitation on two-dimensional hydrofoil[J]. Physics of fluids, 2005, 17(5): 052101.

[17] Gopalan S, Katz J. Flow structure and modeling issues in the closure region of attached cavitation[J]. Physics of fluids, 2000, 12(4): 895-911.

[18] Foeth E J, Van Doorne C W H, Van Terwisga T, et al. Time resolved PIV and flow visualization of 3D sheet cavitation[J]. Experiments in Fluids, 2006, 40(4): 503-513.

[19] Kravtsova A Y, Markovich D M, Pervunin K S, et al. High-speed visualization and PIV measurements of cavitating flows around a semi-circular leading-edge flat plate and NACA0015 hydrofoil[J]. International Journal of Multiphase Flow, 2014, 60: 119-134.

[20] Dular M, Bachert R, Stoffel B, et al. Experimental evaluation of numerical simulation of cavitating flow around hydrofoil[J]. European Journal of Mechanics-B/Fluids, 2005, 24(4): 522-538.

[21] Dular M, Bachert R, Schaad C, et al. Investigation of a re-entrant jet reflection at an inclined cavity closure line[J]. European Journal of Mechanics-B/Fluids, 2007, 26(5): 688-705.

[22] Khlifa I, Vabre A, Hočevar M, et al. Fast X-ray imaging of cavitating flows[J]. Experiments in fluids, 2017, 58(11): 1-22.

[23] Zhang G, Khlifa I, Coutier-Delgosha O. A comparative study of quasi-stable sheet cavities at

different stages based on fast synchrotron x-ray imaging[J]. Physics of Fluids, 2020, 32(12): 123316.

[24] Ganesh H, Mäkiharju S A, Ceccio S L. Bubbly shock propagation as a mechanism for sheet-to-cloud transition of partial cavities[J]. Journal of Fluid Mechanics, 2016, 802: 37-78.

[25] Lush P A, Peters P I. Visualisation of the cavitating flow in a venturi type duct using high-speed cine photography[C]//Proceedings of the IAHR conference on operating problems of pump stations an power plants. 1982: 1-13.

[26] Pipp P, Hočevar M, Dular M. Numerical insight into the kelvin-helmholtz instability appearance in cavitating flow[J]. Applied Sciences, 2021, 11(6): 2644.

[27] Zhang G, Zhang D, Ge M, et al. Experimental investigation of three distinct mechanisms for the transition from sheet to cloud cavitation[J]. International Journal of Heat and Mass Transfer, 2022, 197: 123372.

[28] Leroux J B, Coutier-Delgosha O, Astolfi J A. A joint experimental and numerical study of mechanisms associated to instability of partial cavitation on two-dimensional hydrofoil[J]. Physics of fluids, 2005, 17(5): 052101.

[29] Fuzier S, Coudert S, COUTIER D. O. Two phase velocity measurements using LIF-PIV inside the cavitation sheet generated in a venturi[C]//of: 8 th International Conference on Multiphase Flow ICMF. 2013: 26-31.

[30] Ge M, Zhang G, Apte D, et al. Analysis of the slip velocity between the two phases in a high-speed cavitating flow[C]//APS Division of Fluid Dynamics Meeting Abstracts. 2021: M29. 003.

CHAPTER III. EXPERIMENTAL INVESTIGATION OF THREE-DIMENSIONAL EFFECTS IN CAVITATING FLOWS WITH TIME-RESOLVED STEREO PARTICLE IMAGE VELOCIMETRY

Kunpeng Long[1], *Olivier Coutier-Delgosha[1, 2], Annie-Claude Bayeul-Lainé[1]

[1] *Univ. Lille, CNRS, ONERA, Arts et Metiers Institute of Technology, Centrale Lille, UMR 9014 - LMFL - Laboratoire de Mécanique des Fluides de Lille - Kampé de Fériet, F-59000 Lille, France*

[2] *Virginia Tech, Kevin T. Crofton Dept of Aerospace & Ocean Eng., Blacksburg VA 24060, USA*

Abstract

The present paper is devoted to characterizing the three-dimensional effects in a cavitating flow generated in a Venturi-type profile. Experimental measurements based on 2D3C(Two-dimensional-three-component) stereoscopic PIV(Particle Image Velocimetry) are conducted to obtain the three components of the velocity field in multiple vertical planes aligned with the main flow direction, from the center of the channel to the side walls. Time-resolved acquisitions are conducted, so not only time-averaged quantities but also velocity fluctuations can be discussed. The attention was focused on configurations of cloud cavitation, where the attached cavity experiences large-scale periodical oscillations and shedding of clouds of vapor. Although the water channel is purely two-dimensional, some significant flow velocities in the third direction (depth of the test section) were measured. Some of those velocities were found to be related to small differences between the boundary conditions on the two sides, such as minor gaps between the sides and the bottom wall, while others reflect intrinsic three-dimensional mechanisms inside the cavitation area, such as side jets that contribute to the periodical instability process. These mechanisms are discussed, and a possible 3D(Three-dimensional) structure of the cavitating flow is proposed.

Keywords: Cavitation, instability, flow imaging, PIV, 3D effects

* Corresponding author, ocoutier@vt.edu

Chapitre III. Etude experimentale des effets tridimensionnels dans les ecoulements cavitation a l'aide de la vélocimétrie stéréo à image de particules resolue en temps(Français)

Dans le chapitre 3, l'effet 3D sur le même cas est analysé. La revue de la littérature met en évidence le manque d'études expérimentales sur l'écoulement local et le mécanisme 3D de la cavitation instationnaire. La présentation de la section expérimentale et de la méthode de mesure est presque identique à celle du chapitre 2. Les résultats commencent par les conclusions du chapitre 2 sur la cavitation mono / multi-nuages et en nappe. Une fois encore, il est indiqué qu'il existe une relation entre l'intensité et l'échelle des structures tourbillonnaires et le type de cavitation obtenu. La frontière entre chaque type de cavitation est en quelque sorte difficile à prévoir, c'est pourquoi les cas de ce chapitre sont sélectionnés lorsque le physique est dominant. La principale limite de cette étude est que les plans verticaux ne sont pas pris simultanément, donc aucune structure 3D ne peut être extraite des mesures PIV, et les résultats sont basés sur l'écoulement moyen. Cependant, la turbulence peut jouer un rôle majeur dans la dynamique de la cavitation.

Ce chapitre a fait l'objet d'un article de journal : *Kunpeng Long; Olivier Coutier-Delgosha; Annie-Claude Bayeul-Lainé Experimental investigation of three-dimensional effects in cavitating flows with time-resolved stereo Particle Image Velocimetry, Physics of Fluid, 2023-02-02 | Journal article, DOI: https://doi.org/10.1063/5.0136242*

Résumé :

Le présent article est consacré à la caractérisation des effets tridimensionnels dans un écoulement cavitant généré dans un profil de type Venturi. Des mesures expérimentales basées sur la vélocimétrie par image de particules 2D3C sont effectuées pour obtenir les trois composantes du champ de vitesse dans plusieurs plans verticaux alignés avec la direction principale de l'écoulement, du centre du canal aux parois latérales. Des acquisitions résolues dans le temps sont effectuées, de sorte que non seulement les quantités moyennes dans le temps mais aussi les fluctuations de vitesse peuvent être discutées. L'attention s'est portée sur les configurations de cavitation nuageuse, où la cavité attachée subit des oscillations périodiques à grande échelle et le déversement de nuages de vapeur. Bien que le canal d'eau soit purement bidimensionnel, certaines vitesses d'écoulement significatives dans la troisième direction (profondeur de la section d'essai) ont été mesurées. Certaines d'entre elles sont

liées à de petites différences entre les conditions limites des deux côtés, telles que des écarts mineurs entre les côtés et la paroi inférieure, tandis que d'autres reflètent des mécanismes tridimensionnels intrinsèques à l'intérieur de la zone de cavitation, tels que des jets latéraux qui contribuent au processus d'instabilité périodique. Ces mécanismes sont discutés et une structure 3D possible de l'écoulement cavitant est proposée.

Conclusion :

Dans cet article, une analyse de la structure d'écoulement 3D à l'intérieur de la zone de cavitation générée sur un profil Venturi 2D a été étudiée en utilisant la PIV 2D3C. Les trois composantes du champ de vitesse moyenné dans le temps ont été étudiées dans différents plans y-z depuis le bord d'attaque jusqu'à l'extrémité aval de la cavité en feuille, et dans des plans x-z situés à différentes hauteurs depuis la surface du fond jusqu'à la jonction avec l'écoulement de liquide pur. Un jet puissant, allant des côtés vers le centre, a été détecté dans la zone de vaporisation intense juste en aval de la gorge du Venturi. Ce jet remonte vers l'interface supérieure de la cavité avec l'écoulement principal de liquide, contribuant à l'accélération locale détectée dans les études précédentes à l'interface feuille-cavité. Il a été montré que ce jet résulte de la déviation du flux entrant induite par le jet rentrant, qui tourne en atteignant le col : plus le flux inverse est fort, plus la déviation du flux vers le centre est importante.

Plus en aval, ce jet latéral descend, en raison de la pression plus élevée générée à l'avant du "renflement" induit par le soulèvement de la partie arrière de la cavité attachée (détaillé par Long et al.16), coupant finalement la cavité aux positions où le jet rentrant est le plus faible, et provoquant ainsi la rupture de la cavité et le détachement d'un nuage de vapeur à grande échelle.

Des mécanismes supplémentaires ont été signalés en aval de la rupture de la cavité, en raison de la rotation du nuage de vapeur dans le sens inverse des aiguilles d'une montre. Deux tourbillons tournant le long de l'axe x ont été identifiés sur les côtés du nuage, générant une structure tridimensionnelle complexe. Dans l'ensemble, des mécanismes tridimensionnels importants ont été détectés, certains d'entre eux contribuant directement à l'instabilité de l'écoulement, bien que la configuration de l'écoulement soit purement 2D.

1.Introduction

Although cavitation dynamics has been studied extensively in the last decades, using both experiments and computations, all the mechanisms in play in the instabilities generated by cavitating flows are far from being elucidated. One of the reasons is that even cavitation on simple bodies like two-dimensional profiles often exhibits complex behaviors, combining large-scale periodical shedding (called cloud cavitation) and high-frequency turbulent effects. The role of the re-entrant jet in the low-frequency flow instability has been shown for a long time[1, 2], but cases where a strong jet was observed, although no cloud cavitation was obtained, were also reported[3], while other mechanisms contributing to the instabilities were also discussed. For example, the role of bubbly shock propagation was highlighted by Ganesh et al. in 2017[4], and the presence of a strong Kelvin-Helmholtz instability at the cavity interface was shown recently by Podbevsek et al. 2021[5]. How these various processes combine and how much each of them triggers the flow unsteadiness are still open questions, and the responses likely depend on the flow conditions.

Even the flow organization is not clear, as its investigation is challenged by the fluctuations at various scales and the opaque nature of cavitation. High-frequency acquisitions are needed to access a time-resolved information: in the range of hundreds/thousands of Hz to capture the large-scale shedding, up to 100 kHz to track individual bubbles. It has induced, until recently, some strong limitations for non-intrusive optical techniques of investigation, such as Particle Image Velocimetry (PIV). Other limitations come from the difficulty of getting optical access to the areas of interest. Laser light sheets are distorted by the reflection of the beams on the bubble interfaces, and all bubbles between the laser light sheet and the camera form a mask that prevents any good quality measurement. Therefore, a lot of studies have been focused on the investigation of cavity wakes[6, 7] where the void fraction is low, boundary layers on the side walls[8], or just the liquid flow outside from the cavitation area[9].

The basic structure of the flow in a cavity attached to a solid wall was first described by Knapp et al. 1970[10] and later discussed in various publications: in the cavity closure, the external flow forms a jet impinging obliquely upon the wall. It results in two separate streams (see figure 3.1), one flowing upstream and later contributing to the cavity break-off, once it has reached the cavity front end, and

the second one re-attaching to the wall downstream[11].

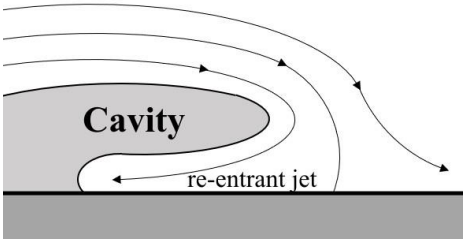

Figure 3.1. Schematic representation of the re-entrant jet flow in the closure region of an attached cavity

The re-entrant jet has been observed and measured several times using optical probes[12], electrical probes[13], laser-based PIV[14], and x-ray imaging-based PIV[3, 15]. Recent work by the present authors has revealed that this jet does not consist only of an intermittent negative speed in the main flow direction; instead, it has a more complex structure[16]. Measurements based on optical PIV in a small-scale venturi profile show that it is composed of a series of vortices generated at the cavity upstream end, which roll downstream and eventually form a step-shaped structure that will result in the cloud of vapor. This study suggests that significant three-dimensional effects, in addition to the purely 2D description of the cavity behavior, might play a role in the flow unsteadiness.

Studies focused on 3D effects can hardly be found in the literature. In an early theoretical study, Johnson(1961) combined solutions for several planar flows, using corrections derived from aerodynamics, to obtain a solution for a finite aspect ratio hydrofoil[17]. Numerical simulations are now providing 3D results, but a high level of inaccuracy still affects most of the calculations of cavitating flows. The global unsteady behavior of the cavity can usually be reproduced, as well as the time-averaged velocity fields, using advanced turbulence models like LES[18], but the local flow characteristics are often not consistent with the experimental data[19]. Nevertheless, Decaix & Goncalves have compared 2D and 3D simulations of cloud cavitation in a 2D venturi-type section, and they found that the 3D calculations provided a better agreement with the experimental data regarding the global frequency of the fluctuations, as well as the time-averaged velocity values in the flow direction and void fraction[20]. Some secondary structures generated in corners of the test sections

were found in these simulations: a strong jet toward the center of the channel was observed, forming a vortex (see figure 3.2).

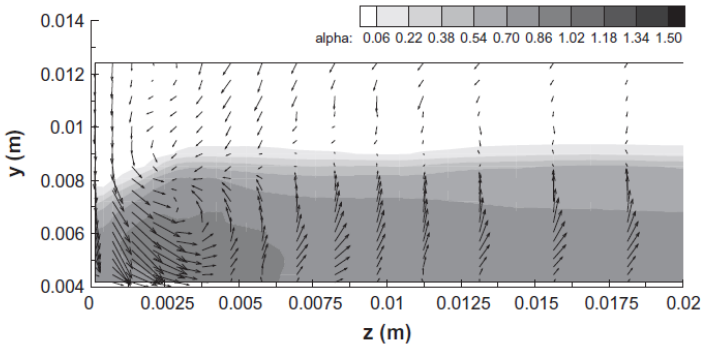

Figure 3.2. Snapshot of the void ratio and the velocity vectors in a transverse cutting plane, downstream of a venturi throat, obtained by Decaix and Goncalves[20]

On the experimental side, only a few notable studies have focused on the 3D structure of cavitation. Visualization from the side and the top was performed by Callenaere et al. in 2001, to observe the development of the reverse flow and the related events[11], but it did not provide any detailed information on the flow structure. More recently, Prothin et al. have recorded high-speed videos from the top of the cavity on a NACA0015 foil, and processed the data using POD and DMD. They observed a series of three-dimensional vortices formed by the lateral motion of the cloud of vapor[21]. However, the role played by these vortices in the mechanisms of the flow instability is not elucidated yet.

Indeed, experimental investigations of the 3D flow organization are challenging, as optical imaging, which is now the most usual technique of velocimetry in single-phase flows, is difficult to apply in cavitating flows. More specifically, Particle Image Velocimetry does not provide any accurate results in areas where the void fraction is higher than a few percent because of (i) the opacity of the liquid/bubbles mixture, which makes the particles difficult to see, and (ii) the light reflection on the bubbles, which deforms the laser light sheet. The second effect can be drastically reduced by using fluorescent particles associated with notch filters on the cameras to record only the fluorescence emitted by the particles and filter the laser light. It has been used by several groups in the 2 last decades to measure the liquid velocities in areas of small void fraction, such as cavity wakes[9, 22, 23].

However, the first effect has no solution, unless the laser light sheet is located very close to one side wall, so that the fluorescence can be detected[14, 24]. This is the case when cavitation is studied at a small scale, like in Venturi-type sections of a few millimeters in depth and height[25]. In such a configuration, accurate 2D2C PIV results could be obtained and used to discuss the cavitation instabilities. Comparisons of cavitating flows generated at different scales have shown that similar instabilities are obtained, although the quality of the finish of the surfaces is crucial at a small scale to avoid any side effect.

In the present study, cavitating flows in a small-scale 2D Venturi type section are investigated using 2D3C (two-dimensional – three components) PIV, in order to characterize the three-dimensional patterns specific to attached cavitation on a solid body. Section 2 presents the experimental setup and the measurement accuracy, while section 3 is focused on the flow structure, and section 4 is on the discussion of the results.

2. Experimental setup and measurements

2.1 Test Rig

Cavitation tests were conducted in a small-scale cavitation tunnel schematically represented in figure 3.3. This tunnel was designed for the particular purpose of velocimetry in a cavitating flow by ultra-fast X-ray imaging. All details related to the conception of the cavitation tunnel can be found in Khlifa et al.[15].

Water circulation is obtained with a Salmson-type Multi HE1602-SE-T/2-2G pump with variable rotation speed controlled by a micro-AC Variable Frequency Drive (VFD) model GS2-45P0 to set the flow rate. A tank partially filled with the circulation water is used for water cooling at the pump delivery to maintain a constant temperature, using a secondary cooling loop. The volume flow rate is measured by a Bürkert type SE32 (uncertainty 0.15 l/min after in situ calibrations) turbine flow meter. Temperature is obtained with a type K thermocouple, directly in contact with circulation water.

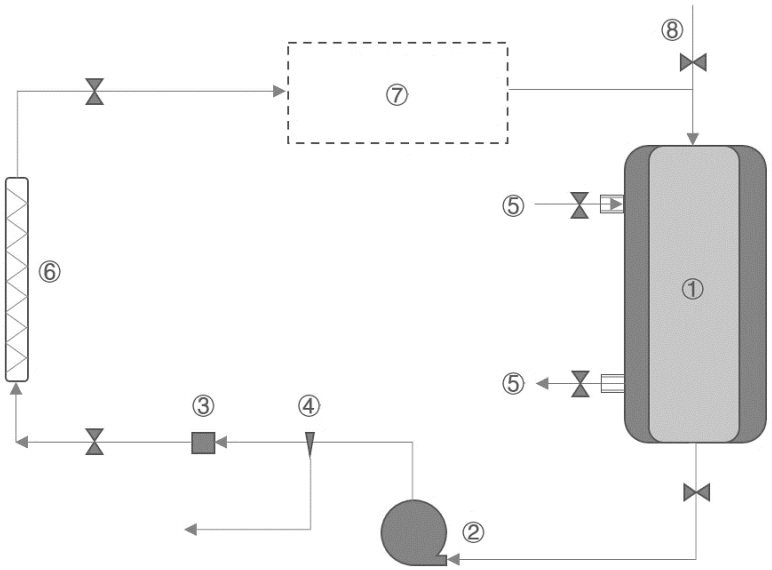

1) Water tank
2) Circulation pump
3) Flow meter
4) Temperature meter
5) Cooling system
6) Heater
7) Test section
8) Vacuum pump

Figure 3.3. Cavitation test facility

Upstream from the test section, a noise attenuation device is used to filter the periodical pressure fluctuations due to the passage of the pump blades. The reference pressure is measured 10 mm upstream from the venturi test section with a Series 6M/S(C) OEM pressure transducer connected to an EV 94 EB digital indicator. The uncertainty on the measurements was of the order of 50 Pa. Another pressure meter measures the downstream pressure 10mm downstream from the test section. The partially filled tank is connected to a compressor and a vacuum pump, which enables variation in the pressure in this tank between 0.1 bar and 3.5 bar, thus adjusting the pressure in the test section.

2.2 Venturi-type Section

The geometry of the test section is similar to the one used previously at a larger scale by Stutz and Reboud at a larger scale to characterize the re-entrant jet in cloud cavitation[1] or Dular et al. to perform PIV measurements close to the side walls[26]. Here, a small-scale version of the Venturi profile is used, like in our previous experiments based on X-ray imaging[15, 27].

The main body of the test section is 3D printed, while the bottom, top, and side walls of the

convergent/divergent nozzle are inserts made of transparent optical glass (figure 3.4). The venturi shape (bottom wall) is a simple wedge: the flow is accelerated in the convergent part of the venturi, which has an 18° angle. The maximum speed at the throat (width 5 mm, height 10 mm) is in the range of 10 to 20 m/s. Cavitation is initiated immediately downstream from the edge of the Venturi, which has an 8° divergence angle, and it collapses abruptly as the fluid moves outwards since the pressure re-increases downstream.

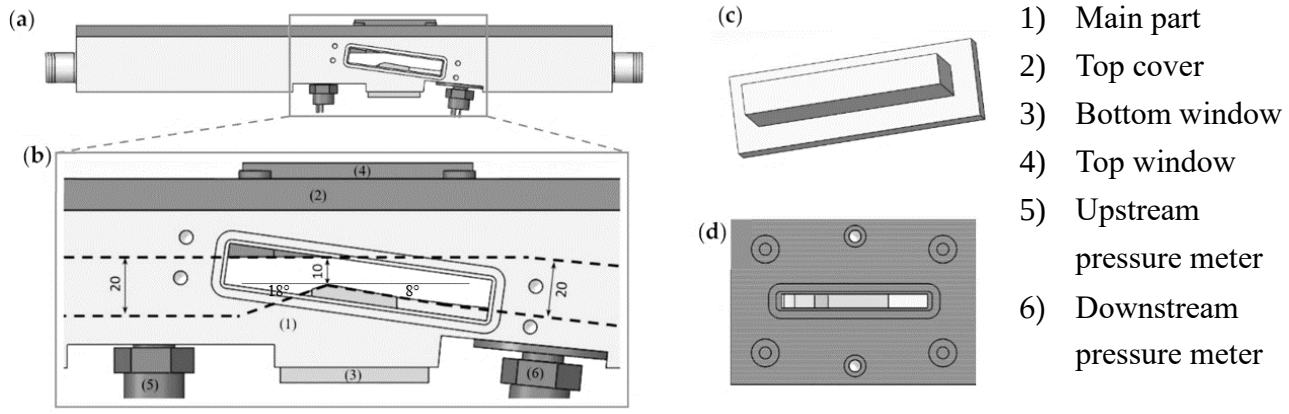

Figure 3.4. Venturi-type section: (a, b) side views, (c) side window, (d) top view of the top window

2.3 PIV measurements

The flow field is illuminated from the top with a vertical light sheet generated with a DM150-532-DH dual-head Nd: YAG laser from Photonics Industries (figure 3.5). The light sheet is about 1 mm thick and is located in the middle of the test section. The flow is seeded with PMMA-RhB-Frak Fluorescent tracers with an average 10 µm diameter, which re-emit light at a 584 nm wavelength significantly higher than the original 527 nm of the laser.

Two Phantom v2512 high-speed cameras were used to capture simultaneous images one side of the test section, as shown in figure 3.5 (see the yellow rectangle that shows the area of interest). The cameras are equipped with notch filters that eliminate the wavelengths around 527 nm in order to capture only the light emitted by the particles. It enables the removal of the reflections of the laser light on the cavitation bubbles while capturing the images of particles. The bright spot generated by

each particle is typically 20 to 50 µm, i.e., 1 to 2 pixels on the images. Note that it is about 2 to 5 times the size of the particles only, as the spot is due to the fluorescence emitted by the particles, not the reflection of the incident light, so the halo generated by each particle is significantly smaller.

The two cameras are oriented with an angle of around 25 to 30 degrees from the direction perpendicular to the windows, which was found to be the best compromise between the accuracy of the velocity 3rd component and the sharpness of the images.

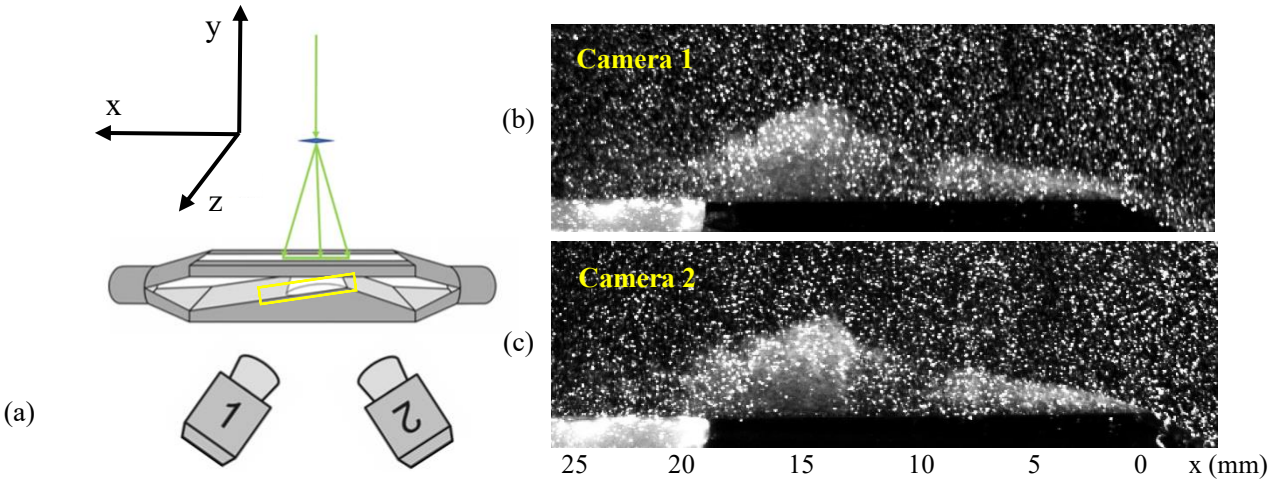

Figure 3.5. (a) scheme of the PIV setup, (b, c) Raw images of particles obtained simultaneously with the two cameras of the yellow area

For each flow condition, 20,000 8-bit pictures with a resolution of 768 x 480 pixels were recorded by the two cameras with an exposure time of about 200 ns (duration of the laser flash). These 20,000 pictures are composed of 10,000 times two frames separated by 5 µs, acquired at a frequency of 25,000 Hz in order to time resolve the motion of the vapor structures in the flow field. So the total time of acquisition is 0.4s. The 5 µs time between the two frames corresponds to a typical displacement between 0.5 and 2 pixels in most of the flow field, which is smaller than the usual prescriptions for PIV, but enabled in this specific case to minimize the uncertainties.

The cameras and the laser were synchronized with a high-speed controller, and the images were recorded using the Davis LaVision 10.0 software.

To perform measurements in the different vertical planes in the z-direction (see figure 3.5), the

test section is mounted on a sliding frame controlled with a micrometric screw of precision 0.01 mm, to adjust precisely the laser light sheet position from the front side to the backside (5 mm distance with 0.5 mm between two successive positions). This setup enables moving only the test section without changing anything in the PIV setup. Note that the test section was fixed rigidly to the frame so that only the entire frame could slide, but no other motion was enabled, which was critical for the accuracy of the calibration.

A thorough calibration process was performed once the laser light sheet, camera fields of view, and image sharpness were adjusted: the test section was moved so that the light sheet was at the middle of the channel, then the top (see figure 3.3b) was open to the air, but still maintained full of water. A micro calibration plate from LaVision (200 µm distance between the dots, covering the 30×10 mm^2 surface of the field of view) was inserted into the test section and used to record the calibration data. The micrometric screw was used to move the test section to the front and back for the stereo PIV calibration. Once the process was completed, the test section was closed for measurements.

2.4 Test cases

Four flow conditions were investigated, as reported in Table 3.1. Only the flow rate Q was changed, while the pressure in the downstream tank was maintained at atmospheric pressure. It results in 4 values of the cavitation number $\sigma = \left(P_{up} - P_v\right)/\frac{1}{2}\rho V_{th}^2$, where V_{th} is the mean speed at the Venturi's throat, P_{up} is the pressure upstream from the test section, P_v is the vapor pressure, and ρ is the liquid density.

	Temp (°C)	Pv (Pa)	ρ (kg/m3)	V_{th} (m/s)	Q (l/min)	Area (mm^2)	σ	P_{up} (Pa)	P_{down} (Pa)
1	23	2807	997.541	15	45	50	1.19	136500	98800
2	23	2807	997.541	16	48	50	1.06	138000	98100
3	23	2807	997.541	17	51	50	1.00	147000	97300
4	23	2807	997.541	18	54	50	0.95	156500	96600

Table 3.1. Investigated cavitation conditions

For each flow condition, 9 laser sheet positions in the z direction were investigated, from 0.5mm off the back side window(P1) to 0.5mm off the front side window (P9).

2.5. PIV post-processing

To enhance the quality of the images of particles inside the cavitation areas, a pre-processing was applied to eliminate, as much as possible, the traces of the cavitation bubbles. It is based on particle brightness standardization and background filter, and it enabled to obtain a quite uniform brightness of the particles in the entire flow field (see figure 3.6).

The vector fields are calculated from the images of particles using the Davis 10.0 software from LaVision. Interrogation areas of 64×64 pixels with 50% overlap are applied for the first 2 passes, and then 16×16 pixels windows with 75% overlap for the last 3 passes. Vectors with a correlation factor lower than 0.6 or a Q factor lower than 1.3 were removed from the results. The final results are smoothed by applying a 3×3 Gaussian kernel.

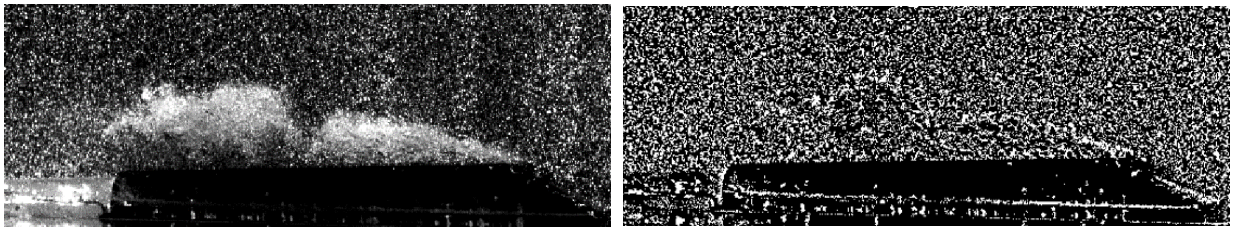

Figure 3.6. Raw image of particle (left) and processed image used for PIV (right)

Figure 3.7 displays the typical distributions of correlation factors, peak ratios, and uncertainty obtained for the three components of the velocity in test case #4. Note that it is shown here at a given time, for the sheet cavity shown in figure 3.7f, but the levels remain very similar for all PIV results obtained in this experiment. The uncertainty on V_x is systematically smaller than 2% in the entire field of view, while the one on V_y is smaller than 1%. Higher values are obtained for V_z, with peaks in the range of 4 to 5%, but most of the data still have an uncertainty lower than 3%. In addition, the correlation factors are always higher than 0.7, and the peak ratio is always higher than 2.

This level of accuracy, which is consistent with previous PIV campaigns performed on the same geometry with a different system working at lower frequency[16] is considered good enough to analyze hereafter the three-dimensional structure of the flow field and discuss the impact of the 3D effects.

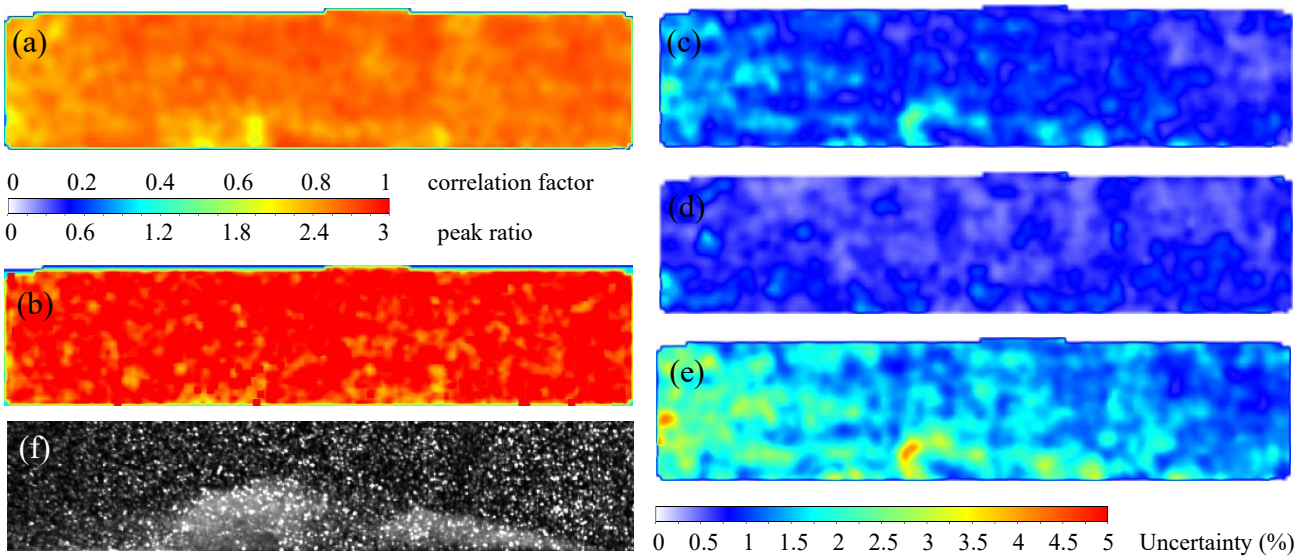

Figure 3.7. Typical distributions of (a) correlation factor, (b) peak ratio, (c) uncertainty on V_x, (d) uncertainty on V_y, (e) uncertainty on V_z in test case #4, for the sheet cavity indicated in (f).

The quantity of image pairs to be used to calculate the time-averaged velocity fields was selected based on a convergence study shown in figure 3.8. Two specific locations are considered here: (a) inside the cloud of vapor, once it is detached from the attached cavity, and (b) inside the attached cavity, in the area where the re-entrant jet is flowing upstream. In both cases, a satisfactory convergence was obtained on V_x and V_y with about 6000 pairs of images, while 8000 is required for V_z. Therefore, 10,000 pairs of images were eventually used for all time-averaged velocity fields used hereafter to discuss the 3D structure of the flow field.

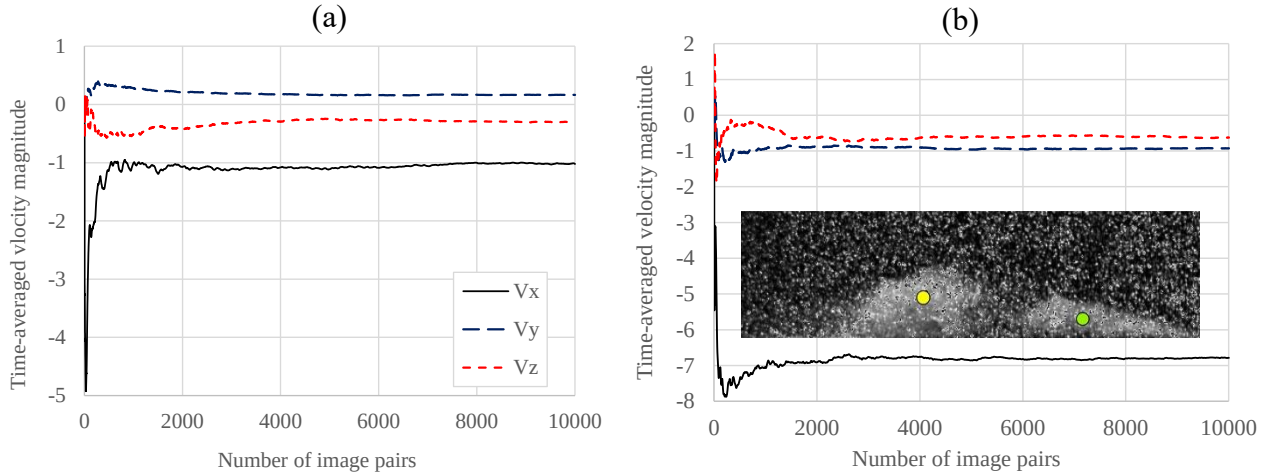

Figure 3.8. Convergence of the time averaged velocity components according to the number of image pairs: (a) at the location of the cloud detachment (yellow dot), (b) in the re-entrant jet (green dot).

3. Results

3.1 General unsteady behavior

The flow behaviors observed in the present experiment are the same as those described in a previous paper by Long et al.[16], with three different types of sheet instabilities: (1) single cloud cavitation, (2) multi-clouds cavitation, and (3) sheet cavitation.

For small-size sheet cavities, type (3) is dominant, with random shedding of small clouds of bubbles in the wake of the cavitation area, but no clear periodic detachment. It is associated with a very weak re-entrant jet at the bottom wall, which can hardly flow up to the upstream end of the cavity. For larger sheet cavities, periodical shedding of large-scale clouds of vapor is obtained, with four distinct steps (cavity growing, cavity up-lift, cavity break-off, cloud convection) described in detail by Long et al.[16]. The re-entrant jet plays a crucial role in that process, as can be seen in figure 3.9, which shows the typical four stages of the cavity (images a to d).

Figure 3.9a shows the growing stage, where a continuous cavitation region is formed downstream from the Venturi's throat. The Vx velocity component (color field), as well as the velocity vectors, show a thin re-entrant jet flowing upstream along the bottom wall (note that positive Vx values here correspond to the re-entrant jet), forming a series of vortices in the bottom half of the sheet cavity (not shown here). This series of vortices gradually merge while the thickness of the re-entrant jet increases, forming a bulge-like structure, as shown in figure 3.9b (up-lift stage). When this bulge grows to a certain level, the re-entrant jet weakens in between the bulge and the upstream end of the sheet cavity, enabling the main flow to cut it and separate the cavitation area into two sections (figure 3.9c). The detached cloud is then pushed and rolled downstream under the combined actions of the main flow and the re-entrant jet.

During the up-lift stage, when the re-entrant is strong, multiple bulges can form, resulting eventually in several points of separation between these bulges at the next stage. In that case, several cavitation clouds are generated and detach almost simultaneously: this is the multi-clouds cavitation configuration shown in figure 3.9e. The raw image shows here three independent cavitation clouds, which are rotating counterclockwise. The Vx distribution also shows that the re-entrant jet is cut into

three sections. The evolution of this configuration is less predictable than the single cloud cavitation case: sometimes the clouds will move downstream individually and collapse separately, and sometimes they will merge together and be convected as a single cloud.

In the flow conditions indicated in Table 3.1, the flow sometimes oscillates between two configurations, typically between sheet cavitation and single cloud cavitation or between single and multiple cloud cavitation for larger cavities. The investigation of the 3D effects in the present study is performed in the specific case of single cloud cavitation, so we have selected acquisitions where this configuration is dominant.

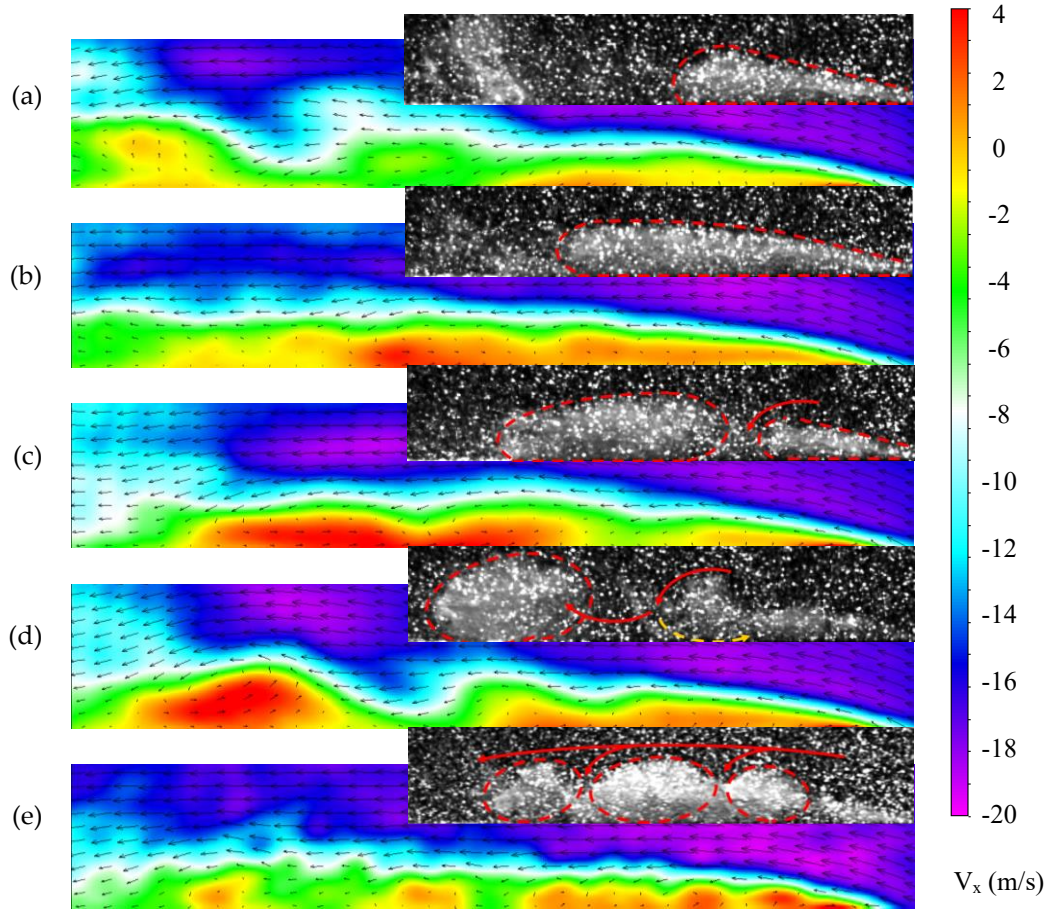

Figure 3.9. Raw images and instantaneous velocity component Vx (color field) superimposed with the velocity vectors for the 4 steps of single cloud cavitation (a) cavity growing, (b) cavity up-lift, (c) cavity break-off, (d) cloud convection. (e) Cavity break-off in case of multiple clouds

The examination of the z-component of the instantaneous velocity fields reveals a very complex fluctuating behavior, with characteristic frequencies close to the frequency of the cloud shedding (see figure 3.10). It suggests that the flow instability generates some significant perturbations in the z-direction, related to the cavity break-off and the rolling of the cloud of vapor, which is also certainly strongly coupled with the turbulence. The study of these effects is out of the scope of this work since the velocity fields were not acquired simultaneously in the 9 vertical planes, so the instantaneous 3D structure of the flow is not available. The study is thus intentionally focused on the large-scale dominant three-dimensional effects induced by cavitation, so only the time-averaged velocity fields will be used hereafter.

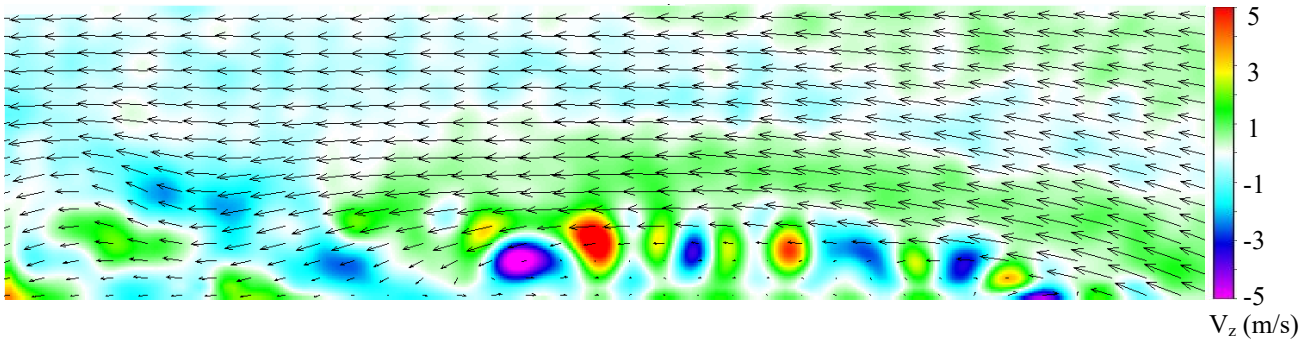

Figure 3.10. Instantaneous Vz distribution for test case #4 in the middle of the channel

3.2 Variation in the z direction

The flow in the venturi-type section is primarily two-dimensional. Figure 3.11 shows the time-averaged gray level brightness of the images of cavitation (left) in the nine vertical planes between the two sides of the test section (called hereafter P1 to P9), as well as the time-averaged vorticity distribution (middle). No significant variation according to z can be detected: only a decay of the general brightness with the distance to the observation window (from P9 to P1) can be observed, but no change in the vorticity is noticed.

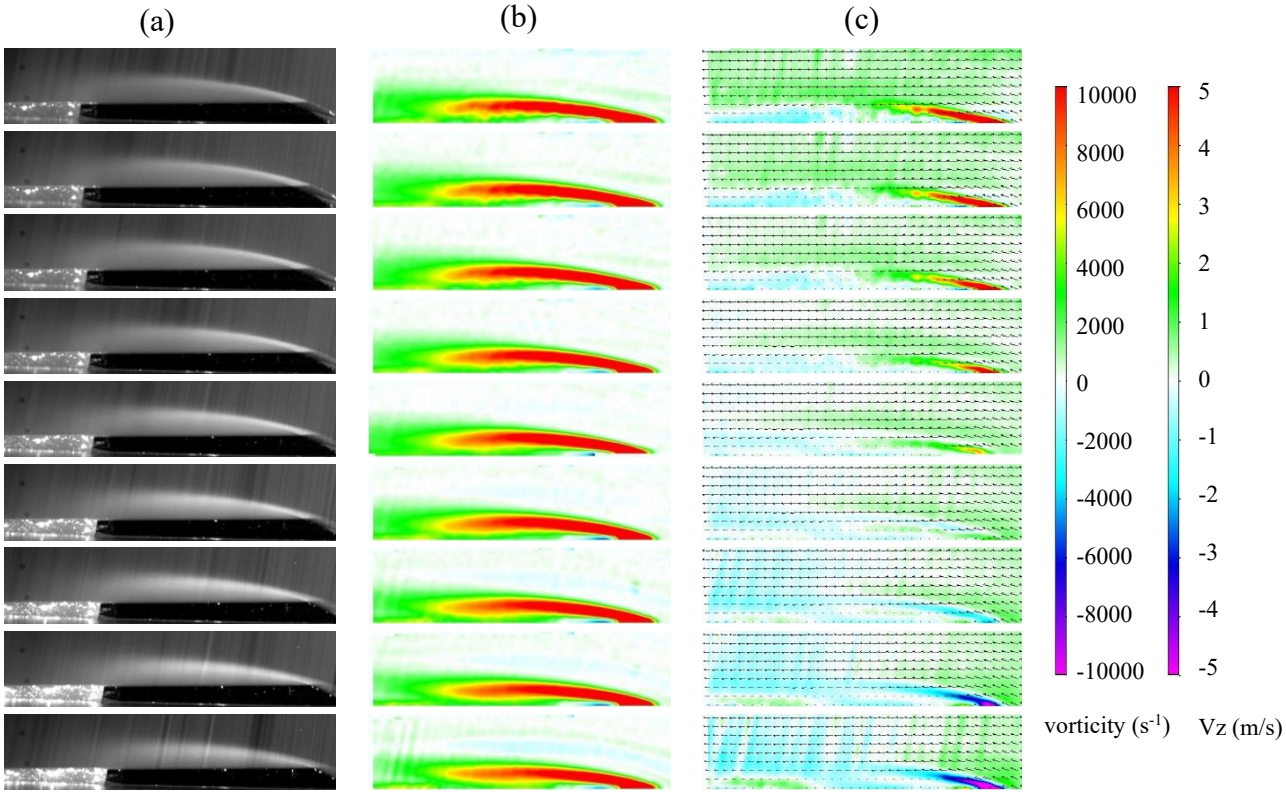

Figure 3.11. a) Time-averaged brightness of the raw images, b) Time-averaged vorticity field, c) Time-averaged Vz – Test case #4, positions 1 (back) to 9 (front) from top to bottom

This qualitative similarity is confirmed by the quantitative comparisons displayed in figures 3.12a, b, and c, regarding the maximum vorticity in the height of the channel from x = -5 mm to x = 25 mm, the maximum Vx component (i.e., the max speed of the re-entrant jet), and the minimum Vx (i.e., the max. speed of the main flow). A pretty close agreement between the 9 different planes is obtained for these three parameters, which means that the dynamics of the flow are very similar at all z positions.

However, the examination of the z component of the velocity also reveals some significant 3D effects: figure 3.11c shows that a significant Vz velocity affects the upstream part of the sheet cavity, with negative speeds in the front (positions P6 to P9) and positive speeds in the back (positions P1 to P5), meaning that the flow is moving from the sides to the center of the channel. This is confirmed by figure 3.12d, which shows the evolutions of the maximum V_z in the channel height from x = -5 mm to 25 mm. An intense side jet characterized by a maximum amplitude of 7 m/s on both sides is present at the upstream end of the cavity, before decreasing progressively more downstream.

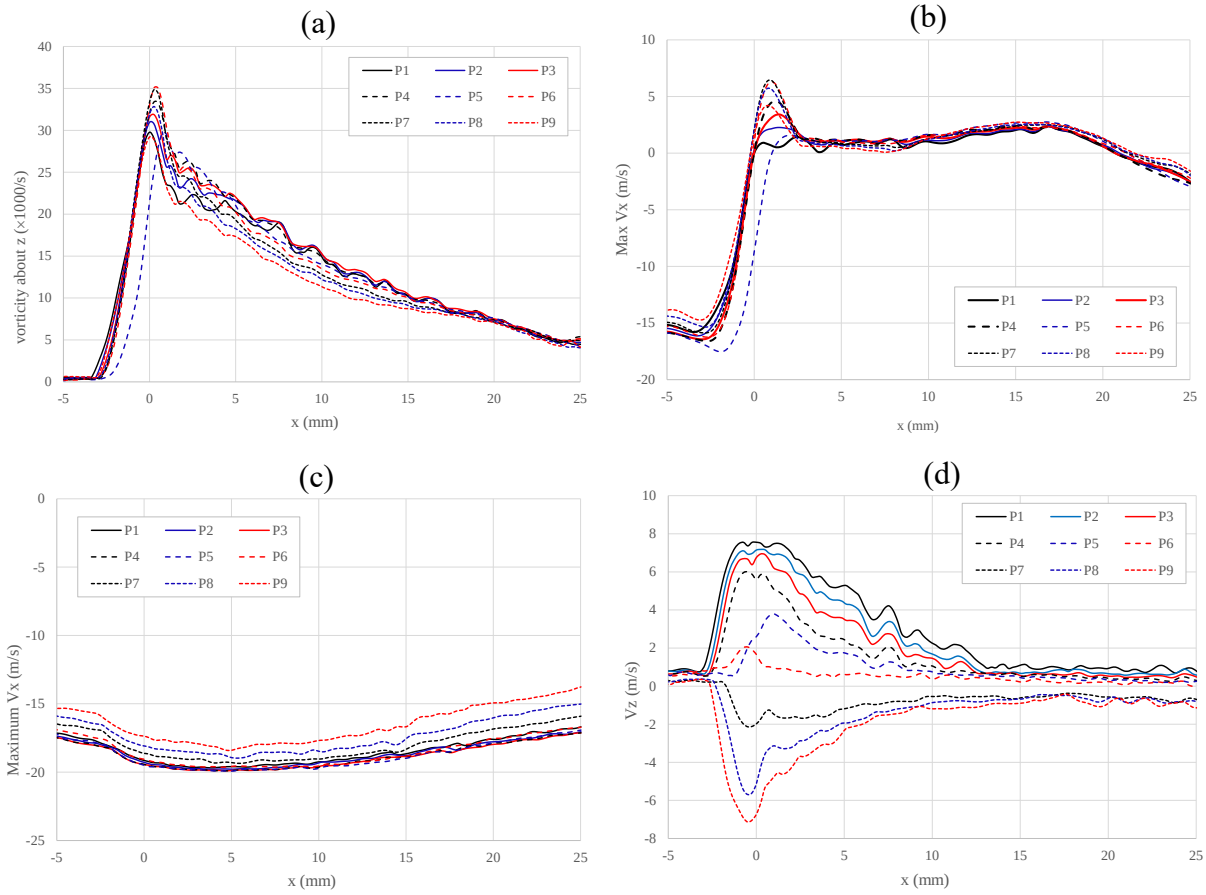

Figure 3.12. Evolution according to x of (a) the max. vorticity along the z axis, in the height of the channel, (b) the max. V_x component (re-entrant jet), (c) the maximum V_x component (maximum speed of the main flow), (d) the max. V_z component. The results are shown in the 9 vertical planes, from P1 (back side) to P9 (front side).

To get a better understanding of the flow structure in the z-direction, figure 3.13 displays for test cases 1 to 4 the z evolution of four quantities calculated in the nine vertical planes P1 to P9: the mean V_x, the mean V_z, the re-entrant jet max. speed, and the max. V_z magnitude. It shows that both the main flow and the re-entrant jet have a higher speed in the middle of the channel, compared to the sides: the variation is quite small for the main flow (of the order of 20% of the max. speed), but it is larger for the re-entrant jet (close to 50% of the max. speed). This is observed for the 4 flow conditions. Both the mean V_z and max. V_z evolutions confirm the presence of the jet towards the center of the test section, with intensity decreasing quite linearly from the sides to the center. Note that all results here show an asymmetry of the channel, as the zero mean V_z is obtained at position P7, the max. V_z is minimal at position P6, and the re-entrant jet max. speed is minimal at position P6

as well. Globally, the flow is quite symmetrical apart from position P6, while the center of the channel is at position P5. This might be related to a small imperfection at the junction between the side windows and the bottom wall, inducing a spurious side effect that slightly shifts the symmetry plane to the front.

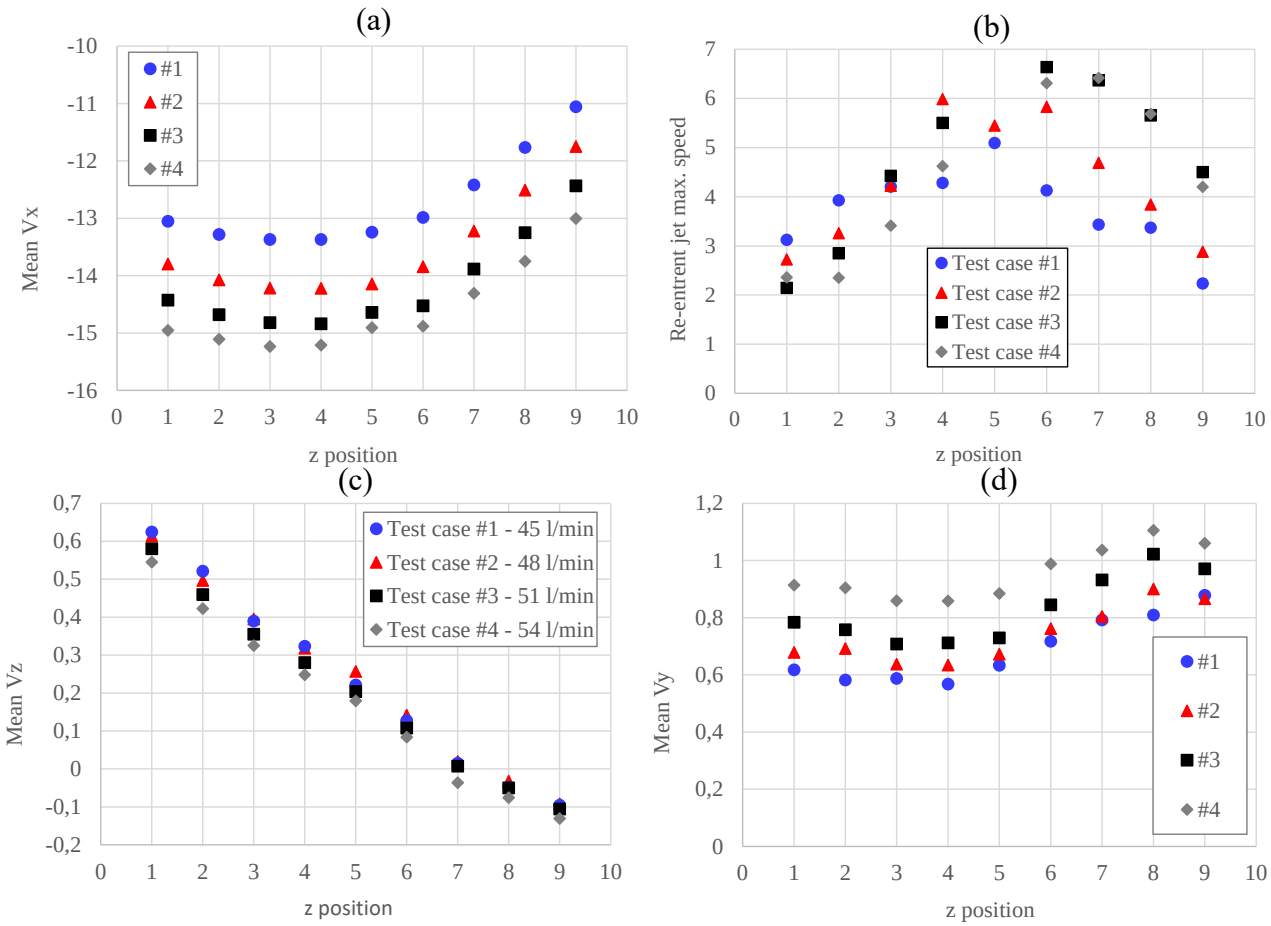

Figure 3.13. Evolution in the z direction of (a) the mean V_x in the x-y plane located at z, (b) the re-entrant jet max. speed in the x-y plane located at z, (c) The mean V_z in the x-y plane located at z, (d) the max. V_z in the x-y plane located at z

3.3 Three-dimensional structure

In order to better understand the 3D flow structure close to the bottom wall, in the re-entrant jet region, velocity vectors calculated in test case #4 are plotted in figure 3.14 in several x-z horizontal planes located at several heights above the Venturi surface, with the V_x velocity component as

background color field. The horizontal axis is the position in the x direction (remember the venturi throat is at x = 0), and the vertical axis is the position in the z direction from the backside (z = 0.5mm) to the front side (z = 4.5 mm).

The re-entrant jet (positive V_x values) is most intense immediately above the bottom wall (y = -2.1 mm) at two distinct x positions. The first one is just downstream of the throat (1 < x < 3 mm), where the jet reaches a maximum speed of approximately 7.5m/s (the empty area at the center of the channel is due to missing data close to the bottom wall, because of the mask used for PIV data processing). This high-speed reverse flow enables the sheet cavity to stay attached and grow, until the cloud eventually detaches. The second region of intense reverse flow is located between x = 10 and 17 mm, downstream from the break-off position, right below the detached cavity cloud. This second patch, where the maximum speed is approximately 3m/s, is related to the rolling of the cloud of vapor in the counterclockwise direction after it is shed.

At higher y positions, the intensity of the re-entrant jet decays rapidly, particularly in the area immediately downstream from the throat. At y = -1.4mm, the velocity of the entire re-entrant jet is close to zero, which means that the thickness of the re-entrant jet is approximately 0.7 mm at this flow condition. However, it must be reminded that all velocities here are time-averaged. The horizontal plane at y = -0.7 mm is characterized by alternate negative and positive velocities, depending on the steps of the periodical cycle of vapor shedding, which results in time-averaged speeds close to zero. So this region of the flow is still part of the re-entrant jet dynamics. At even higher y positions, the re-entrant jet is not present anymore at all, but the speed is still significantly lower than the one of the main flow. This one is recovered at approximately y = 1 mm (see figure 3.15).

The top part of figure 3.14 displays a vertical z-y plane located at x = 2 mm immediately downstream from the throat. The horizontal axis is the z direction from P1 to P9, and the vertical axis is the y direction. It shows that the entire re-entrant jet region represents only a small part of the venturi cross-section, but the dynamics in this small part trigger most of the properties of the sheet cavity.

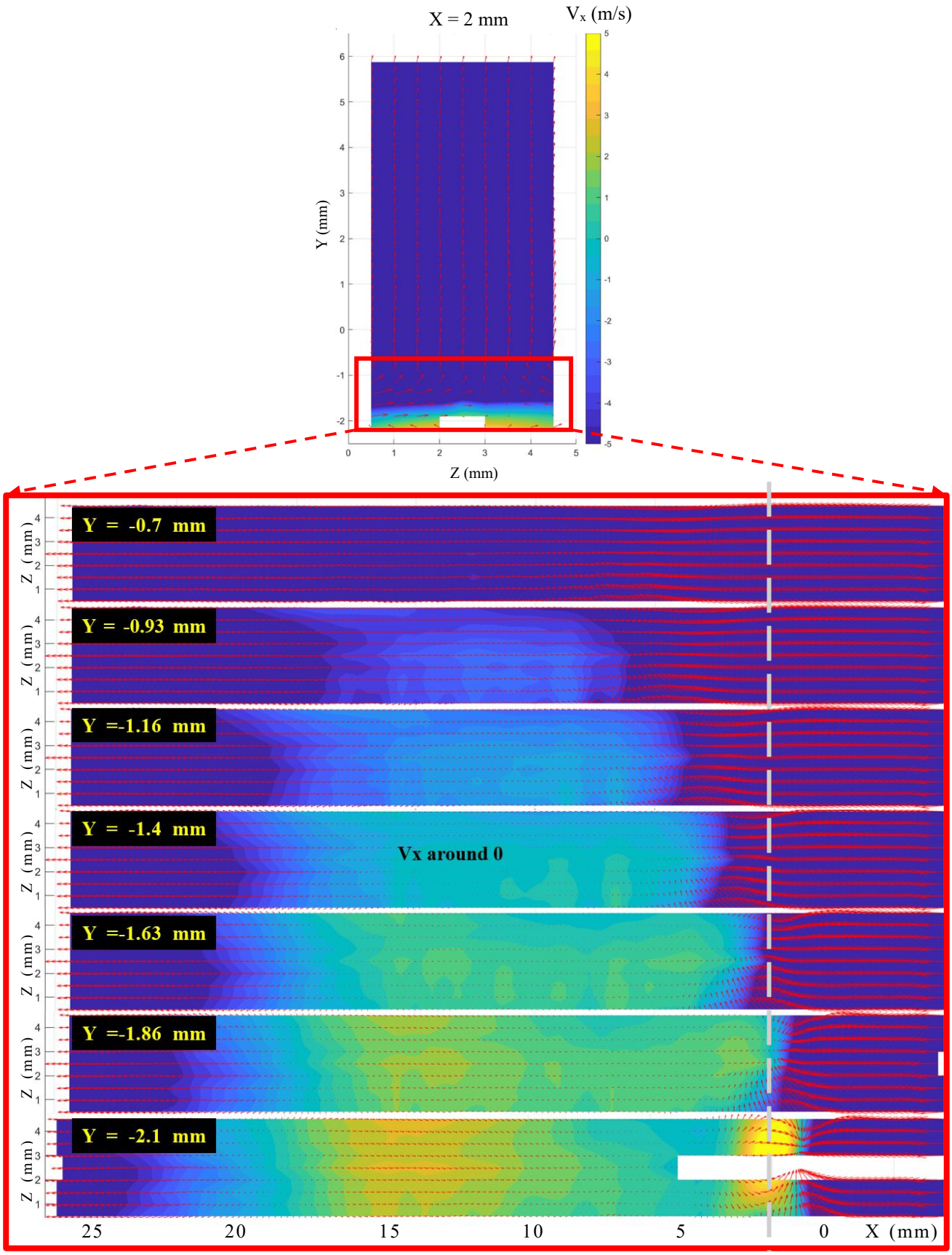

Figure 3.14. Bottom: time-averaged velocity vectors in x-z planes at different y positions within the re-entrant jet with Vx as background color field; Top: time-averaged velocity vectors in the z-y

plane located at x = 2 mm, with Vx as background color field (test case #4)

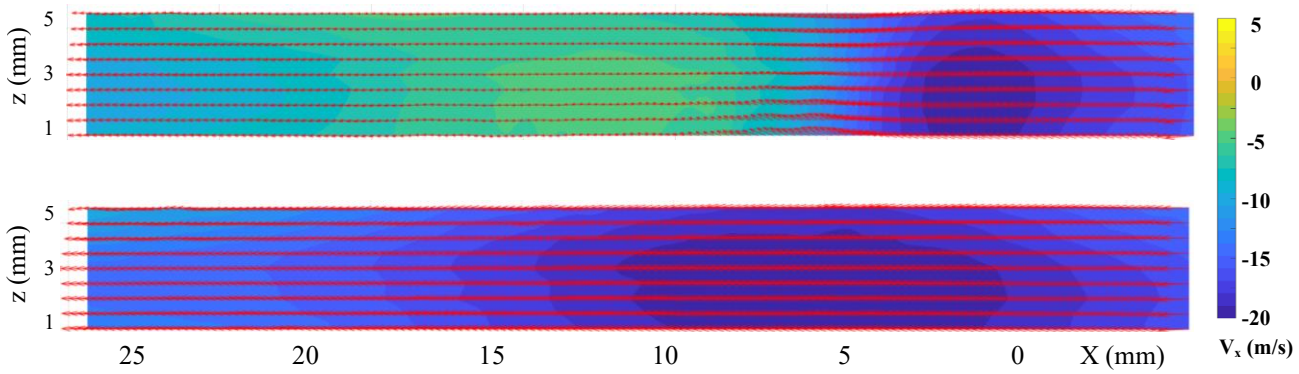

Figure 3.15. Time-averaged velocity vectors superimposed with Vx (color field) in the x-z plane located at y = -0.7 mm (top) and y = 1 mm (bottom) for test case #4

Details of the flow field immediately downstream from the throat (-3 < x < 5 mm) are displayed in figure 3.16. It shows that while it vaporizes, the flow is pinched to the center of the channel, and it also goes up to get around the sheet cavity. The speeds directed to the center are definitely larger at the back side, compared with the front, which results in a junction of the two side flows at z between 3 and 3.5 mm (between P6 and P7), as observed previously in the mean V_z evolution. Conversely, the re-entrant jet is more intense in the front, since the momentum is more directed to the x direction, instead of being partially moved to the side.

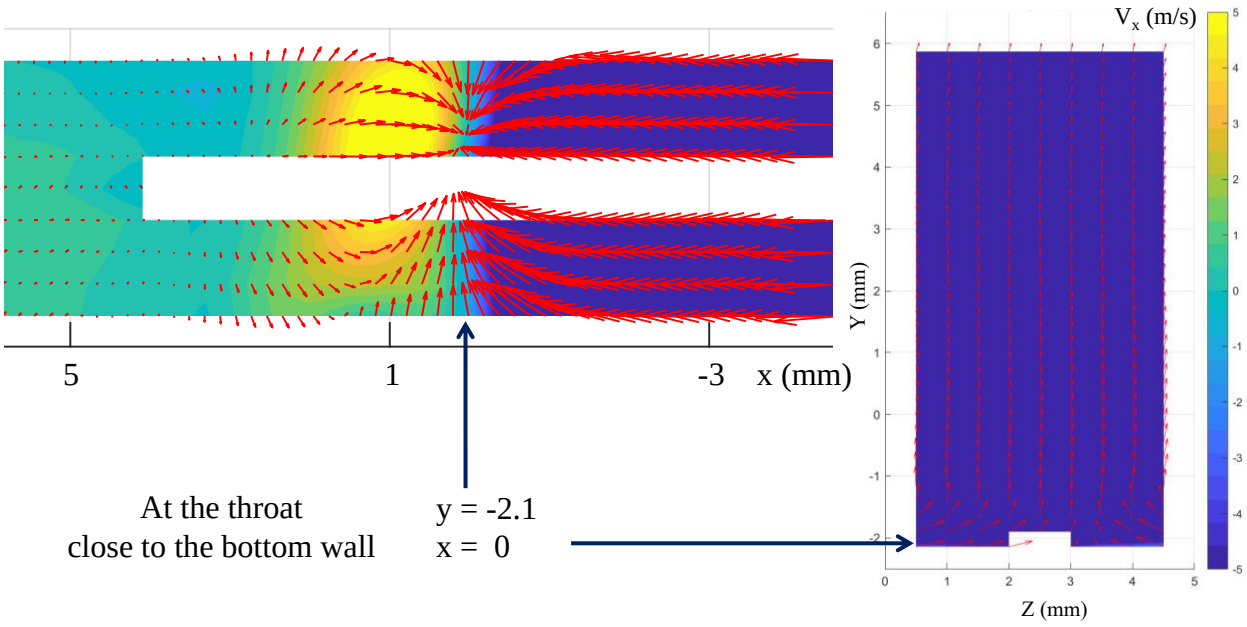

Figure 3.16. Zoom at the flow field close to the bottom wall, immediately downstream from the throat: velocity vectors and Vx (color field) in the x-z plane located at y = -2.1 mm (left) and in the y-z plane located at x = 0 (right) for test case #4

In figure 3.17, the velocity vectors are plotted in 5 different y-z planes located at distances from 0 to 10 mm from the Venturi's throat. It shows that the side jet is essentially located at the interface (yellow dashed line) between the attached sheet cavity and the mainstream region, slightly above the re-entrant jet. Therefore, the more we move downstream, the more the side jet is found at higher y positions. At the same time, a rapid decay of its intensity is observed.

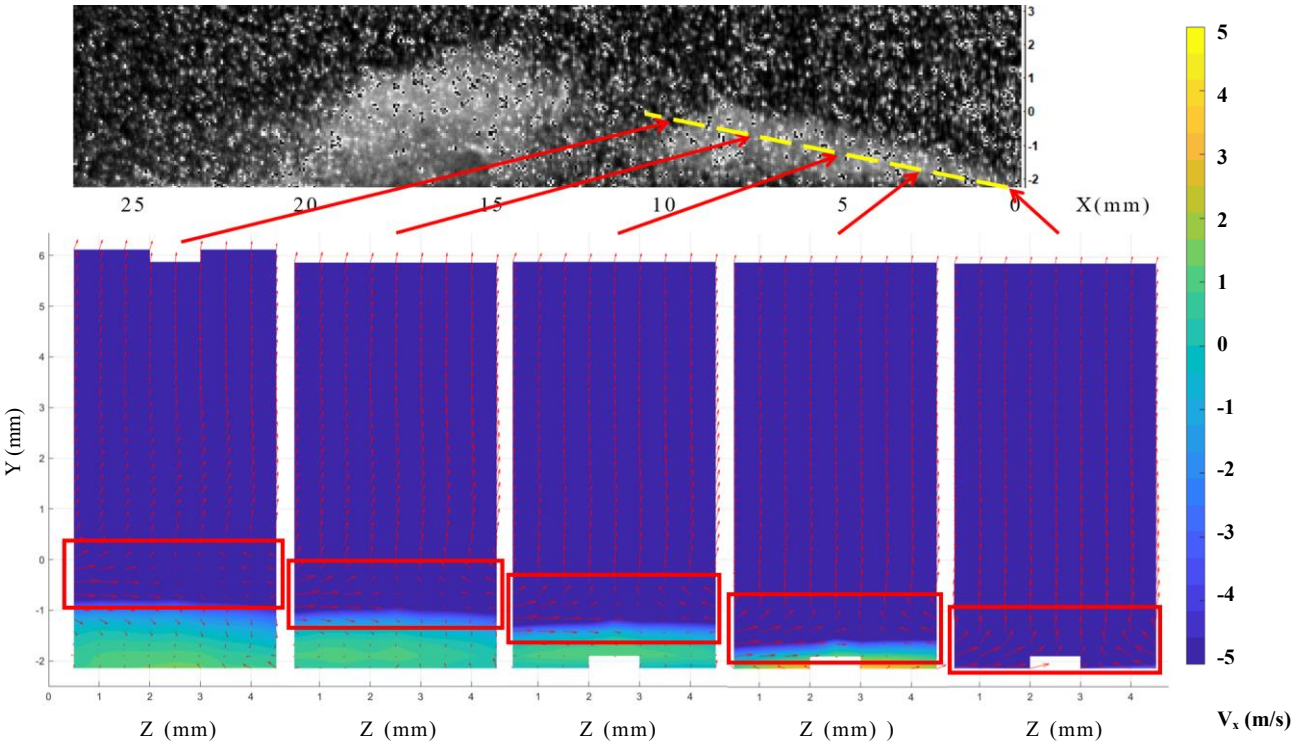

Figure 3.17. Time-averaged velocity vectors in y-z planes located at different x positions downstream from the throat with V_x as background color field (test case #4)

This side jet has not been detected in previous experiments or simulations[20, 28], possibly because the 3D simulations often assume periodical conditions at the side walls, rather than boundary layers that require a very costly mesh refinement. In the present experiments, it has not been found in non-cavitating flow conditions, while it starts to be observed when cavitation grows on the wall (sheet cavitation configurations). In cases of cloud cavitation studied here, the intensity of the side jet does

not vary significantly with the flow rate (and thus the size of the sheet cavity), as indicated in figure 3.18a. It leads to the preliminary conclusion that this phenomenon is directly related to the unsteady mechanisms of vapor shedding, through the re-entrant jet dynamics at the cavity leading edge.

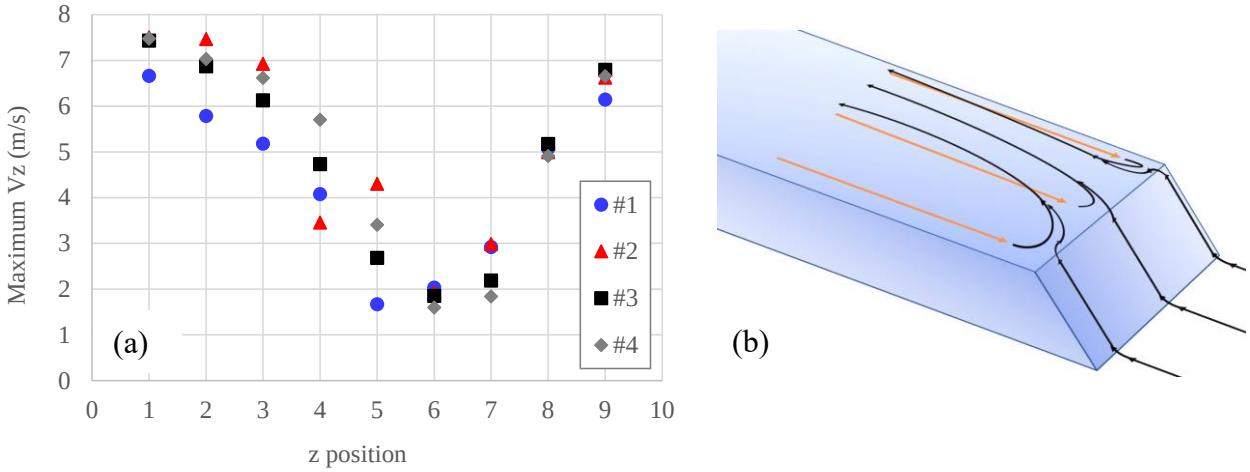

Figure 3.18. (a) Max. time-averaged velocities of the side-jet in planes P1 to P9, for the 4 test cases, (b) 3D schematic of the flow at the Venturi throat.

Based on this analysis, a three-dimensional schematic of the flow inside the attached sheet cavity, immediately downstream of the throat, is shown in figure 3.18b. The incoming flow at the throat, as it faces the re-entrant jet coming from downstream, is submitted to a side jet from the sides to the center, generated by the turn of the re-entrant jet, which still has some momentum. The flow is also lifted in the same process, thus accelerating the speed at the sheet cavity top interface. This effect of local flow acceleration at the top of the cavitation region has already been observed in previous experiments focused on the velocity fields in x-y planes3, 15, 27.

More downstream, in the area where the cavity break-off usually happens, the side jet, although it has lost some intensity, has also developed more in height: figure 3.19 shows that for x close to 12 mm (last y-z plane on the right), a large part of the y-z cross sections is submitted to a significant Vz velocity, still from the sides to the center. This velocity is directed partially downward into the re-entrant jet region, and partially upwards into the mainstream region. It also shows that the re-entrant jet intensity is quite low at this position (the max. Vx speed is around 1 m/s), which suggests that the side jet coming from above is significantly disturbing it, eventually leading to the cut of the sheet

cavity and its break-off, as described in section 3.1.

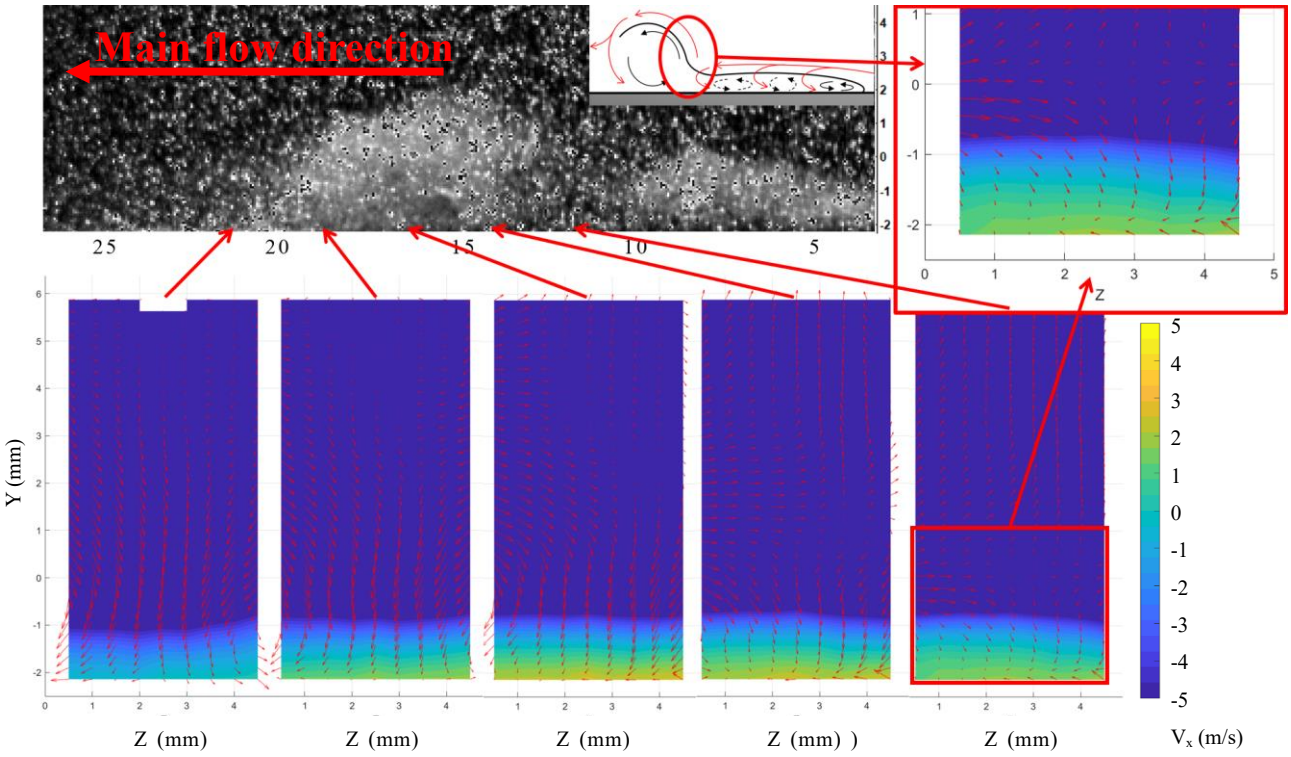

Figure 3.19. Time-averaged velocity vectors in y-z planes located at different x positions downstream from the cavity break-off location, with V_x as background color field (test case #4)

It was shown by Long et al.[16] that the cavity break-off is due to the formation of a bulge in the rear of the attached cavity, under the action of the re-entrant jet that lifts the bulge into the main flow region, causing the pressure to rise in front of it, resulting in cutting the connection between the bulge and the cavity sheet where the re-entrant jet is weaker. Eventually, this process initiates the cloud shedding. Thanks to the three-dimensional velocity field obtained here, this cut of the cavity can be visualized. The x position of the phenomenon varies in each test case, due to the different cavitation lengths, however, the flow field structure is generally the same, as shown in figure 3.20. It consists of a strong flow resulting from the side jet, flowing mostly downwards and also toward the center of the channel. This fluid impacts the re-entrant jet, and will divide into two streams, as will be seen later: one merging with the reverse flow in the attached cavity, the other one flowing underneath the detached cloud.

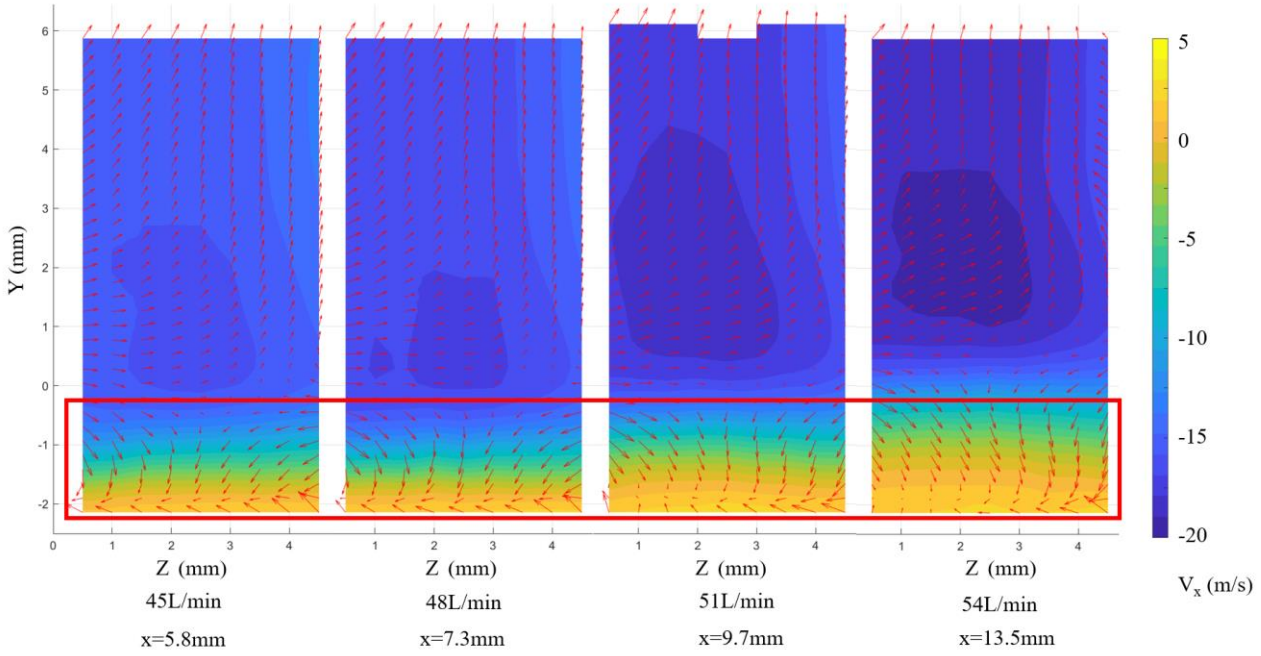

Figure 3.20. Time averaged velocity vectors and V_x color field in y-z planes located at the x position of the cavity break-off, for test cases 1 to 4 (left to right).

Further downstream, for x between 13 and 20 mm (see the 4 y-z planes on the left of figure 3.20), the situation becomes more complex, with a flow from the sides to the center and simultaneously to the bottom in the top part of the channel, and a flow from the center to the sides at the bottom. The more downstream we go, the more downwards the flow in the entire cross-section. This range of x positions in test case #4 is where the detached cloud of vapor is present, so this flow structure can be related to the spin of the cloud along the z-axis in the counter clock direction. In the rear part of the cloud, all velocities are from top to bottom, while at the front, a significant part above the re-entrant jet is going up.

Further downstream, once the re-entrant jet has vanished, a counter-clockwise vortex is visible in the lower right corner of the y-z cross-section, near the bottom wall and the side windows, as shown in figure 3.21 for the different test cases. For test case #4, this vortex is located at x = 27 to 29 mm, i.e., roughly at the location of the collapse of the cloud of vapor. It can be seen that a similar pattern tends to be created in the lower-left corner, so it can be assumed that if the channel was perfectly symmetrical, two identical vortices would be obtained, with a clockwise rotation in the left corner.

This secondary flow suggests that the cloud of vapor is characterized by a 3-dimensional rotation during its collapse, counter-clockwise in the x-y plane and both clockwise and counter-clockwise in the y-z plane, on the two sides. Figure 3.22 shows a schematic of the flow organization downstream from the cavity break-off (note that the orange arrow shows the re-entrant jet).

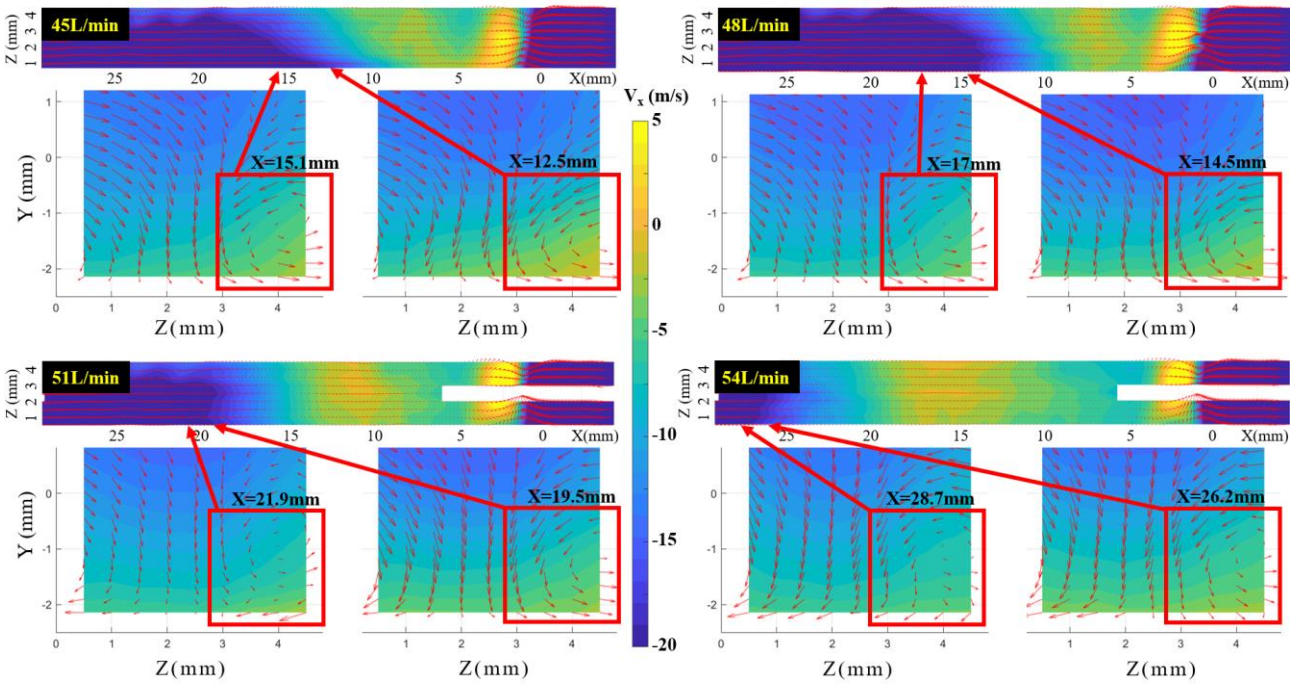

Figure 3.21. Time-averaged velocity vectors in y-z planes downstream from the cavity break-off, for the 4 test cases. The color field shows V_x.

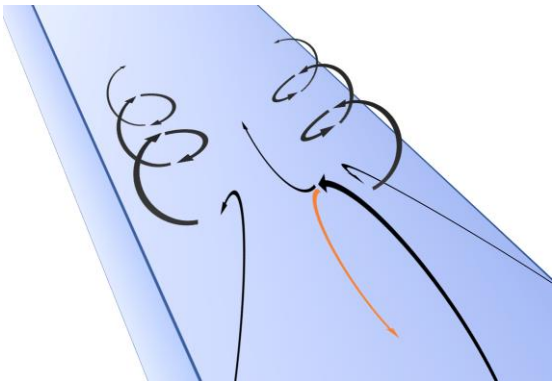

Figure 3.22. Schematic of the flow organization, downstream from the cavity break-off location

4. Discussion

In this section, our objective is to use the data presented hereabove to propose an explanation for the 3D features of the flow field, especially the inception of the side jet at the sheet cavity leading edge. As shown previously in figure 3.16, this jet starts to appear immediately downstream from the throat as the incoming flow interacts with the re-entrant jet. It develops at the interface between the main liquid flow area and the re-entrant jet (figure 3.23), which is an area of high velocity and pressure gradient, where intense vaporization is observed and confirmed by previous x-ray imaging in a similar flow configuration (figure 3.24).

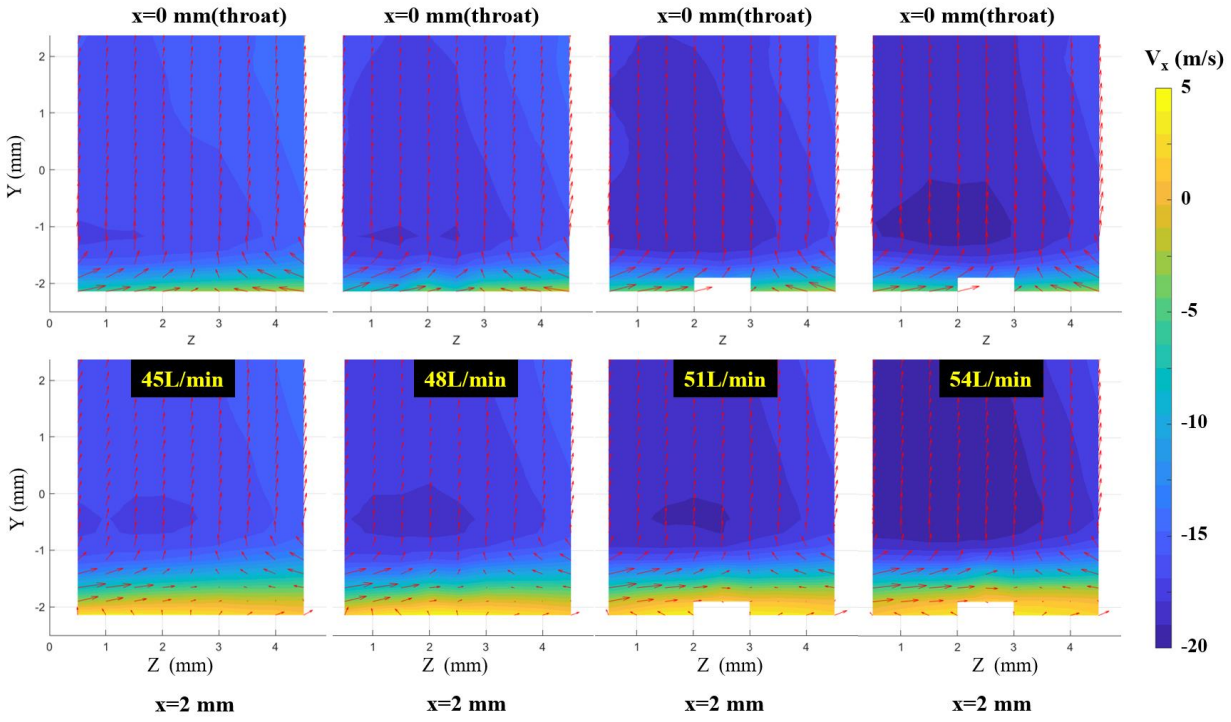

Figure 3.23. Side jet structure in y-z planes for different flow condition with Vx as background color

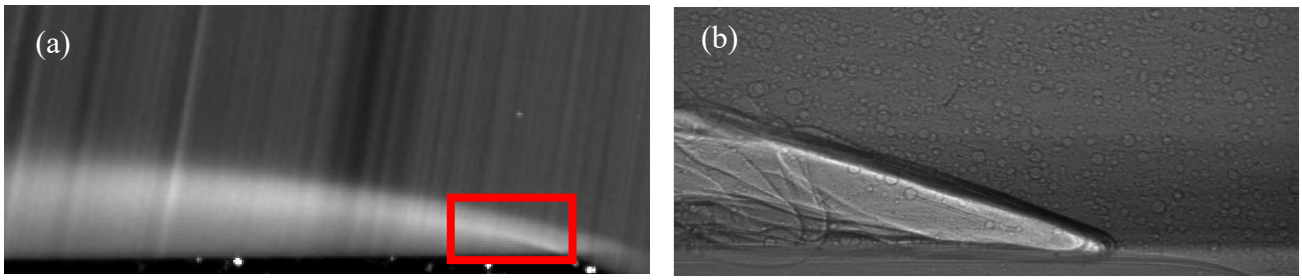

Figure 3.24. (a) Time-averaged brightness of raw images for test case #4 (position P9), (b) x-ray visualization of the intense vaporization at the cavity upstream end, in the same Venturi.

At the Venturi's throat, due to the 18° convergence angle and the 8° divergence angle, the incoming flow is deflected by an angle of 26°, so V_y decreases accordingly, and V_x also decreases due to the expansion of the Venturi flow channel (figure 3.25). However, the intense vaporization delays the velocity reduction caused by the expansion of the flow path. So, the combination of the cavity's fast expansion, the large V_x speed of the incoming flow, the significant momentum of the re-entrant jet, and the presence of the walls at the bottom and on the sides direct the flow up and to the center of the channel, generating a diagonal jet towards the interface. Downstream, as the vaporization rate is lower and the V_x speeds decrease, the strength of the side jet also decreases, as described in the previous section.

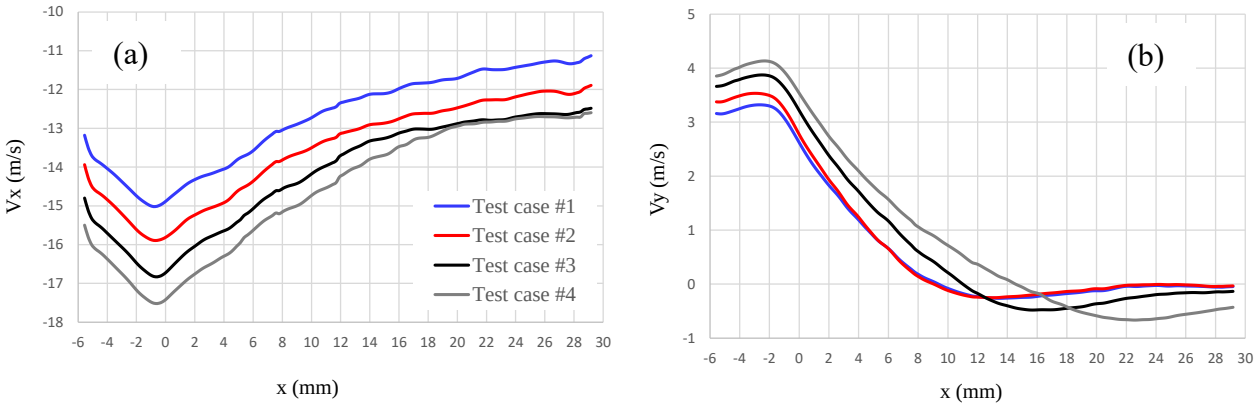

Figure 3.25. Time-averaged mean velocity (a) V_x in y-z vertical planes, according to x, (b) V_y in x-z horizontal planes, according to y

As mentioned previously, the flow field and the side jet are non-symmetrical. The effect is obtained in all test conditions for the 3 components of the velocity, and it is not related to any inaccuracy in the measurements. It was found that a small gap between one of the side windows and the bottom wall was responsible for this specific effect. Indeed, any side gap as small as 0.1 mm (while the test section is 5 mm wide) was found to generate a significant asymmetry, like the one observed in the present results. This is clearly a limitation in the use of a small-scale test section, although it must be mentioned that quite strong side effects, impacting sometimes the overall cavitation behavior, have been reported in the past also at a larger scale[29].

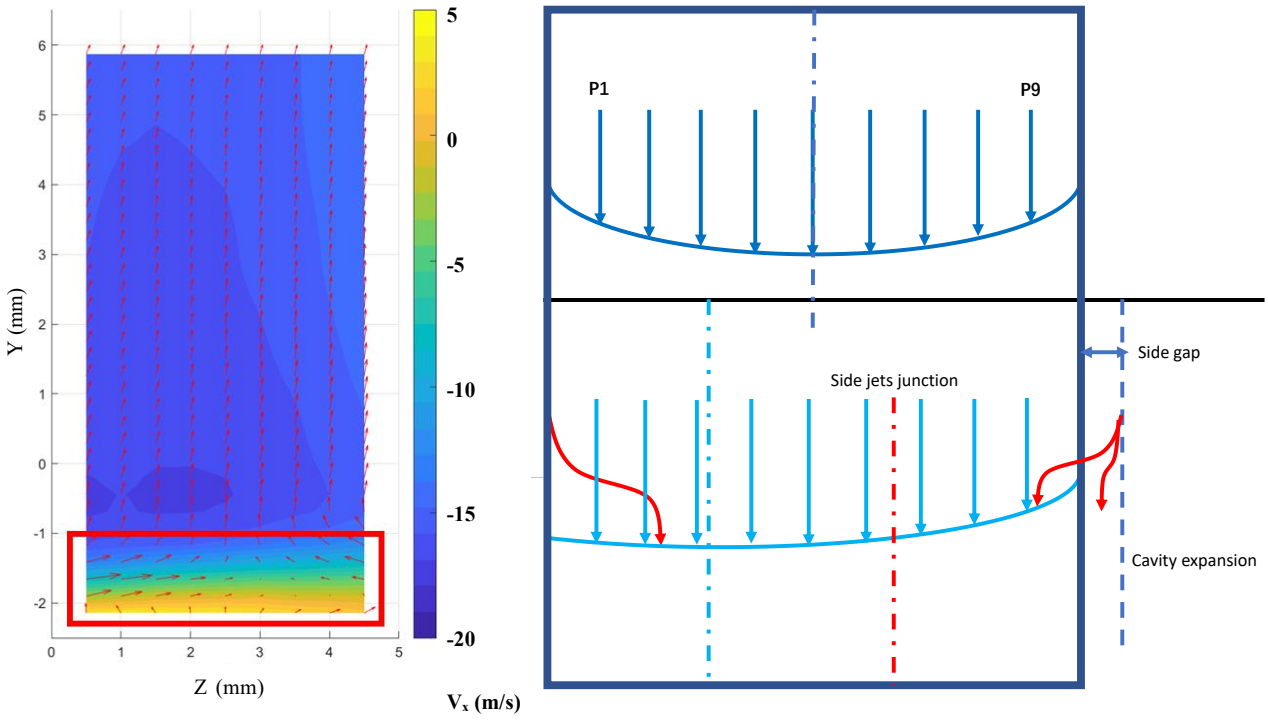

Figure 3.26. Schematic of side-gap and side-jet effects

Under normal conditions, if the incoming flow is uniform and stable, the flow field should be symmetrical, as shown in the upper part of figure 3.26, with two identical boundary layers on the sides and the side jet that would enhance the difference of speed between the center and the sides. However, it was shown in section 3 that the axis of symmetry of the V_x velocity component is between the P3 and P4 positions (see the mean V_x or V_y in figure 3.13). This asymmetry also impacts the side-jet intensity, which is higher on the P1 side and lower on the P9 side, but the axis of symmetry (where

V_z equals 0) is between P6 and P7 (figure 3.18). The same is observed for the re-entrant jet (see figure 3.13). This asymmetry can actually be used to confirm our hypothesis: the side where the re-entrant jet is the strongest is also the one that generates the most intense side flow.

5. Conclusion

In this paper, an analysis of the 3D flow structure inside the cavitation area generated on a 2D Venturi profile was studied using 2D3C PIV. The three components of the time-averaged velocity field were studied in various y-z planes from the leading edge to the downstream end of the sheet cavity, and in x-z planes located at various heights from the bottom surface to the junction to the pure liquid flow. A strong jet from the sides to the center, was detected in the area of intense vaporization just downstream from the Venturi's throat. This jet goes up towards the cavity top interface with the liquid main flow, contributing to the local acceleration detected in previous studies at the sheet cavity interface. It was shown that this jet resulted from the deviation of the incoming flow induced by the re-entrant jet, which is turning as it reaches the throat: the stronger the reverse flow, the larger the flow deviation to the center.

More downstream, this side jet goes down, due to the higher pressure generated at the front of the “bulge” induced by the lift of the rear part of the attached cavity (detailed by Long et al.[16]), eventually cutting the cavity at positions where the re-entrant jet is the weakest, and thus causing the cavity break-off and the detachment of a large-scale cloud of vapor.

Additional mechanisms were reported downstream of the cavity break-off, due to the rotation of the cloud of vapor in the counter-clockwise direction. Two vortices rotating along the x-axis were identified on the sides of the cloud, generating a complex three-dimensional structure. Overall, some significant three-dimensional mechanisms were detected, some of them directly contributing to the flow instability, although the flow configuration is purely 2D.

References

[1] Stutz B, Reboud J L. Experiments on unsteady cavitation[J]. Experiments in fluids, 1997, 22(3): 191-198.

[2] Callenaere M, Franc J P, Michel J M, et al. The cavitation instability induced by the development of a re-entrant jet[J]. Journal of Fluid Mechanics, 2001, 444: 223-256.

[3] Zhang G, Khlifa I, Fezzaa K, et al. Experimental investigation of internal two-phase flow structures and dynamics of quasi-stable sheet cavitation by fast synchrotron x-ray imaging[J]. Physics of Fluids, 2020, 32(11): 113310.

[4] Ganesh H, Mäkiharju S A, Ceccio S L. Bubbly shock propagation as a mechanism of shedding in separated cavitating flows[J]. Journal of Hydrodynamics, Ser. B, 2017, 29(6): 907-916.

[5] Podbevšek D, Petkovšek M, Ohl C D, et al. Kelvin-Helmholtz instability governs the cavitation cloud shedding in Venturi microchannel[J]. International Journal of Multiphase Flow, 2021, 142: 103700.

[6] Gopalan S, Katz J. Flow structure and modeling issues in the closure region of attached cavitation[J]. Physics of fluids, 2000, 12(4): 895-911.

[7] Arndt R E A, Song C C S, Kjeldsen M, et al. Instability of partial cavitation: a numerical/experimental approach[J]. 2000.

[8] Dular M, Bachert B, Stoffel B, et al. Relationship between cavitation structures and cavitation damage[J]. Wear, 2004, 257(11): 1176-1184.

[9] Foeth E J, Van Doorne C W H, Van Terwisga T, et al. Time resolved PIV and flow visualization of 3D sheet cavitation[J]. Experiments in Fluids, 2006, 40(4): 503-513.

[10] R. T. Knapp, J. W. Daily, and F. G. Hammitt, Cavitation (McGraw-Hill Book Company, London, 1970).

[11] Callenaere M, Franc J P, Michel J M, et al. The cavitation instability induced by the development of a re-entrant jet[J]. Journal of Fluid Mechanics, 2001, 444: 223-256.

[12] Stutz B, Reboud J L. Experiments on unsteady cavitation[J]. Experiments in fluids, 1997, 22(3): 191-198.

[13] Pham T M, Larrarte F, Fruman D H. Investigation of unsteady sheet cavitation and cloud cavitation mechanisms[J]. J. Fluids Eng. Jun 1999, 121(2): 289-296

[14] Dular M, Bachert R, Stoffel B, et al. Experimental evaluation of numerical simulation of cavitating flow around hydrofoil[J]. European Journal of Mechanics-B/Fluids, 2005, 24(4): 522-538.

[15] Khlifa I, Vabre A, Hočevar M, et al. Fast X-ray imaging of cavitating flows[J]. Experiments in fluids, 2017, 58(11): 1-22.

[16] K. LONG, Coutier-Delgosha O, et al. Analysis of the cavitation instabilities with time-resolved stereo and multiplane Particle Image Velocimetry [J]. Physics of Fluids, 2022, 34(12): 123323.

[17] Johnson V E. Theoretical and experimental investigation of supercavitating hydrofoils operating near the free water surface[M]. National Aeronautics and Space Administration, Scientific and Technical Information Office, 1961.

[18] Gnanaskandan A, Mahesh K. Large eddy simulation of the transition from sheet to cloud cavitation over a wedge[J]. International Journal of Multiphase Flow, 2016, 83: 86-102.

[19] Apte D, Ge M, Coutier-Delgosha O. Comparison of Reynolds shear stress methods for RANS turbulence modelling of a cloud cavitation in a venturi[C]//APS Division of Fluid Dynamics Meeting Abstracts. 2021: P28. 008.

[20] Decaix J, Goncalves E. Investigation of three-dimensional effects on a cavitating Venturi flow[J]. International Journal of Heat and Fluid Flow, 2013, 44: 576-595.

[21] Prothin S, Billard J Y, Djeridi H. Image processing using proper orthogonal and dynamic mode decompositions for the study of cavitation developing on a NACA0015 foil[J]. Experiments in fluids, 2016, 57(10): 1-25.

[22] Gopalan S, Katz J. Flow structure and modeling issues in the closure region of attached cavitation[J]. Physics of fluids, 2000, 12(4): 895-911.

[23] Kravtsova A Y, Markovich D M, Pervunin K S, et al. High-speed visualization and PIV measurements of cavitating flows around a semi-circular leading-edge flat plate and NACA0015 hydrofoil[J]. International Journal of Multiphase Flow, 2014, 60: 119-134.

[24] Dular M, Bachert R, Schaad C, et al. Investigation of a re-entrant jet reflection at an inclined cavity closure line[J]. European Journal of Mechanics-B/Fluids, 2007, 26(5): 688-705.

[25] Ge M, Zhang G, Petkovšek M, et al. Intensity and regimes changing of hydrodynamic cavitation considering temperature effects[J]. Journal of Cleaner Production, 2022, 338: 130470.

[26] Dular M, Khlifa I, Fuzier S, et al. Scale effect on unsteady cloud cavitation[J]. Experiments in fluids, 2012, 53(5): 1233-1250.

[27] Ge M, Zhang G, Nematikourabbasloo N, et al. Application of fast synchrotron X-ray imaging in velocimetry of cavitating flows[C]//SNAME 26th Offshore Symposium. OnePetro, 2021.

[28] Barre S, Rolland J, Boitel G, et al. Experiments and modeling of cavitating flows in venturi: attached sheet cavitation[J]. European Journal of Mechanics-B/Fluids, 2009, 28(3): 444-464.

[29] Gouin C, Junqueira-Junior C, Goncalves Da Silva E, et al. Numerical investigation of three-dimensional partial cavitation in a Venturi geometry[J]. Physics of Fluids, 2021, 33(6): 063312.

CHAPTER IV. CAVITATION DYNAMICS AT SUB-MILLIMETER SCALE

Kunpeng Long[1], *Olivier Coutier-Delgosha[1,3], Matevž Dular[2], Annie-Claude Bayeul-Lainé[1]

[1] *Univ. Lille, CNRS, ONERA, Arts et Metiers Institute of Technology, Centrale Lille, UMR 9014 - LMFL - Laboratoire de Mécanique des Fluides de Lille - Kampé de Fériet, F-59000 Lille, France*

[2]*University of Ljubljana, Slovenia*

[3]*Virginia Tech, Kevin T. Crofton Dept of Aerospace & Ocean Eng., Blacksburg VA 24060, USA*

Abstract

This paper focuses on cloud cavitation dynamics at Sub-millimeter scales, between 0.1mm and 10 mm. A simple flow configuration consisted of a small diameter jet flow impacting a wall at 90° from a plat jet nozzle and then flowing radially between two plates. Cavitation was obtained in the gap between the two plates due to the local flow acceleration. The setup scale was changed by varying the gap between the two plates and the nozzle diameter separately. Observations were performed from the transparent bottom plate, using a high-speed camera and intense illumination, for various Reynolds and cavitation numbers. The analysis focus on the variations of the cavity length and the Strouhal number based on the characteristic frequency of the flow instability for the first part of experiment. Later PIV tools was introduced to calculate the velocity field, and frequency map was also calculated, which makes the local parameters could be obtained quantitatively.

Keywords: Small Scale, cavitating flow, instability, flow imaging

* Corresponding author, ocoutier@vt.edu

Chapitre IV. Dynamique de la cavitation a l'echelle submillimetrique(Français)

Le chapitre 4 se concentre sur l'étude de la cavitation de nuages à l'échelle sub-millimétrique. Elle est obtenue par un jet impactant perpendiculairement une plaque inférieure, qui est ensuite accélérée en plaçant une plaque supérieure en parallèle. Dans un premier temps, la revue de la littérature porte sur la physique générale de la cavitation. Ensuite, une étude montre que des types de cavitation très différents sont observés si l'on considère différentes échelles de pales, pour un même nombre de cavitation.

Les expériences sont menées dans deux installations expérimentales différentes. Le dispositif expérimental est simple et bien présenté. Les deux installations ont la même configuration, mais avec des conditions de fonctionnement différentes. La visualisation est effectuée à l'aide de caméras à haute vitesse, jusqu'à 600K fps. De nombreuses conditions ont été étudiées en faisant varier le diamètre de la buse du jet et la distance entre les plaques. En raison de la cavitation à micro-échelle, aucune particule n'a été ajoutée pour les mesures de PIV et les vitesses sont mesurées directement à partir des bulles.

Les résultats sur la longueur de la cavité montrent une évolution cohérente du comportement de la cavitation avec le débit, de la cavitation ondulatoire, à la cavitation maillée et enfin à la cavitation nuageuse. La cavitation ondulatoire semble provenir d'un mécanisme d'instabilité.

L'auteur introduit ensuite une longueur non dimensionnelle pour caractériser les fréquences dominantes de l'écoulement. Des fréquences de Strouhal basses, moyennes et hautes sont identifiées, qui se comportent linéairement avec le débit

Résumé :

Cet article se concentre sur la dynamique de cavitation des nuages à des échelles submillimétriques, entre 0.1 mm et 10 mm . Une configuration d'écoulement simple consistait en un jet de petit diamètre impactant une paroi à 90° à partir d'une buse de jet plat et s'écoulant ensuite radialement entre deux plaques. La cavitation a été obtenue dans l'espace entre les deux plaques en raison de l'accélération locale de l'écoulement. L'échelle du montage a été modifiée en faisant varier

séparément l'espace entre les deux plaques et le diamètre de la buse. Les observations ont été réalisées à partir de la plaque inférieure transparente, à l'aide d'une caméra à grande vitesse et d'un éclairage intense, pour différents nombres de Reynolds et de cavitation. L'analyse s'est concentrée sur les variations de la longueur de la cavité et du nombre de Strouhal en fonction de la fréquence caractéristique de l'instabilité de l'écoulement pour la première partie de l'expérience. Plus tard, des outils de PIV ont été introduits pour calculer le champ de vitesse, et la carte de fréquence a également été calculée, ce qui permet d'obtenir les paramètres locaux de manière quantitative.

Conclusion :

Cet chapitre présente une étude approfondie de la cavitation des nuages à de petites échelles (submillimétriques) à travers plusieurs étapes d'expériences photographiques à grande vitesse de jets de plaques. Grâce à l'amélioration continue du système d'éclairage expérimental et du système d'acquisition, la résolution temporelle et spatiale de la photographie à grande vitesse du phénomène de cavitation a été améliorée de manière significative, et les différentes caractéristiques de la cavitation dans les jets de plaques à différentes échelles et à différents débits ont été observées. Le phénomène de cavitation est décrit de manière qualitative et la longueur de la cavité a été analysée de manière quantitative.

En outre, l'innovation de la méthode de post-traitement a permis d'améliorer la précision de la mesure de la fréquence et de la longueur de la cavité et de réduire l'erreur pour l'expérience de cavitation à petite échelle. La distribution radiale des fréquences de cavitation le long de la direction de l'écoulement est obtenue en sélectionnant différentes fenêtres d'observation ROI dans la direction radiale. On observe que les fréquences caractéristiques de la cavitation ne sont pas identiques et constantes sur l'ensemble de la région de cavitation mais présentent une distribution multi-ordre. Par la suite, à l'aide de la courbe d'équation d'ajustement, une carte de fréquence des divisions de fréquence dominantes de la cavitation du nuage de jet de plaque sur toute la zone d'observation expérimentale a été réalisée, donnant une compréhension intuitive globale des caractéristiques de fréquence de la cavitation du jet de plaque. La carte de fréquence est plus attrayante visuellement et fournit des informations plus générales sur le champ d'écoulement que la prise d'un certain nombre de ROIs dans la direction radiale. Cependant, elle prend plus de temps pour le post-traitement et

l'incertitude est plus importante en raison des algorithmes de traitement.

Une étude plus approfondie des FFT des images de cavitation dans une région particulière révèle que la fréquence ne change pas simplement en fonction de l'emplacement, mais que plusieurs fréquences se superposent dans toute la zone d'observation expérimentale. C'est seulement que les différentes régions présentent des fréquences dominantes différentes. En combinant la structure de la cavité observée par la photographie à grande vitesse, la théorie des ondes et des trous de la cavité est introduite. En séparant et en extrayant ces fréquences caractéristiques, l'analyse quantitative de certains groupes de résultats expérimentaux est effectuée, et des courbes de distribution des fréquences caractéristiques sont dérivées pour les trois fréquences globales les plus apparentes : les hautes, moyennes et basses fréquences. Cette méthode d'analyse des fréquences a permis de constater que la fréquence globale varie linéairement avec le débit. Les courbes de distribution du nombre de Str ont été calculées pour chacune des trois fréquences caractéristiques, et un modèle de distribution hautement linéaire a été trouvé. De plus, les nombres Str à basse fréquence sont stables dans un intervalle spécifique, approximativement 0,25 pour le groupe d'expériences à plus petite échelle avec un espace de 0,7 mm et 0,65 pour le groupe d'expériences à plus grande échelle avec un espace de 1 mm.

Le paramètre local était nécessaire en raison d'une variation de la fréquence de cavitation dominante en fonction de l'emplacement. Ainsi, un calcul de PIV a été effectué pour obtenir un champ de vitesse préliminaire en utilisant les bulles de cavitation du nuage auto-généré comme particules traceuses. En outre, une division préliminaire du facteur de vide local a été dérivée en calculant le champ de vitesse moyen par rapport à la structure géométrique. En comparant le champ de vitesse avec la carte de fréquence, une forte corrélation et une distribution cohérente ont été trouvées entre eux. Le nombre Str local a été calculé en utilisant ce champ de vitesse, combiné avec la fréquence locale obtenue par la méthode précédente. La distribution du nombre Str local en fonction de la distance du trou a été tracée et s'est avérée être une courbe approximative cohérente pour différents débits, avec seulement une forte corrélation avec la géométrie. Cependant, en raison de la précision des mesures, l'analyse quantitative n'est pas discutée plus avant dans cet article mais peut être améliorée et étudiée dans de futures expériences.

1. Introduction

Hydrodynamic cavitation is a phenomenon that specifically happens in liquid flows. It is a liquid vaporization phenomenon that occurs in the case of high-speed flows due to the pressure decrease associated with the local flow acceleration. In most engineering applications, cavitation has adverse effects such as performance decrease, noise, vibrations, and erosion, which are extremely difficult to prevent. On the other hand, cavitation is also used as a positive phenomenon, for example, for medical or chemical applications[1-4]. In this thesis, the main research topic is conventional cavitation, also known as "Hydraulic Cavitation" or "Hydrodynamic Cavitation."

Pieces of evidence of cavitation have been reported for quite a long time, but scientific study Only started in the late 1890s. In 1895, English scientist Parsons built an experiment setup to observe the phenomenon of cavitation in the laboratory. This was the first cavitation water tunnel experiment setup in the history of science. In 1897, during the cooperation with Parsons in studying the topic of "ship propeller efficiency decrease," English scientist Barnaby named this kind of hydrodynamic phenomenon "cavitation " by reference to the analysis of propeller air-suction by Reynolds in 1873 and the word "cavitation " mentioned in the research of Froude in 1887[3].

In 1924, American scientist Thomas suggested using a non-dimensional number to describe the state of cavitation in liquid. This non-dimensional number was also defined as the cavitation number(σ) during the development of cavitation research[5]. This number provided a quantitative characterization of cavitation and thus facilitated the experimental tests and comparisons between different flow conditions. In this thesis, we use mainly the two non-dimensional numbers to describe different cavitation phenomena: the Strouhal number (Str, non-dimensional frequency), which characterized the flow instabilities, and the cavitation number(σ).

Cavitation phenomena are observed in high-speed liquid flow and on the surfaces of objects with a high relative velocity with surrounding fluid[6]. Cavitation is usually unsteady with oscillations in the range of 50 Hz to 500 Hz[7], so it is complicated to observe with naked eyes. High-speed photography is therefore used to study cavitation phenomena. In addition, it can also be characterized by the analysis of the noise it produces or the erosion of the solid surfaces submitted to cavitation[8]

According to the different flow conditions, cavitation conditions are classified into different forms: traveling cavitation, Sheet Cavitation, Cloud Cavitation, Super cavitation, Vortex cavitation, and Vortex cavitation behind the bluff body, etc.[1, 3]. The primary study object in this paper is cloud cavitation.

In the 21st century, with the development of science and technology, underwater machines and equipment show a downsizing trend. Such as mini submarines or diving robots, which are widely used in marine scientific investigations, deep ocean adventures, wreck salvages, and underwear rescues. Besides, there is also some newly developing industry that requires small scale underwater machines such as pipeline maintenance, urban underground engineering, especially in the field of medical treatment: the application or micro medical robots provide a brand-new solution for surgeons to operate on their patients, which is more secure, more efficient, more accurate, and minimally invasive. It has been found out that a problem is always there, which leads to efficiency loss, construction damage, service life loss, and noise, the Cavitation[3, 8].

However, cavitation on the micro-scale is quite different from what happens on a large scale, not only in external physical characteristics but also in frequency and other mechanisms[9, 10]. The following pictures are cavitation phenomena in different scales of a NACA 16020 hydrofoil by Keller and Andreas Peter in 2001[11].

(a) Max. chord length 50 mm
$\boldsymbol{\sigma} = 2.18 \quad \mathbf{u}_{\infty} = 11{,}0$ m/s
Beginning tip vortex cavitation

(b) Max. chord length 100 mm
$\boldsymbol{\sigma} = 2.18 \quad \mathbf{u}_{\infty} = 11{,}0$ m/s
Developed cavitation

(c) Max. chord length 200 mm
$\boldsymbol{\sigma} = 2.18 \quad \mathbf{u}_{\infty} = 11{,}0$ m/s
Fully developed cavitation

Figure 4.1. Size scale effect for cavitation shown with the example of a NACA 16020 hydrofoil

According to the difference compared to large scale, it was called “Small Scale Cavitation.”

Which been believed, with the development and popularization of micro machines, it is of great importance to study the mechanism of small-scale cavitation.

To study cavitation numerical computation is a practical and effective approach, but it still has its limitation due to current technology and theoretical achievement[1]. Rayleigh-Plesset(R-P) equation is the basic equation for babble dynamics[12]. However, after years' development, no matter how exquisite the computation became, no matter how the algorithm improved, it is still a single babble, cannot be generalized to common cavitation phenomena case. Despite the rapid development of CFD application in cavitation developing simulation, scientists still face many challenges. Cavitation is a kind of multiphase flow so that in numerical computation, not only turbulence flow but also the changing process between two phases should be considered and calculated. It is the main technical difficulty demanding a prompt solution. The several cavitation models in hand nowadays make some achievement in applying some critical parameters of some cases. However, they are without universality, especially in the description of details[13, 14].

Therefore, it is still a long journey for numerical researchers, making the experimental method still the most efficient approach to study Cavitation dynamics in such complicated flow conditions.

2. Experimental set-up

It is known that cavitation on a small scale behaves quite differently from what on a large scale; besides, many characteristics of cavitation such as cavitation number and Str number are also quite different. Thus, to uncover the mystery of what happens in small-scale cavitation and find out the mechanism of small-scale cavitation to compare the difference with what in large-scale cavitation, researchers have conducted a series of experiments on scale effects. As professor Olivier Coutier-Delgosha and professor Dular Matevž developed a Venturi nozzles scale effects cavitation experiment in Various geometries with high-speed cameras[7].

This research is based on what they have done before, expecting to get higher resolution images in much smaller scales and more couples of contrast experiments containing wilder flow conditions,

further, to get some more reliable results to assistant researchers to explore cavitation mechanism at the sub-millimeter scale.

2.1 Cavitation tunnels

Cavitation tests were conducted in a cavitation tunnel of the University of Ljubljana and Arts et Metiers ParisTech Lille. Experiments on smaller scales (1mm 3mm hole) were conducted in the small cavitation tunnel of the LML Laboratory (Lille, France), as shown in figure 4.2. Water circulation is obtained with a Salmson Multi HE 403 pump (2) that enables the variation of the rotation speed. At the pump delivery, a tank completely filled with the circulation water (3,10) is used for water cooling to maintain a constant temperature. Water temperature can also be increased with an immersion heater TCV020 of output 2,000 W (4). The volume flow rate is measured by two flow meters, depending on the flow rate – a turbine flow meter Bürkert type 8032 (DN 6, uncertainty 0.15 l/min after in situ calibrations) was used for low flow rates. Bürkert type 8045 (DN 15, 2 % uncertainty) flow meter was used for higher flow rates (5). Temperature is obtained with a type K thermocouple directly in contact with the circulation water. Upstream from the test section (7), a second tank (6) partially filled with water is used to filter the flow rate and/or periodical pressure fluctuations due to the passage of the pump blades. The reference pressure is measured 30 mm upstream from the test section with a Rosemount 3051 pressure sensor. The uncertainty of the measurements is as close to 10 mbar. The pressure in the test rig is adjusted in the partially filled tank (1) connected to a compressor and a vacuum pump (9), enabling the pressure in this tank to vary between 0.1 bar and 3.5 bar.

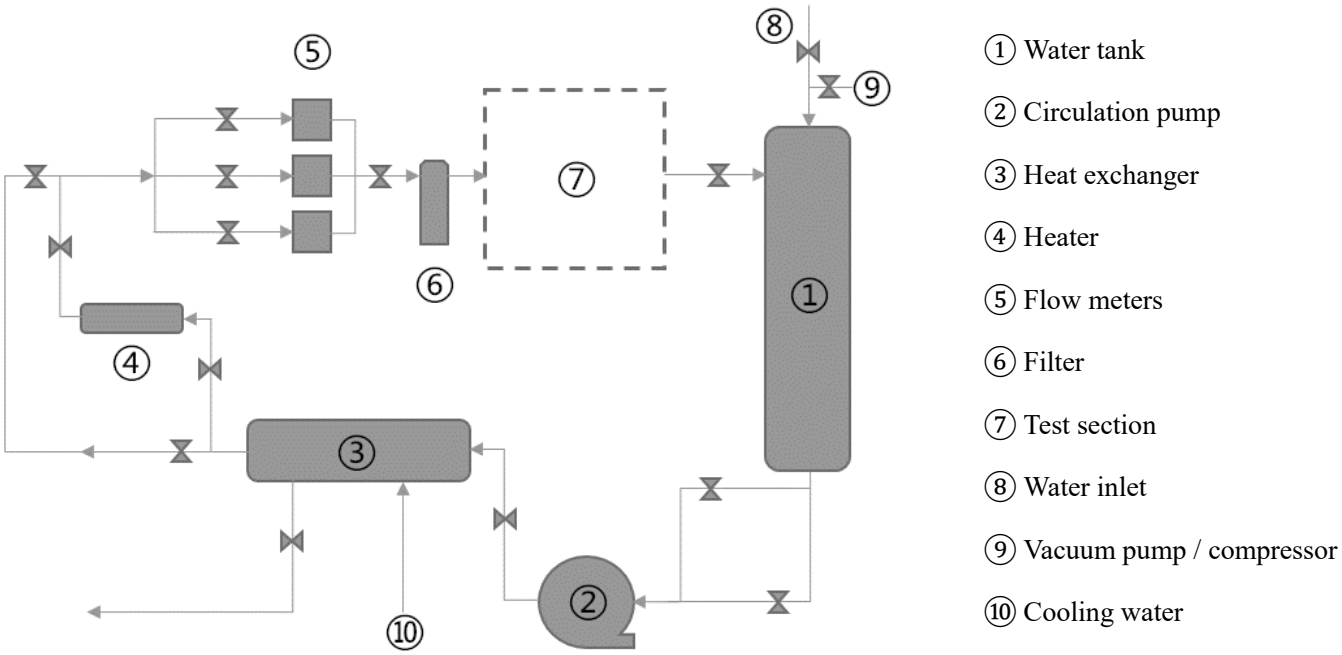

Figure 4.2. Cavitation tunnel at Arts et Metiers ParisTech

The cavitation tunnel at the University of Ljubljana is similar to the Cavitation tunnel at Lille, which is driven by a 4.5 kW pump, which enables the variation of the rotation frequency in order to set the flow rate. Downstream of the pump, a partially filled tank is installed to attenuate the periodical flow rate and pressure fluctuations. Cavitation and its effects are observed in a test Section. The water enters the section axially through the nozzle and exits by eight flexible pipes. The tank further downstream is used for cooling of the circulation and further attenuation of pressure and flow rate fluctuations. The valves enable easy and fast disconnection of the test section from the main loop. The flow rate is measured by an electromagnetic flow meter ABB ProcessMaster 300 (DN 40) with a 2% uncertainty on measurements. Temperature is obtained with a type K thermocouple. The reference pressure is measured 35 mm upstream from the test section by an ABB 266AST pressure transducer – the uncertainty of the measurements is 8 mbar. The pressure in the test rig is adjusted in the partially filled tank connected to a compressor and a vacuum pump. The pressure, velocity, and temperature measurements precisions result in a mean uncertainty of 3% for the cavitation number.

2.2 Test section

Cavitation is obtained with a radial jet impacting a flat plate, as shown in figure 4.3. The flow enters the test section at high velocity through a nozzle with a diameter D drilled in the upper plate. After it impacts the bottom plate, it then forced to turn at an angle of 90°, a radial outward cavitating flow between the bottom and upper plates is obtained. The gap between the two plates is denoted H. Cavitation is initiated slightly downstream from the edge of the inlet nozzle, and it collapses abruptly as the fluid moves radially outwards since the pressure re-increases in the radial direction.

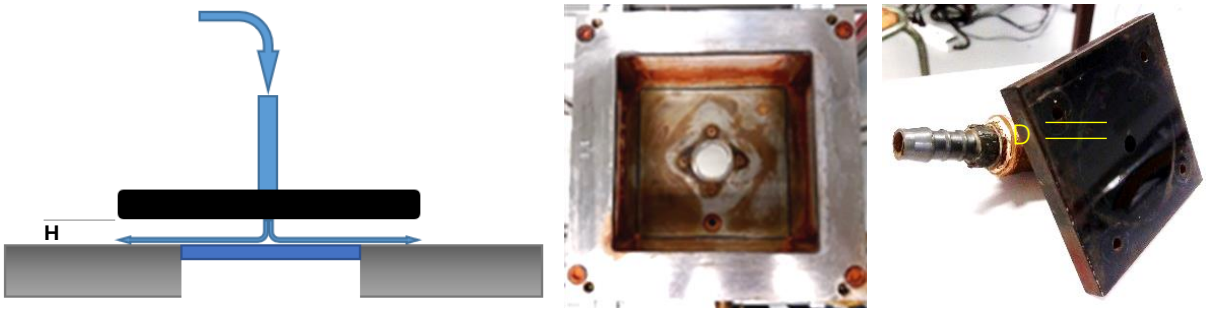

(a) (b) (c)

Figure 4.3. Plate jet test section (a) scheme of the flow passage side view, (b) Top view of the bottom plate, (c) upper plate

In Ljubljana, a more Compact test section was used, as shown in figure 4.4. The flow enters the section axially at a high velocity through a nozzle with a diameter of D. It is then forced to turn at an angle of 90°, making it cavitated. The radius of curvature of the feed nozzle exit is close to 0. The gap between the front and back plates is denoted by H. As the fluid moves radially outwards between the plates, the pressure recuperates rapidly, and the cavitation zone abruptly closes. The flow exits the section axially through 4 holes in the corner's backplate. This compact test section allowed us to have more space for lighting system and Acquisition devices operations.

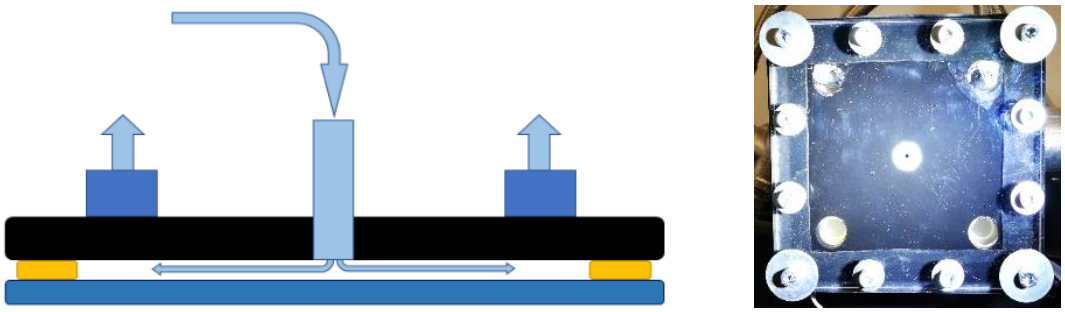

Figure 4.4. Test section (a) scheme of the flow passage side view, (b) bottom view of the test section

2.3 High speed visualization

In Lille, A MotionBLITZ EoSens mini1 high-speed camera is used for flow visualization from the bottom of the test section. Figure 4.5a presents the typical cavitation pattern obtained between the two plates. The camera's maximum resolution is 1280×1024 pixels at 2000 fps, while it was used for the present tests at a higher frequency of 20K to 50K fps (depending on the frequency of cloud cavitation) with a typical resolution of 512×100 pixels. For that purpose, only a tiny band of cavitation was recorded at high frequency instead of the whole axisymmetric cavitation pattern (see figure 4.5b). In the second campaign, an optimization of the image quality was conducted by testing three optics (Nikon AF Nikkor 50mm, Nikon AF-S DX Nikkor 40mm, and Nikon micro Nikkor 105mm) combined extension rings and various continuous illumination sources. As a result, the image's contrast and resolution could be significantly improved for all data sets #2 (figure 4.5c).

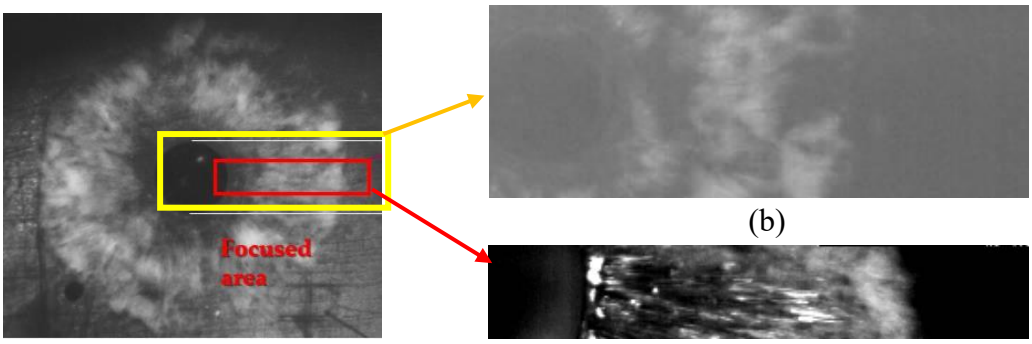

(a) (b) (c)

Figure 4.5. Cavitation raw images (a) whole pattern (b) zoom for high frequency acquisitions in data sets #1 (c) zoom in data sets #2

In Ljubljana, thanks to the use of the compact experimental section have given us more operation space, a completely new acquisition system (new high-speed camera FASTCAM SA-Z) was used to take higher resolution images in even much higher frequencies.

The maximum resolution of the camera is 1024×1000 pixels at 21,000 fps, while in this experiment, as it was not necessary to capture the entire cavitation area, thus the resolution was downscaled to focus on a certain part, allowing sampling frequencies of up to 300K to 600K fps in good quality. Besides, a lens extension tube was also used to increase the magnification ratio. As shown in figure 4.6, it is clear that the increase in acquisition frequency has led to an increase in the resolution of high-speed photography. Which even makes it possible to observe the re-entrant jet (second layer flow).

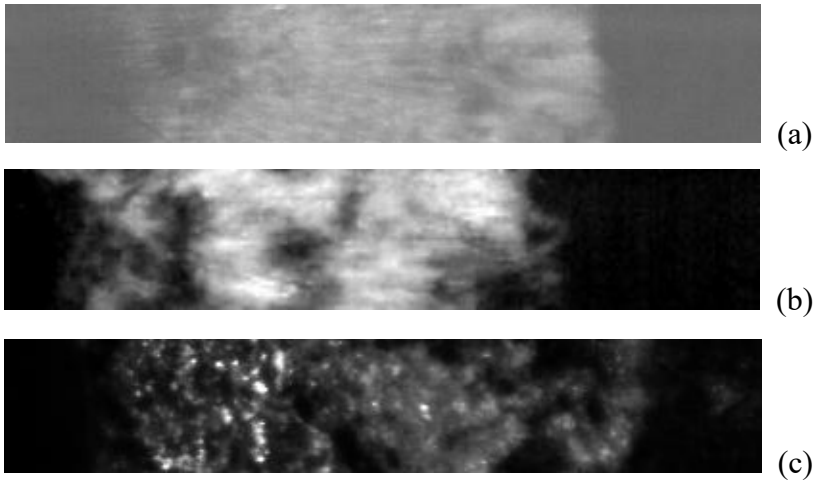

Figure 4.6. cavitation images at different resolution and acquisition frequencies (a) data sets #1, 16k fps, (b) data sets #2, 24k fps, (c) data sets #3, 315k fps

2.4 Investigated conditions

A total of 13 geometrical configurations have been investigated, with a nozzle diameter varying between 1 and 10 mm and various gaps between the two plates, as indicated in table 4.1. Note that two experimental campaigns were performed. In data set#1 (cases A to F in table 4.1), a D = 3 mm diameter hole was mainly considered, with H varying between 0.1 mm and 1 mm. Two additional

configurations with a larger 10 mm hole diameter (H = 3 mm) and a smaller 1 mm diameter (H = 0.33 mm) were also studied to investigate the effect of the hole size. An abrupt change of cavitation behavior was detected between H = 0.3 mm and H = 0.7 mm during the first stage of the experiment, so a second experimental campaign was set up to investigate the transition between these two behaviors. In this second set of experiments (cases G to M in table 4.1), holes of 3 mm and 6 mm diameter have been considered for various values of H between 0.3 and 0.9 mm. Due to the discrepancy between the results of Experiment 2 and Experiment 1 phases in Section 3, a third phase of the experiment was conducted concentrating mainly on the effect of the gap, with a new, improved lighting system and Acquisition devices. In this third set of experiments (cases N to Q in table 4.1), a constant 3mm diameter hole was used, with gap variations between 0.4mm to 1.63 mm.

Geometry	*D* *mm*	*H* *mm*	*D/H*	*Flow rate range* *L/min*	*Data Set*
A	***1***	***0.33***	***3.0***	***0.55 – 0.86***	***1***
B	***3***	***0.1***	***30.0***	***0.5 – 2.4***	***1***
C	***3***	***0.33***	***9.1***	***3 – 6.6***	***1***
D	***3***	***0.7***	***4.3***	***5.1 – 10***	***1***
E	***3***	***1***	***3.0***	***7.6 – 10***	***1***
F	***10***	***3.33***	***3.0***	***68 – 86***	***1***
G	***3***	***0.3***	***10.0***	***3 – 6***	***2***
H	***3***	***0.5***	***6.0***	***3.5 – 7.5***	***2***
I	***3***	***0.7***	***4.3***	***5 – 8***	***2***
J	***3***	***0.9***	***3.3***	***6 – 10***	***2***
K	***6***	***0.5***	***12.0***	***7.4 – 12***	***2***
L	***6***	***0.7***	***8.6***	***10 – 15.5***	***2***
M	***6***	***0.9***	***6.7***	***12 – 17.5***	***2***
N	***3***	***1.63***	***1.84***	***6 – 9***	***3***
O	***3***	***1***	***3***	***3.5 – 7.5***	***3***
P	***3***	***0.7***	***4.3***	***4 – 6.5***	***3***
Q	***3***	***0.4***	***7.5***	***3 – 5.5***	***3***

Table 4.1. Investigated geometrical configurations

Various pressure and velocity conditions were investigated for each configuration by varying the flow rate and pressure in the tank to change the Reynolds number and the cavitation number.

However, due to the small scale of this experiment and the multiple geometrical scales involved, the characteristic lengths are not easy to determine, and the cavitation phenomenon is strongly influenced by pressure and water quality, resulting in a significant difference in cavitation number between different experimental groups even in the same controlled flow conditions. Therefore, other parameters are perhaps more applicable in this experiment than these two dimensionless parameters, such as volumetric flow rate, dimensionless cavitation length. Therefore, to obtain experimental data for more groups with different flow conditions, the main control parameters in the experiments were the volume flow rate and the upstream pressure of the plate jet, which has made the maximum throat velocity range around 5 to 30 m/s.

3. Evaluation techniques

3.1 Cavity length

Mean values and Root Mean Square of the gray level of images were calculated to evaluate cavity length and location of cloud separation in case of unsteady behavior. This method was proposed by Dular et al. 2004 in order to get an objective determination of the mean characteristics and oscillation frequencies of the cavitation area. It was shown in former study of M. Dular et al. that the mean value and standard deviation of gray level in the images do not change significantly (less than 2 %) when taking into account more than 50 images[7, 15]. However, after numerous tests, it has been discovered that due to ultra-high-speed photography is extremely sensitive to the lighting system and vibration. Moreover, as the flow rate increases, there is also a high probability of a thick layer of bubbles existing along the inner wall of the jet nozzle, which will create a brightness peak at the hole's edge (as shown in figure 4.7b red circle). This can cause significant errors in the measurement of the cavity length. Therefore, RMS cavity length is more effective and reliable. Therefore in the results that follow, the RMS cavitation length (take account 1000 images) is mainly used in this paper.

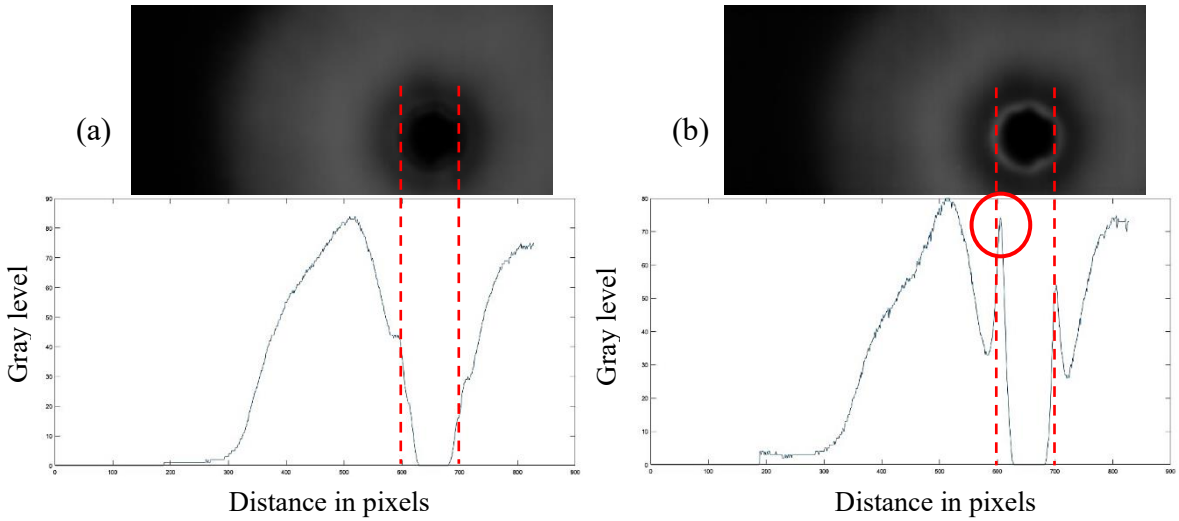

Figure 4.7. (a) RMS cavities overlap image and gray level curve schematics along radial distance, (b) Mean cavity overlap image and gray level curve schematics along radial distance

3.2 FFTs and Frequencies

Frequency characteristics are an important topic in cavitation research. The power spectral density function (PSD) was calculated by fast Fourier transform to determine the frequency of the sheet cavity oscillations (or possible cavitation cloud shedding). As a time-series vector for the FFT, the first region of interest (ROI) was selected, as shown in figure 4.8. A total of ten windows of interest (sample windows10×10 pixels) were selected in the radial direction away from the hole of the images. The sum of the gray-level values of the 100 pixels included in this region of interest was used for each vector element. For each flow condition, the record duration was at least 1s, so at least 10,000 elements length of the time series vector was used for each window FFT calculation.

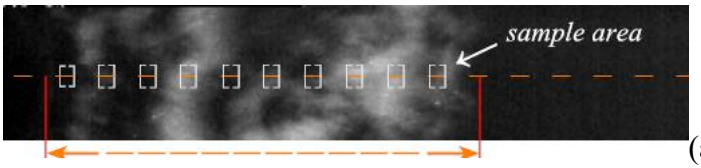

(a)

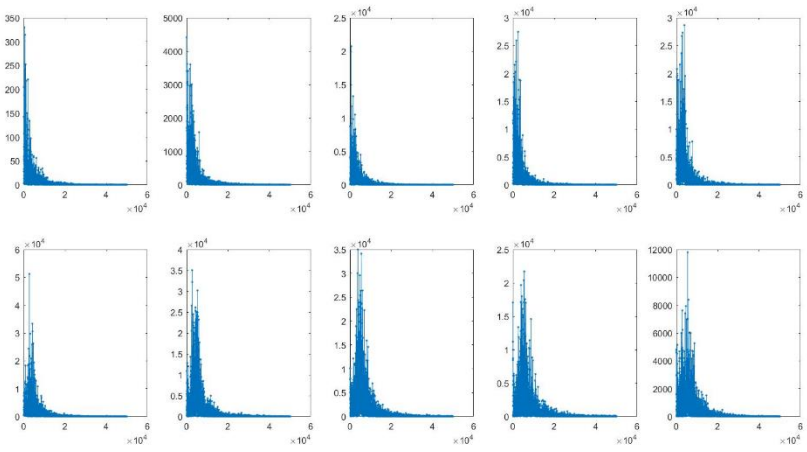

(b)

Figure 4.8. (a) FFT sample area schematic along radial direction (b) FFT results schematics for 10 ROIs

However, the lack of resolution and the problem of ultra-high-speed photography led to poor FFT results. Therefore, we have made several adjustments to the sampling window to improve FFT results. As shown in figure 4.9, the sample windows have been adjusted from 10×10 square to a 5×30 rectangle and then to a 5 pixels thickness ring size sample area, and the improvement of the results is also apparent. Also, the fitting equation tool was used to improve the experimental FFT results.

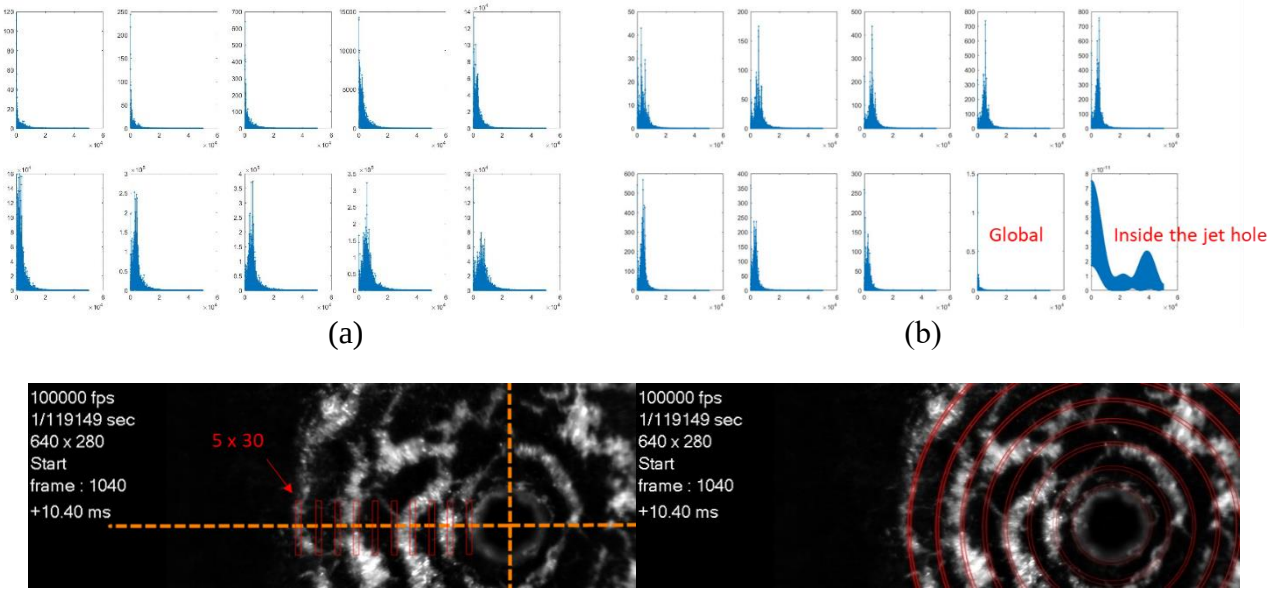

(a) (b)

Figure 4.9. Improved sample area schematic (a) 10 rectangle Windows and FFTs (b) 8 ring Windows and FFTs

In the third phase of the analysis of the experimental results, the frequency maps were also calculated by using a fitting equation curve to choose the highest peak automatically, which gives us a much more clear global view of the cavitation area (to reduce noise and computational effort, the FFT map is calculated from scaled original image using nearest-neighbor interpolation). However, as the fitting equation is doubtful and dubious in terms of accuracy, and some FFT figures or fitting equation curves have more than one peak or no peak at all, the fitting equation is only used as an assistant in selecting frequencies, and the experimental data afterward remains counted manually.

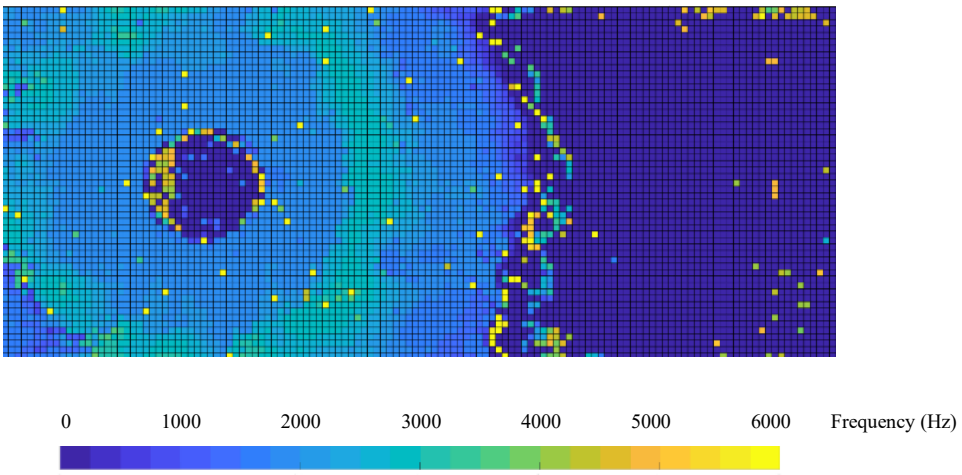

Figure 4.10. FFT map at 20% scaled for experiment at 3mm hole 0.7mm gap in the condition volume flow rate 5.79L/min

In order to describe this instability caused by cavitation more precise, the Str number was introduced for use and defined as the ratio of the inertial force of non-constant motion to the inertial force:

$$Str = \frac{L \cdot f}{v}$$

L is the characteristic length, f is the characteristic frequency, v is the characteristic velocity. The Strohal number is a similarity criterion modeled in non-constant hydrodynamic experiment. For periodic non-constant flows, it is a similarity criterion to characterize the periodicity of the flow[1, 3, 16].

3.3 PIV and velocity field

Velocity or Reynolds number is also an important parameter in evaluating cavitation flows. However, the small experimental scale and limited space resulted in a difficulty to measure the flow field velocities directly. Therefore initially, we used geometric structures to calculate theoretical flow velocities under the assumption of incompressible non-viscous flow. However, soon which has been discovered that this could lead to significant errors in the calculation of some of the characteristic parameters, such as Str number and Cavitation number, as the creation of cavitation bubbles and flow deflection angles could lead to sudden decreases in local velocity or sharp fluctuations, and the effect of the boundary layer could not be ignored at such small scales. Therefore, the PIV tool was introduced to calculate the velocity field, an open source code: MatPiv v.1.6.1 was used for the PIV process in this work[17].

Particle Image Velocimetry, also known as PIV, is a transient, multi-point, non-contact hydrodynamic velocimetry method developed in the late decades. The PIV technique is characterized by the fact that it goes beyond the limitations of single-point velocimetry (e.g., LDA) and can record the velocity distribution at a large number of spatial points in the same transient state, providing a relatively detailed and specific picture of the spatial structure of the flow field and the flow characteristics[18-21].

Unlike the standard PIV experiments, no tracer particles were used in this experiment. Another of the author's experiments shows that particles in the fluid significantly affect the cavitation phenomenon, particularly in small-scale experiments (laser bubble experiments which will not be discuss in this paper). The cloud of bubbles produced by cavitation is therefore used as a tracer particle to calculate the flow field, which is the most efficient way of measuring the flow field. However, it introduces an additional, more significant error than traditional PIV methods. After continuous debugging and image processing, the correlation value of the PIV was kept above 0.6（to reach the average standard level of the PIV experiment）. Uncertainty was calculated using the same methods as Khlifa1 in 2017, which resulted in over 80% of velocity results within 10% uncertainty both in x direction and y direction, as shown in figure 4.11[22, 23].

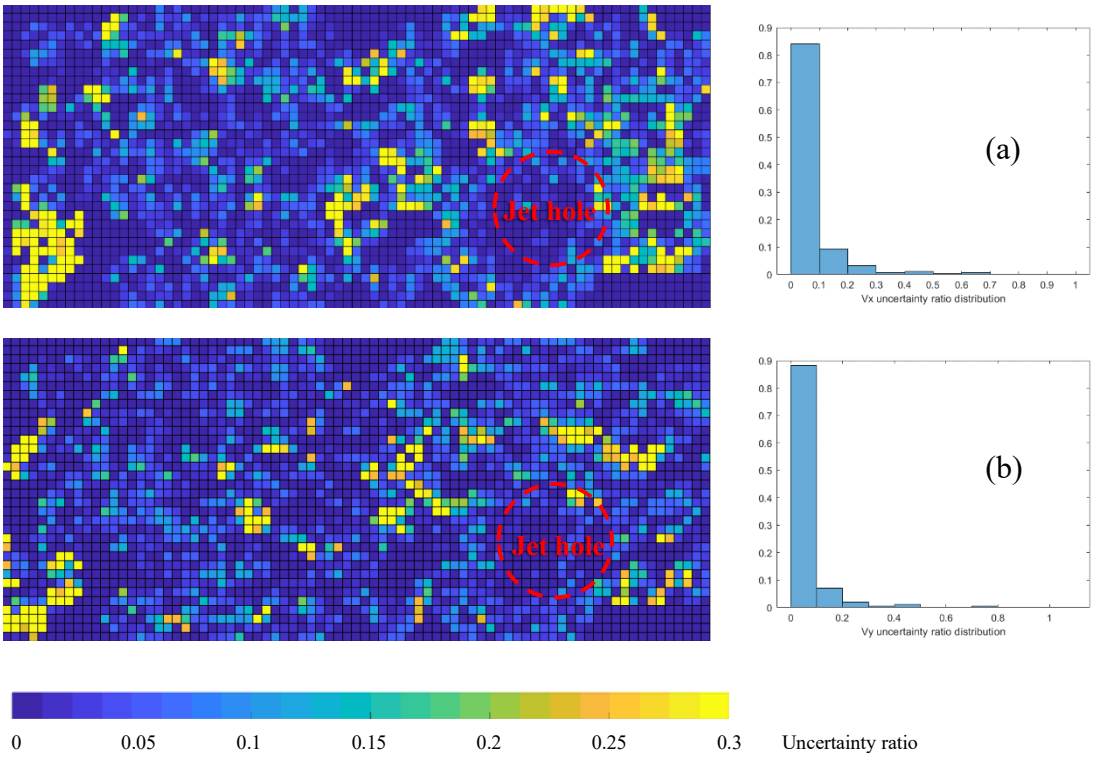

Figure 4.11. Velocity uncertainty ratio map(left) and distributions(right) for an instantaneous velocity field at 3mm hole 1.63mm gap in the flow rate 7.7L/min, (a) Vx, (b) Vy

Figure 4.12a shows the PIV mean velocity field of the 3mm diameter jet hole 1.63mm gap in the 7.7L/min flow rate test case. It can be seen that the velocity rises rapidly to 5-6m/s after the water starts to deflect 90 degrees out of the jet hole and then starts to decrease gradually as the radial direction continues to expand. The velocity profile is extracted along the radial direction, as shown in Figure 4.12b (This velocity will be used in subsequent chapters to calculate the local parameters). When the flow is assumed to be incompressible, the velocity profile for the ideal case of free flat plate expansion flow is known to be the dashed line shown in figure 4.12b, while the actual curve at this point is the solid red line, as obtained from the PIV velocity field. By comparing the difference between the two curves, the difference is a result of the generation of bubbles. A primary void factor can be calculated, as shown in figure 4.12c. It can be seen that near the hole, cavitation is briefly generated and then rapidly disappears and is rapidly generated again after a distance of 0.4 times the cavity length, which is consistent with the results of the cavitation bubble division previously observed through the gray level. Moreover, when considering this plat jet test section as a combination of several Venturi tubes, the results are in general agreement with the results of the two-

stage erosion distribution previously studied by Dr. Petkovšek and Professor Dular in 2013 of the cavitation erosion experiment on a thin aluminum foil[24]. However, it should be noted that the void factor here is a preliminary calculation and ignores the effect of viscosity and boundary layer, therefore the results are not accurate enough for quantitative analysis.

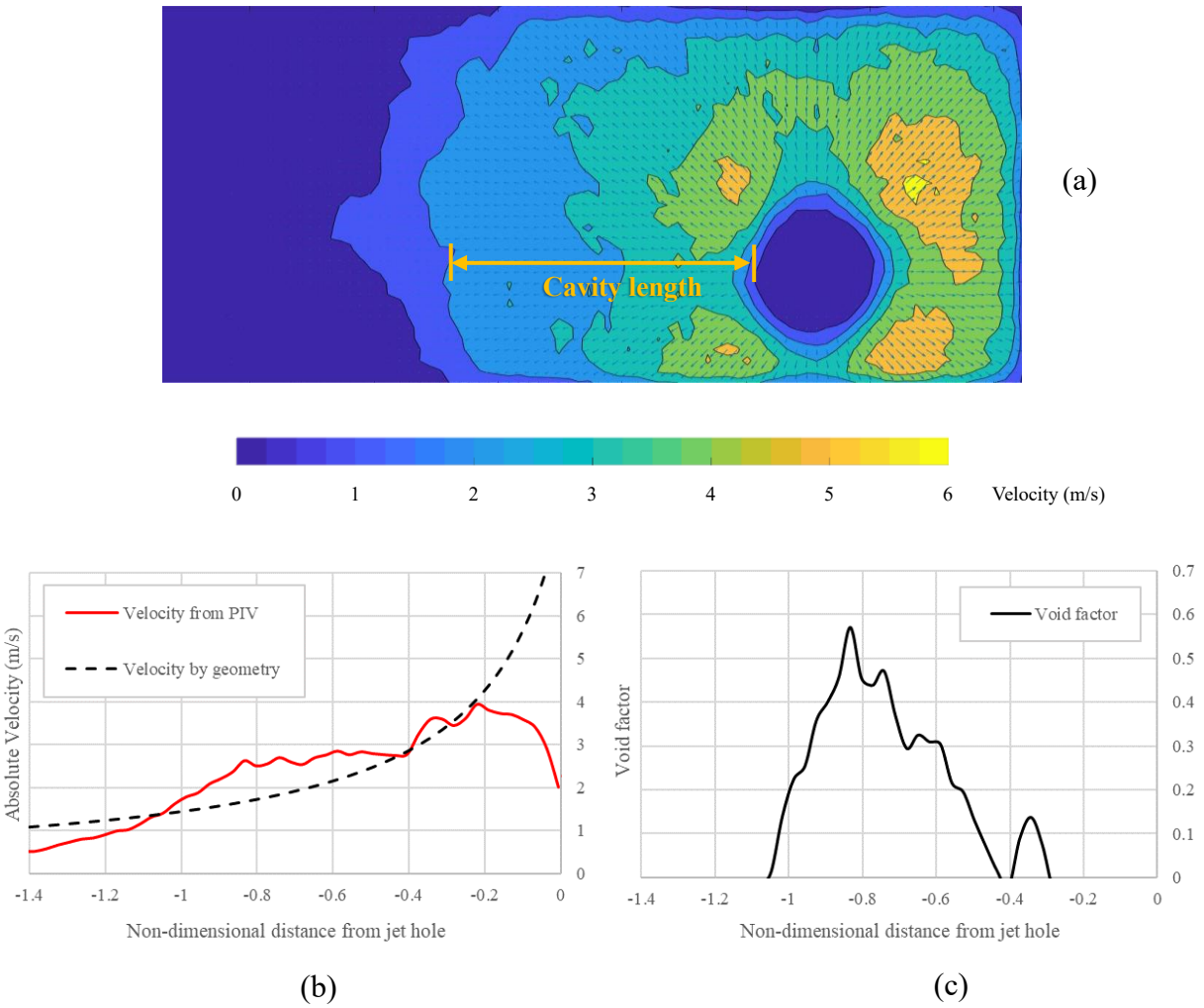

Figure 4.12. (a) Mean absolute velocity field from MatPiv (b) Velocity difference compare to theoretical calculation based on geometry（c）Void factor based on the difference between PIV velocity and geometry

4. Results & Discussions

Due to the massive volume of experimental data, and in order to clearly illustrate the main point of experiment results, this paper mainly focuses on and uses the experimental data of 3 mm diameter holes, supplemented by the data of 6mm holes and 10mm holes as a reference when necessary.

4.1.General behaviors.

As for the general external behavior, the three stages of the experiment show almost completely the same phenomena of cavitation. Cavitation generated around 0.1 mm to 0.5 mm distance from the edge of the jet hole. The cavitation cloud circle shows a periodic expansion and shrink in a set experimental condition (the gap, diameter, and volume flow rate).

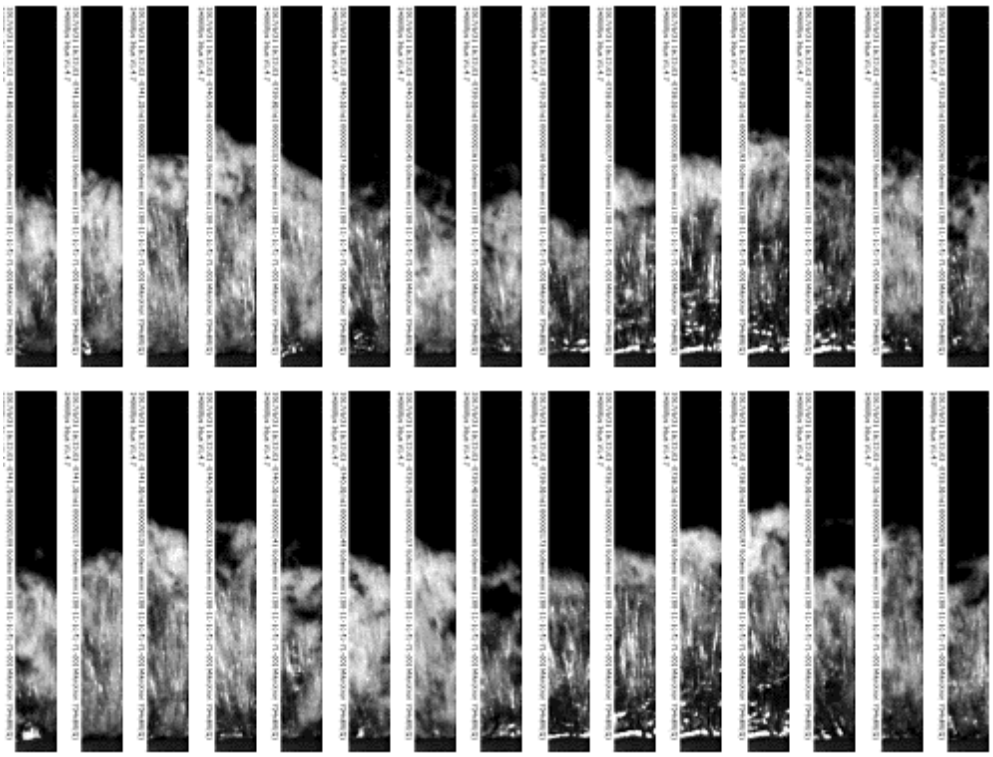

Figure 4.13. The cavitation cloud circle change of Group L at 6mm hole 0.7mm gap in the condition volume flow rate 14.15 L/min date set #2

In order to characterize the general behavior of the cavitation cloud circle in this experiment, we arranged those high-speed images of the cavitation cloud in a line every eight frames, which makes it straightforward to see that the cavitation cloud circle shows a periodic expansion and shrink. Figure

4.13 shows an example of cavitation cloud circle change of Group L. Cavity length generally increased with the increase of volume flow rate, as shown in figure 4.14.

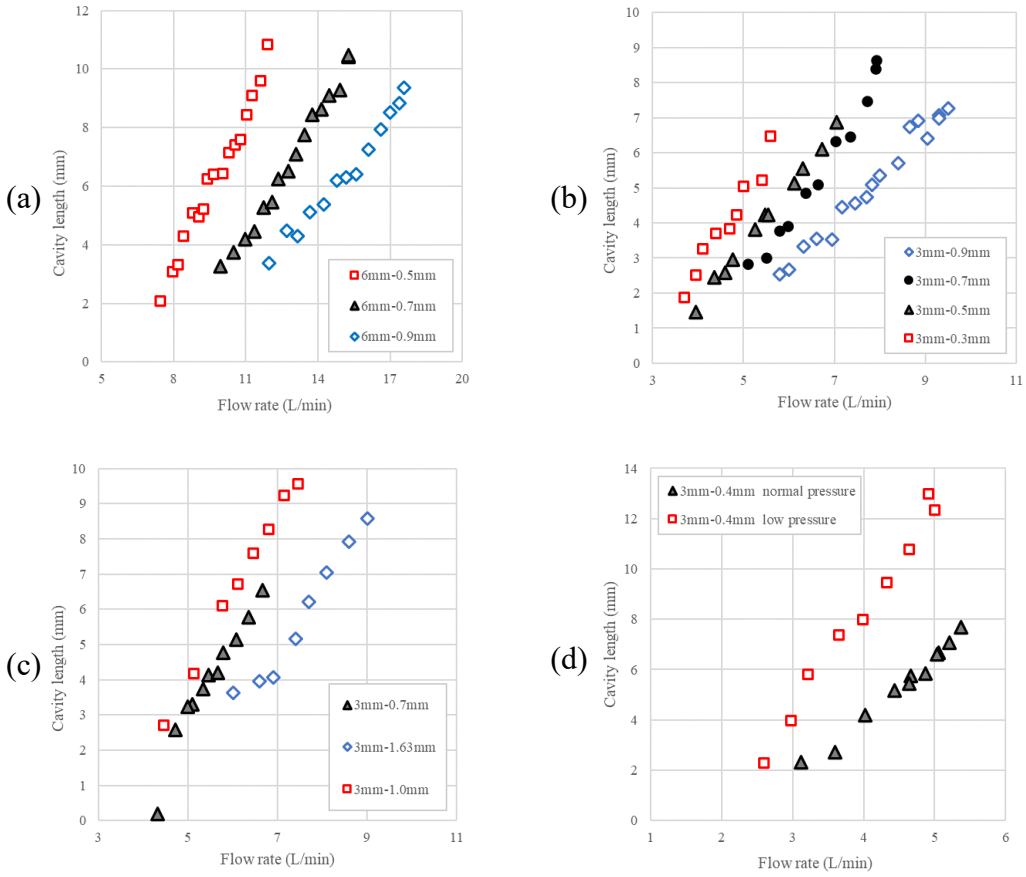

Figure 4.14. RMS cavity length at (a) 6mm hole in atmosphere pressure date set #2, (b) 3mm hole in atmosphere date set #2, (c) 3mm atmosphere higher resolution date set #3, (d) 3mm hole 0.4mm gap in low system pressure condition date set #3

The cavity length L and volume flow rate Q show a linear trend for all experiment sets. Even with the use of vacuum decreased the system's pressure and increased the cavity length without increasing flow rate, L and Q still show a kind of linear trend. Typically, the flow rate increases or decreases with the scale of the gap. However, it is also influenced by a combination of factors such as air temperature, atmosphere pressure, temperature, and humidity at the moment of the experiment. Besides, water quality (e.g., gas content) can also greatly influence the cavitation phenomenon leading to changes in volumetric flow rates, resulting in the situation shown in figure 4.14c. Moreover, during the experiment, which has been found that there does exist a maximum diameter related to the geometry parameters, which do not increase with volume flow rate, but many groups

of the experiment cannot reach the maximum diameter because of the limitation of the pump. The minimum volume flow rate for cavitation generation (cavitation start point) is increased with the increase of jet-hole diameter and increased with the increase of gap.

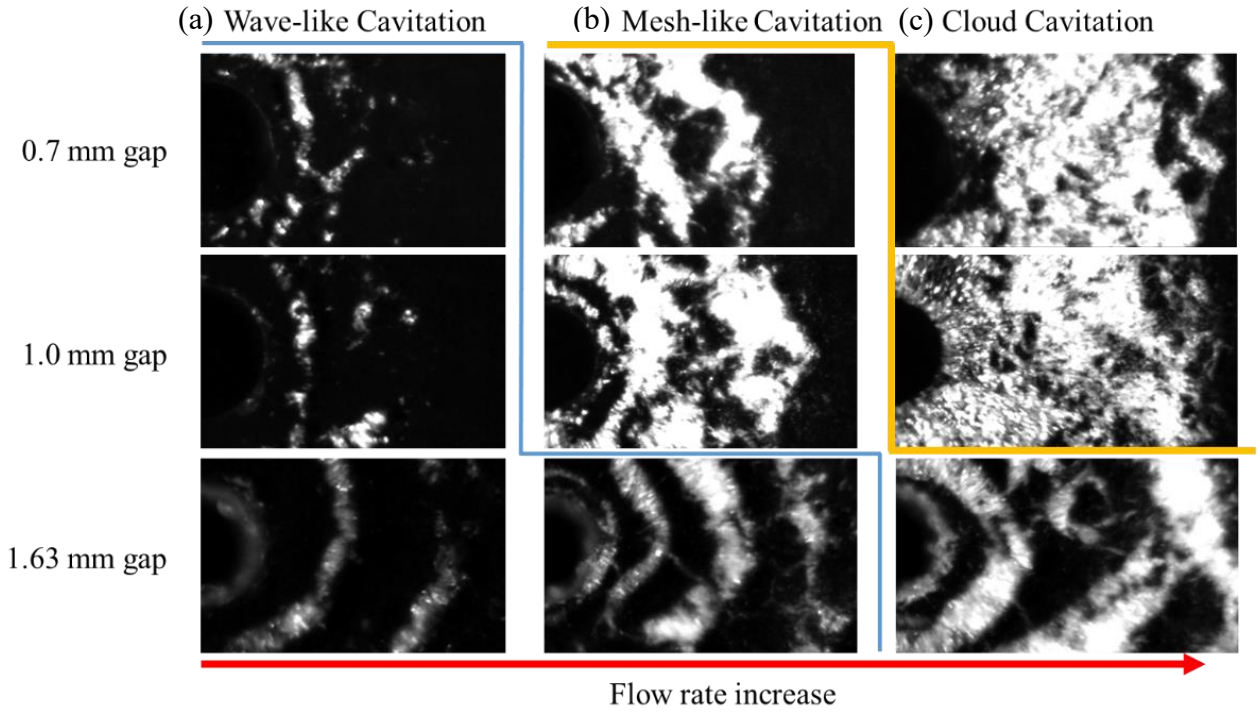

Figure 4.15. Cavitation structures in different geometries date set #3, (a) wave-like cavitation in large gap or small flow rate, (b) mesh-like cavitation in middle gap or middle flow rate, (c) could cavitation in small gap or large flow rate

As for different flow rate conditions, as shown in figure 4.15. At low flow rates or large gaps situations, cavitation takes the form of a self-rotating waveform, like ocean waves, which was called wave-like cavitation in this paper. As the flow rate increases or the gap decreases, several inverted waves begin to superimpose and cross, forming a mesh-like structure with larger pores, called mesh-like cavitation form. As the flow rate continuously increases or the gap decreases to a sufficiently small level, the cavitation wave disappears and breaks up into denser, symmetric mesh-like form or called cloud cavitation form. The cavitation bubbles in all three forms are too tinny, dense, and overlapping, which is not clear enough to recognize its structure. However, one thing is certain that the scale of the babble is smaller than 0.01mm (which is the maximum resolution of our experimental acquisition system).

4.2 FFTs and frequencies

According to previous studies, researchers usually assume that there is a dominant frequency of cavitation shedding, usually around a few hundred Hz7, so if we assume that the global frequency is this dominant frequency, and if we superimpose the FFT results of the ROIs, then we will get the data in figure 4.16.

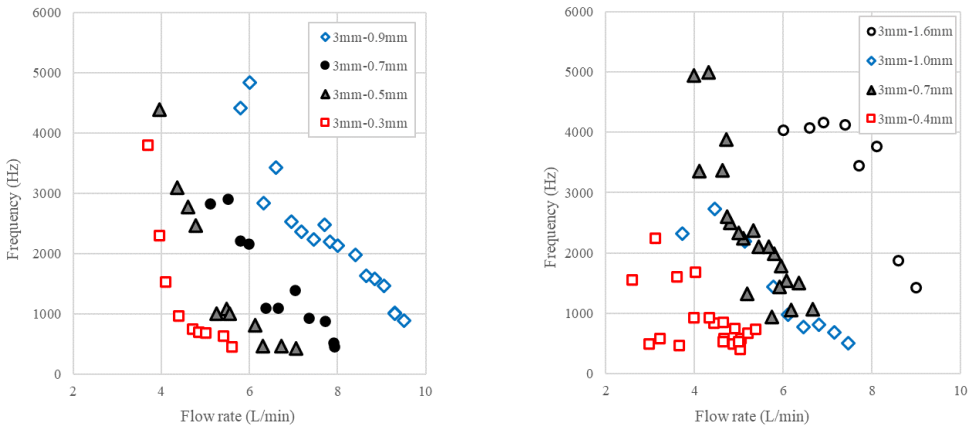

Figure 4.16. Cavitation frequency divisions in different geometries and flow conditions, data set #2(left), set #3(right)

As shown above, the frequency shows a downward trend with the increase of volume flow rate; however, the overall change pattern is still unclear between different geometries. The frequency division is mainly concentrated in three areas, lower frequency around 500 Hz to 1000 Hz, middle frequency about 2000 Hz to 3000 Hz, and higher frequency about 4000 Hz to 5000 Hz, so we introduce a non-dimensional length to make the results under different gaps tend to be uniform, which defined as:

$$L_{\_norm} = \frac{Cavity\ length}{gap}$$

The following figure 4.17 shows that in 0 to around 10 L, which means lower follow rate, with the increase of L, frequencies show a decreasing trend in these two different test sections. As the flow rate continues to increase, the frequency does not change as the cavity length continues to increase; instead, the frequency tends to a constant value around 500 Hz to 1000 Hz. Moreover, 6mm holes and 10mm holes experiments show the same distribution of the results while in different frequency levels.

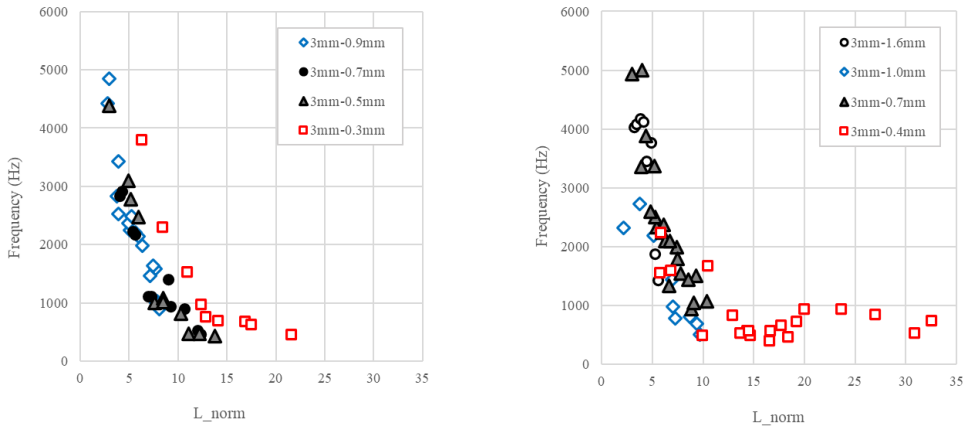

Figure 4.17. Cavitation frequency divisions in different geometries and flow conditions along L_norm, data set #2(left), set #3(right)

However, the cavitation frequency is not that simple. When superimposing the ROIs' FFTs, sometimes it is able to get a precise dominant main frequency with a single high peak. However, usually, we get a higher peak with several lower peaks near it or two or even three peaks at about the same level. After further analysis of the FFT of the ROIs, we found that the frequencies constantly change with position and even change abruptly, as shown in figure 4.18.

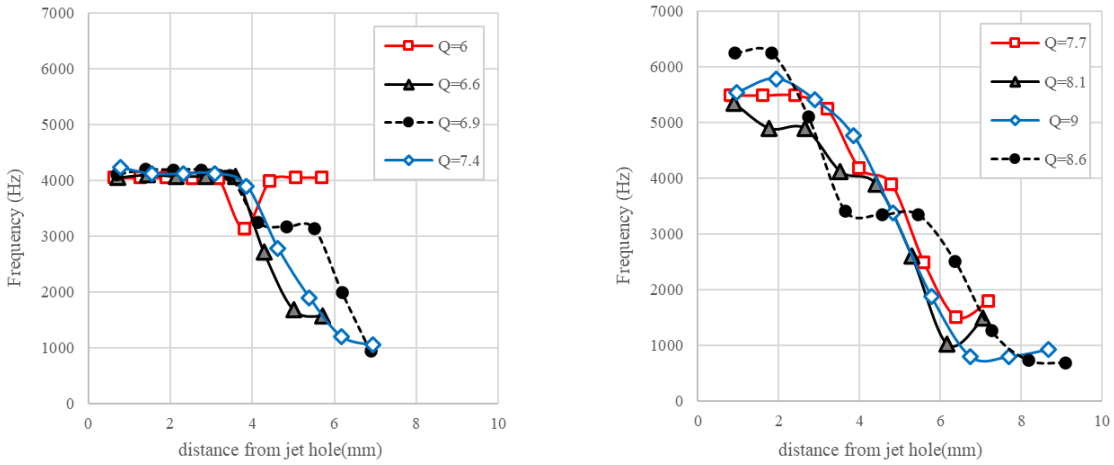

Figure 4.18. Cavitation frequency divisions in different flow rate(Q) at 3mm hole 1.63mm gap along non-dimensional distance, lower flow rate(left) and higher flow rate(right)

The figure above shows the frequency division for a 3mm diameter hole with a 1.63mm gap over the distance from the edge of jet hole. The frequencies show a significant three-band division,

with a high-frequency characteristic near the hole to the middle area, a sharp downward trend or even a sudden change at about the area of 4 to 6 mm, and a low-frequency characteristic near the end of the cavitation area. We, therefore, had to look further into the local problems of frequency.

However, the situation becomes different or more complex when the fitting equation curve is used to assist in the selection of the principal cavitation frequency, which is shown in the figures below, as for larger gap experiment (1.63mm gap), shown in figure 4.19. The external characteristics of cavitation in this set of experiments are all wave-like cavitation. There is a clear peak in the FFT plot far above the other frequencies, making it easy to get a precise main frequency with a clear change trend. In general, as in the previous manual selection of the main frequency of cavitation, the high-frequency band is located close to the jet hole and increases from 4000 Hz to around 6000 Hz gradually with increasing volume flow rate. As the transferring distance increases, the main frequency starts to decrease gradually to around 1000 Hz to 2000 Hz, which corresponds well to the dissipation and dispersion of energy as the cavitation ring diameter increases.

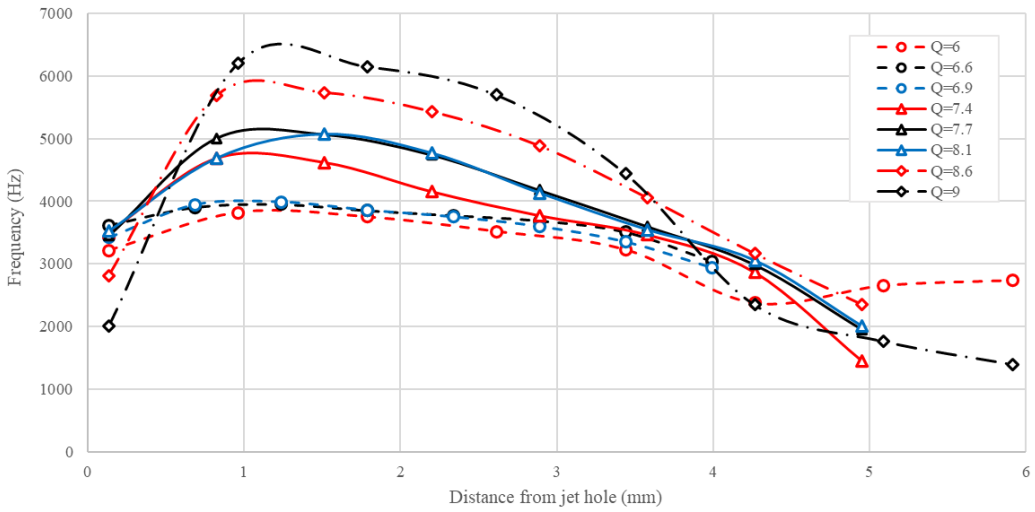

Figure 4.19. Fitting equation curve assisted cavitation dominant frequency in different flow rate(Q) at 3mm hole 1.63mm gap (date set #3) along the distance

For mesh-like cavitation, the situation is quite different. The continuous superimpose cross between the different cavitation waves makes obtaining a relatively constant and varying main frequency complicated. As shown in figure 4.20, as for the 1mm gap experiment, the cavitation frequencies show a clear triadic division, high frequency around 7000Hz, middle frequency around

3000 Hz, low frequency around 500 Hz to 1000 Hz. Moreover, the three cavitation frequencies seem to have little relationship with the flow rate and depend mainly on the geometrical parameters and the type of cavitation.

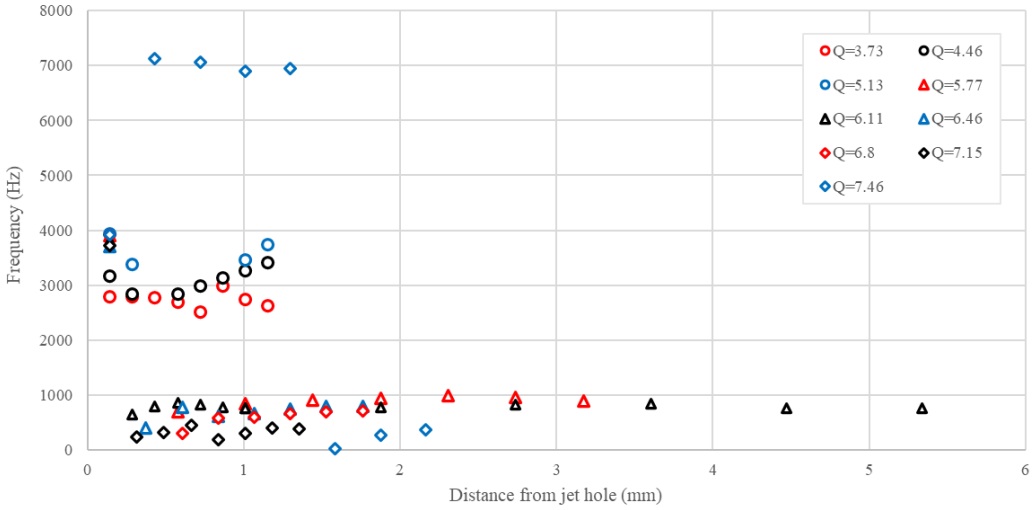

Figure 4.20. Fitting equation curve assisted cavitation dominant frequency in different flow rate(Q) at 3mm hole 1mm gap (date set #3) along the distance

Further complications occur in the case of cloud cavitation conditions. As for 0.7mm gap experiments, which are shown in figure 4.21(the data in the large graph results from the highest peak selected by the fitting equation curve, the data in the small graph inside is the data selected manually). Although the cavitation phenomenon shows a triadic division, the divisions in each segment are more dispersed and have a relatively certain tendency to change, which makes the general regularity more complex and difficult to identify.

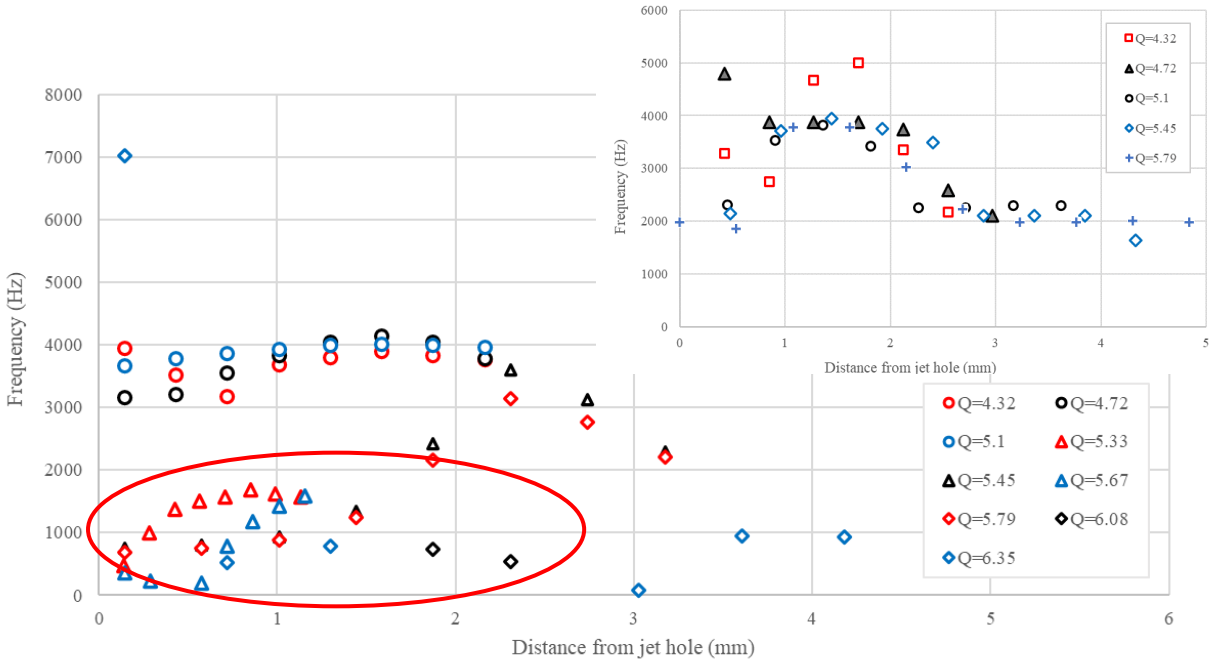

Figure 4.21. Fitting equation curve assisted cavitation dominant frequency in different flow rate(Q) at 3mm hole 0.7mm gap (date set #3) along the distance

A further study of the FFT diagram revealed the following figure 4.22. As we suspected, the cavitation frequencies show a ternary division (or multiple divisions). However, surprisingly, the three (or more) frequencies are present almost simultaneously in all the cavitation FFTs, but in different peaks value levels, so that different results and a more mixed frequency division are observed in figure 4.21. For example, as for the middle position (position 6) of the 3mm hole 0.7mm gap 5.79 L/min flow rate group experiment, the acquisition frequency is 100kfps with a resolution of 35.3 pixels per mm (ppm), three distinct frequencies 3790Hz 6250Hz and 750Hz are present simultaneously, but the highest peak is 3790Hz. These frequencies are widely present in most cavitation areas (position1 to 8). Moreover, a second middle frequency of around 1650Hz to 1870Hz was still captured at some other locations.

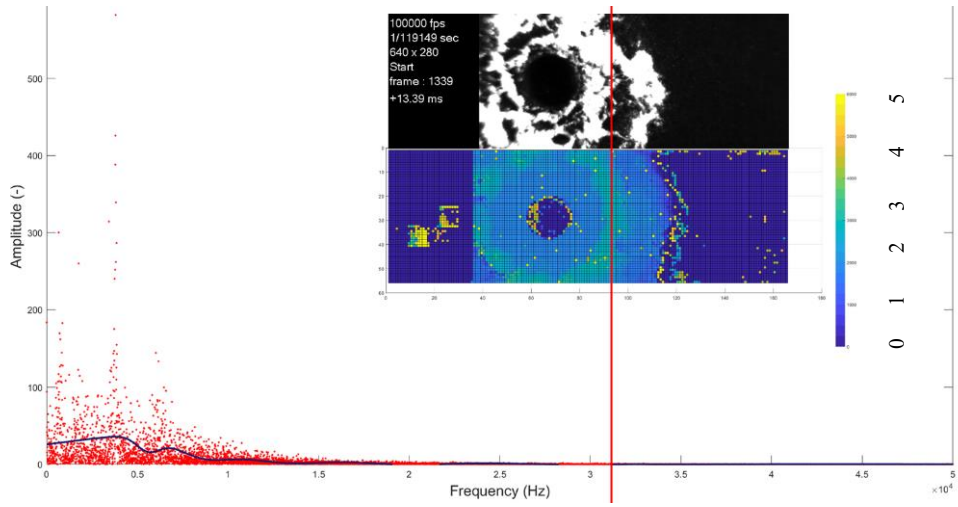

Figure 4.22. Cavitation FFT at 3mm hole 0.7mm gap 5.79L/min flow rate position 6(red line position) with fitting equation curve (blue curve) in higher resolution and acquisition frequency

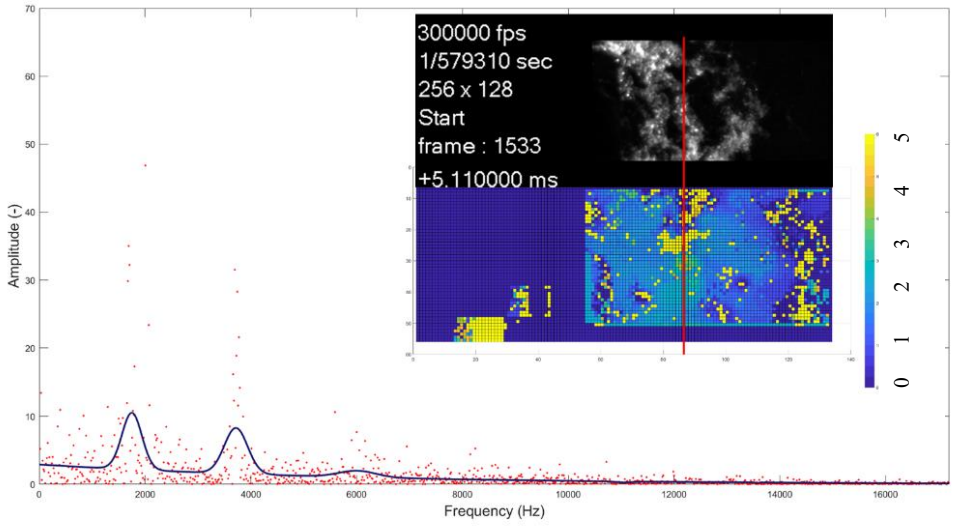

Figure 4.23. Cavitation FFT at 3mm hole 0.7mm gap 5.67L/min flow rate position 6(red line position) with fitting equation curve (blue curve) in highest resolution and acquisition frequency

However, when the resolution is further increased, the situation changes again slightly. As shown in figure 4.23, when the acquisition frequency reaches 300kfps with a resolution of 51 pixels per mm (ppm), more detailed clear images is captured, and the inner structure of the cavitation cloud, which initially appeared as a cloud of highlights, is captured, as shown in figure 4.23. The experimental conditions did not change significantly, except the flow rate was slightly reduced to 5.67 L/min. However, the cavitation frequencies became 3750Hz 6000Hz and 1760Hz, with the

highest peak at 1760Hz. A much lower frequency of around 880Hz was still captured at some other distance positions.

Based on further study of the original images, it has been found that for the 100kfps 5.79 L/min flow rate group experiment, as shown in figure 4.24, a more significant gap (or hole, as shown by the arrow) without cavitation bubbles was created in this region every 60 to 65 frames(see figure 4.24 a to g), corresponding to a frequency of approximately 1650Hz. In addition to these larger holes, several smaller holes around the jet nozzle are produced at higher frequencies, ranging from 3700hz to 6000hz, respectively.

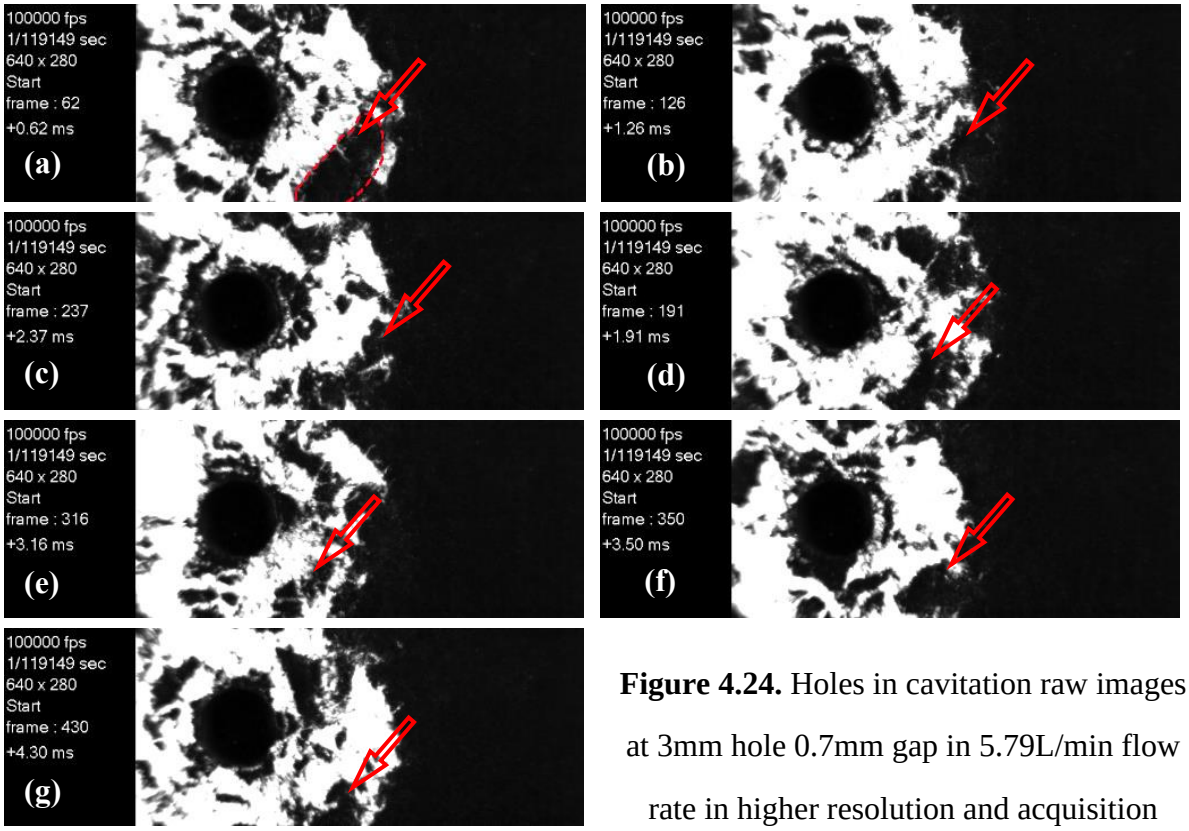

Figure 4.24. Holes in cavitation raw images at 3mm hole 0.7mm gap in 5.79L/min flow rate in higher resolution and acquisition frequency in different cavitation cycle

In order to investigate this phenomenon, a simpler experimental group with both wave-like and mesh-like characteristics cavitation was chosen to start with, 3mm hole 1.63 mm gap 9.0L/min flow rate, as shown in figure 4.25 below. At first, a roughly complete cavity wave is generated at the edge of the jet hole (red circle, a), and this occurs at a high frequency, typically generated once in 15 to 17 frames, reaching about 6,000 Hz (accompanied by incomplete half cavity waves generation in higher

frequency, occurred once in about 6 to 12 frames, at frequencies even up to 16,000 Hz). This cavity wave then expands, develops, and moves downstream, at which point a second cavity wave is generated at the edge of the jet hole (blue circle, b). As the previous wave expands and slows down on its way downstream, the second wave expands rapidly (c), catching up with the previous wave on its way downstream and starting to intertwine and merge (d), eventually forming a larger wave (green circle, e&f), which has a frequency of about 3000 Hz, called second-order wave. However, due to the influence of the higher frequency of half cavity waves that accompany occurred at the edge of the jet hole, the characteristic frequency of this large wave is nominally higher than expected 3000 Hz, which is located between 3500 Hz and 4000 Hz.

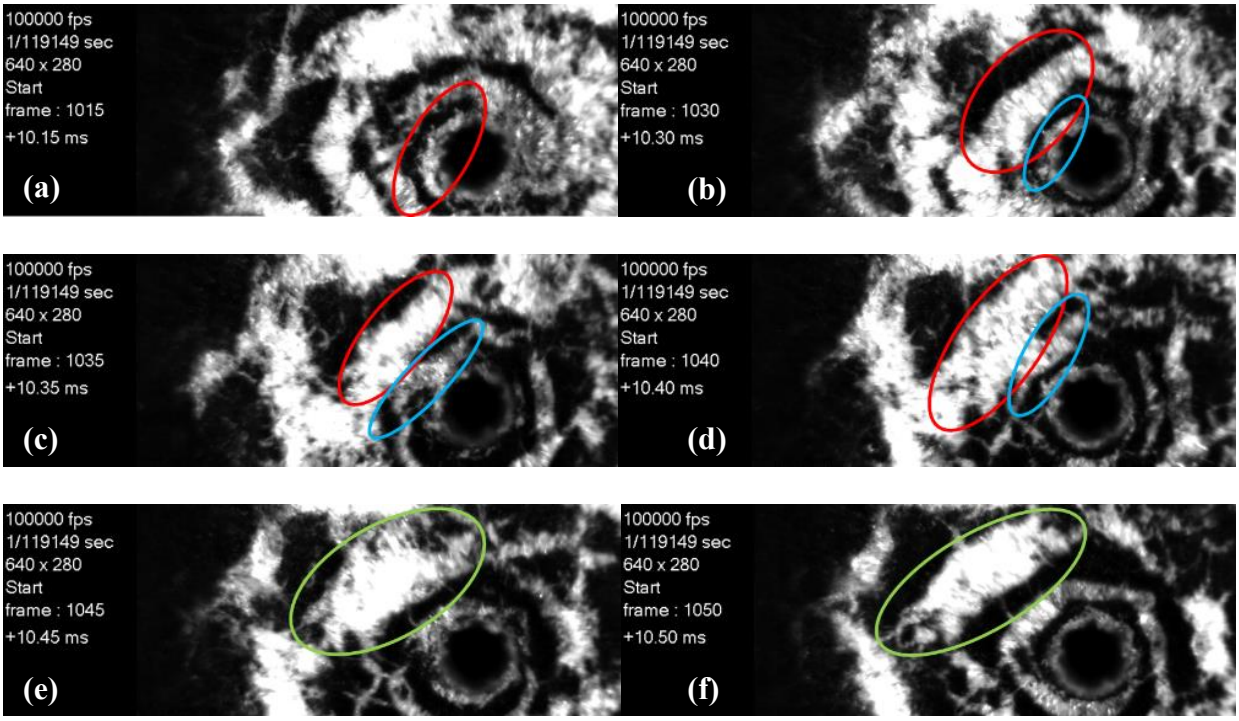

Figure 4.25. Waves in cavitation raw images at 3mm hole 1.63mm gap in 9.0L/min flow rate in higher resolution and acquisition frequency, first wave (red circle),second wave(blue circle), second-order wave(green circle)

According to the conclusions in the previous sections of this paper, when the gap decreases or the volume flow rate increases, the cavity wave will intertwine more quickly and develop into mesh-like cavitation. Therefore, it is reasonable to assume that as the two second-order waves continue to

intertwine and merge into an enormous third-order cavity wave, the frequency will continue to decrease to around 1750 Hz, with the subsequent fourth-order frequency being around 880 Hz. This also corresponds well to the FFTs of the previous experimental results.

Also, by analyzing the results at different resolutions, some groups cannot observe the cavitation's internal structure when the resolution and acquisition frequency is low. The frequencies can only be obtained by observing the hole without cavity bubble inside the mesh-like cavitation or cloud cavitation area, usually lower frequencies. More of the structure inside the cavitation cloud can be observed at higher resolutions, which is a mesh-like structure formed by the interweaving of many small cavity waves. Therefore, we can measure higher frequencies, which confirms this conjecture and explains the discrepancy between the FFT results obtained at different resolutions.

In summary, we, therefore, had to make a manual selection with the assistance of the fitting equation curve. The results of 3mm hole 0.7mm and 1mm gaps are shown in figure 4.26 below.

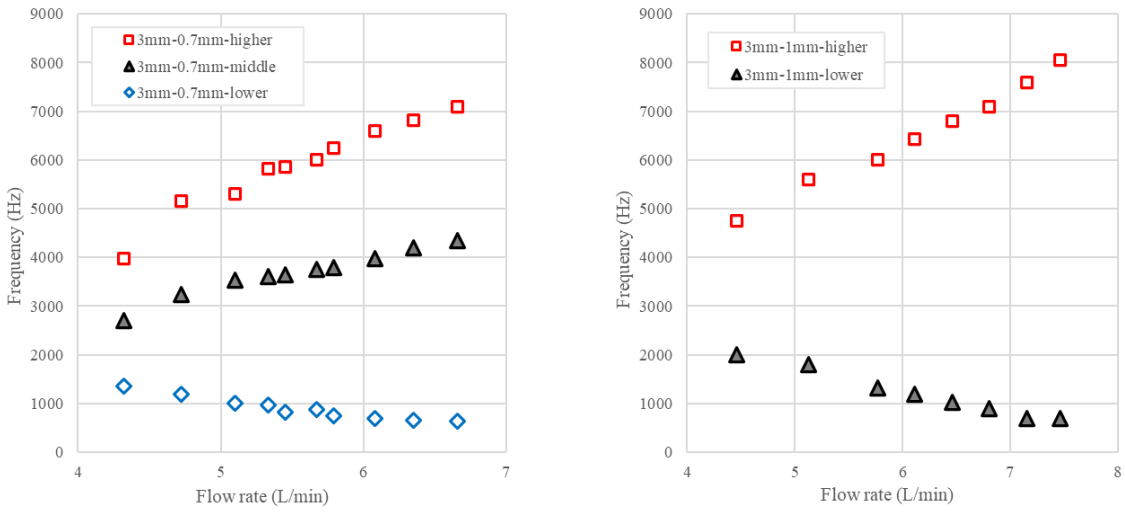

Figure 4.26. Different cavitation main frequency divisions in different flow rate at 3mm hole 0.7mm(left) and 1mm gap(right) date set #3

For 0.7mm gap results, as the experimental results are not all high resolution, most of the experimental results are still taken at 100kfps 35.3 ppm, so we do not get good results for the medium-low frequency around 1700Hz to 2000Hz. Therefore, three main frequencies have been obtained. The high frequencies are around 4000 to 7000hz and increase linearly with increasing of volume flow

rate. The medium frequency is between approximately 2500Hz and 4000Hz and also shows an increasing linear trend with the increase of volume flow rate. The lower frequencies are quite different, ranging from approximately 1300 Hz to 600 Hz, but decrease with the increase of volume flow rate, which may be related to various factors such as the boundary layer and turbulence and will not be discussed in this paper. For 1mm gap experiment results are similar to 0.7mm gap results, but only two distinct frequencies were detected. High frequencies show an increasing trend as well from around 4500 Hz to 8000Hz, and low frequencies show a decreasing trend from around 2000 Hz to 700 Hz.

4.3 Str and global parameters

With the frequency extraction analysis above and other relevant parameters, we can calculate a crucial non-dimension parameter in the cavitation phenomenon, the Strouhal number (Str).

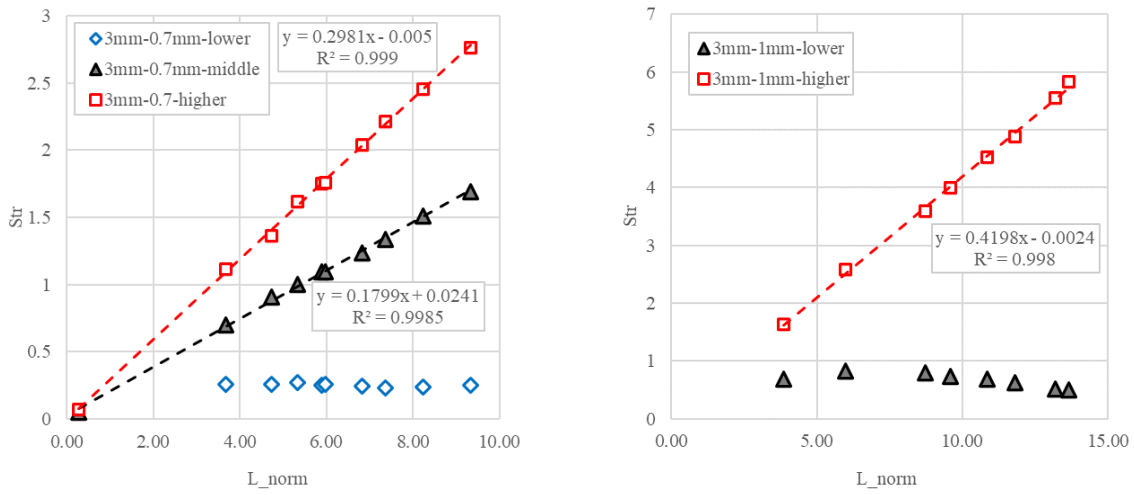

Figure 4.27. Different Str number divisions in different flow rate at 3mm hole 0.7mm(left) and 1mm gap(right) along L_norm date set #3

The trend of the Str number with non-dimensional length L_norm based on global frequencies is shown in Figure 4.27. The characteristic length is defined as the RMS cavity length, and the velocity is the theoretical velocity at the outlet of the jet hole edge based on the flow rate (because the flow is forced to turn 90 degrees at the edge, the PIV does not measure the actual velocity here due to the observation angle and inertia).

In this case, for the higher frequency selected as the main frequency for the Str number calculation, the Str number follows a more strictly linear relationship, increasing with L_norm, as shown in figure 4.27a, the R^2 is larger than 0.99. For the lower frequencies, the Str number tends to be a constant value that does not change with increasing volumetric flow or L_norm, which is approximately 0.25 for the smaller scale group of 0.7mm gap (shown in figure 4.28a below) and 0.65 for the larger scale group of 1mm gap. This, to some extent, corroborates the results of the previous work of M. Dular and O. Coutier-Delgosha at large scales (centimeter scale) in 2017 (unpublished). As at large scales, the researchers focused more on the detachment of the cavitation clouds and did not investigate much into the interior structures of the cavitation clouds, which is similar to the case of this experiment at low resolution, the low-frequency characteristics were mainly reflected. The information in the higher frequency bands could not be captured separately. However, when increasing the resolution and acquisition frequency to look at the detailed structure inside the cavitation cloud, the larger Str numbers vary linearly are obtained.

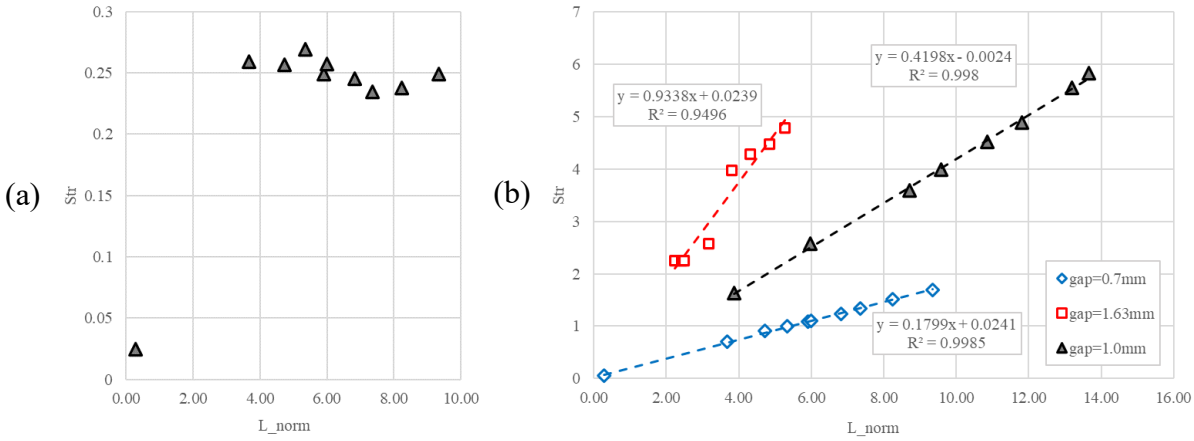

Figure 4.28. (a) Str number (with low frequency) divisions in different flow rate at 3mm hole 0.7mm gap (b) Str number (with dominant frequency) divisions in different flow rate at 3mm hole in different gaps date set #3

When comparing the most significant frequencies in the experimental groups with three different sizes of gap together (figure 4.28b), which has been found that the above pattern is generally consistent at the 3mm hole scale experiment and that the growth rate of Str number gradually increases with increasing gaps.

4.4 Velocity field and local Str number

When calculating the Str number based on local parameters, some problems arise in selecting the local parameters, especially in selecting the characteristic length.

With the experimental data from the previous section, we obtained 2 to 4 global frequencies in the cavitation area from the FFT plots at different locations with the assistance of the fitting equation curve. However, we also found some differences in the frequency characteristics at different locations. Although several global frequencies are present at most locations, there is a clear trend between the peaks corresponding to each frequency. The cavitation area's first half near the hole mainly shows higher frequency characteristics. In comparison, the area away from the hole shows lower frequency characteristics, as shown in figure 4.29 is the frequency division at a 3mm hole 1.63mm gap 7.7L/min flow rate.

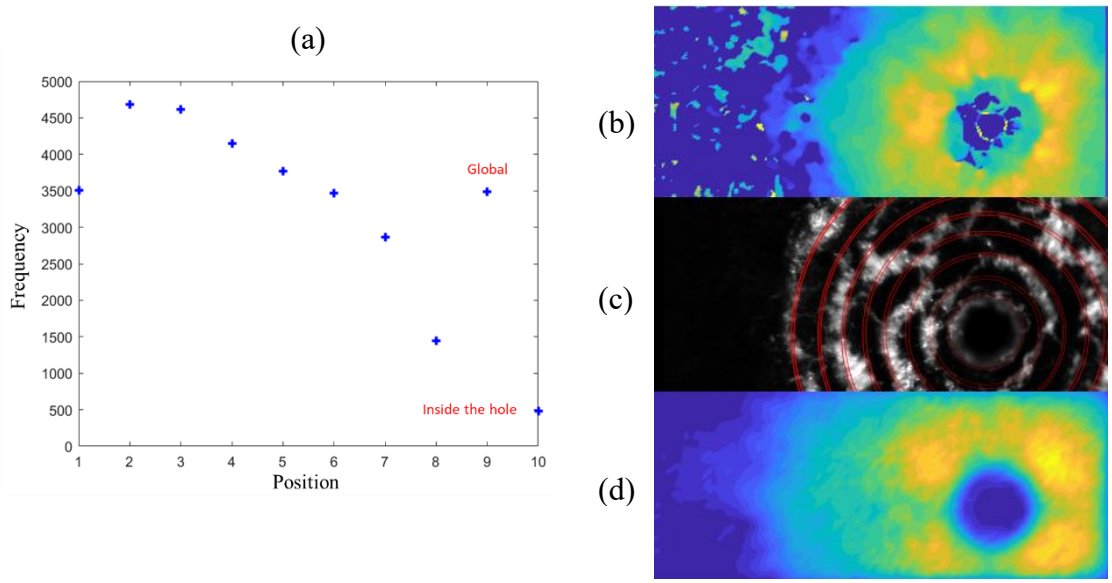

Figure 4.29. (a) Frequency divisions in 7.7L/min flow rate at 3mm hole 1.63mm gap for different sample positions (b) Frequency map
(c) Raw image and sample rings (d) Mean velocity field with matpiv

At the same time, with the PIV technique, the local velocity distribution was obtained, as shown in figure 4.29. The velocity shows a sharp increase in the area closely adjacent to the jet hole due to the 90-degree angle of deflection, and then reaches the maximum velocities at around 0.2 to 0.4 times of cavity length distance, and then gradually decreases. When comparing the velocity field (figure

4.29c) and the frequency field (figure 4.29a), it has been found that there is a considerable similarity between these two figures. Further calculations show that the correlation coefficient between this velocity field and frequency field is about 0.85, which is a strong correlation, so we can initially conclude that there is a positive correlation between the local cavitation frequency and the local velocity. Therefore, according to the definition of Str number, the value of Str number is more related to the selected characteristic length.

When choosing a global parameter such as RMS cavity length or mean cavity length, the Str number will inevitably be scattered because of the local parameter. Therefore, Gap was used as a reference characteristic length to verify our assumptions above. The results are shown in figure 4.30. The Str number value is significantly larger than normal at the area close to the jet hole due to the velocity measurement error. As moving away from the hole, the Str number gradually converges to 0.7 for a 0.7mm gap experiment, 1.0 for a 1mm gap, and 2 to 3 for a 1.63 mm gap experiment (this error is probably due to the difference between wave-like cavitation and cloud cavitation, resulting in a difference in the measured main The difference between wave-like cavitation and cloud cavitation may lead to a difference in the measured main frequencies, which will not be discussed any further).

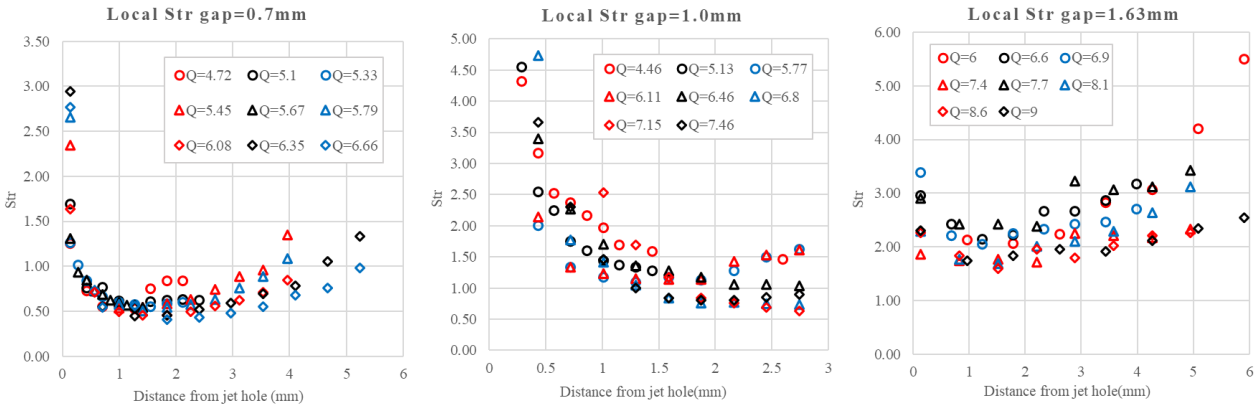

Figure 4.30. Local Str divisions along distance with a constant cavity length from the hole at 3mm hole in different gaps date set #3

5. Conclusions

This paper presents an in-depth study of cloud cavitation at small (sub-millimeter) scales through several stages of high-speed photographic plate jet experiments. Through continuous improvement of the experimental lightning system and acquisition system, the temporal and spatial resolution of the high-speed photography of the cavitation phenomenon was improved significantly, and the different characteristics of the cavitation in plate jets at different scales and different flow rates were observed. The cavitation phenomenon is described qualitatively, and cavity length has been analyzed quantitatively.

Moreover, the innovation of the post-processing method has led to the improvement of the frequency measurement and cavity length measurement accuracy and error reduction for the small-scale cavitation experiment. The radial distribution of cavitation frequencies along the flow direction is obtained by selecting different observation windows ROIs in the radial direction. It is observed that the cavitation characteristic frequencies are not identical and constant over the entire cavitation region but show a multi-order distribution. Subsequently, with the assistance of the fitting equation curve, a frequency map of the dominant frequency divisions of the plate jet cloud cavitation over the entire experimental observation area was made, giving an overall intuitive understanding of the frequency characteristics of the plate jet cavitation. The frequency map is more visually appealing and provides more general information about the flow field than taking a certain number of ROIs in the radial direction. However, it is more time-consuming for post-processing, and the uncertainty is more significant due to processing algorithms.

Further study of the FFTs of cavitation images in a particular region reveals that the frequency does not simply change with location but that multiple frequencies are superimposed on each other in the entire experimental observation area. It is only that different regions exhibit different dominant frequencies. Combining the cavity structure observed by high-speed photography, the cavity wave & hole theory is introduced. By separating and extracting these characteristic frequencies, the quantitative analysis of some groups of the experimental results is carried out, and characteristic frequency distribution curves are derived for the three most apparent global frequencies: the high, medium, and low frequencies. This frequency analysis method found that the global frequency varies

linearly with the flow rate. The Str number distribution curves were calculated for each of the three characteristic frequencies, and a highly linear distribution pattern was found. Moreover, the low-frequency Str numbers are stable in a specific interval, approximately 0.25 for the smaller scale group of 0.7mm gap and 0.65 for the larger scale group of 1mm gap experiments.

The local parameter was necessary due to a location-dependent variation in the dominant cavitation frequency. Thus, a PIV calculation was carried out to obtain a preliminary velocity field using the self-generated cloud cavitation bubbles as tracer particles. In addition, a preliminary local void factor division was derived by calculating the mean velocity field compared to the geometric structure. By comparing the velocity field with the frequency map, a high correlation and consistency distribution were found between them. The local Str number was calculated using this velocity field, combined with the local frequency obtained by the previous method. The distribution of the local Str number with distance from the hole was plotted and found to be a consistent approximate curve for different flow rates, with only a strong correlation with the geometry. However, due to the accuracy of the measurements, the quantitative analysis is not discussed any further in this paper but can be improved and investigated in future experiments.

References

[1] C.E. Brennen, Cavitation and Bubble Dynamics, Oxford University Press, Oxford, 1995.

[2] T.G. Leighton, The Acoustic Bubble, Academic Press, London, 1994.

[3] F.R. Young, Cavitation, McGraw-Hill, London, 1989.

[4] Milton S. Plesset& Andrea Prosperetti, Bubble Dynamics and Cavitation, Ann. Rev. Fluid Mech. 1977.9: 145-85

[5] H Fujita, H Perez-Meana, Cavitation Flow Simulation and Experiment Research in Inducer, IOS Press, Amsterdam, 2021

[6] J.R. Blake, J.M. Boulton-Stone, N.H. Thomas (Eds.), Bubble Dynamics and Interface Phenomena, Kluwer, Dordrecht, 1994.

[7] M. Dular, I. Khlifa, S. Fuzier, M. Adama Maiga & O. Coutier-Delgosha, Scale effect on unsteady cloud cavitation, Experiments in Fluids volume 53, pages1233–1250(2012)

[8] Roger E. A. Arndt, Cavitation in Fluid Machinery and Hydraulic Structures, Ann. Rev. Fluid Mech. 1981.13:273-328

[9] P. Veerabhadra Rao, Donald H.Buckley, Cavitation erosion size scale effects, Wear, Volume 96, Issue 3, 9 July 1984, Pages 239-253

[10] F. G. Hammitt (1975) Cavitation Damage Scale Effectsstate of Art Summarization, Journal of Hydraulic Research, 13:1, 1-17

[11] Keller, Andreas Peter (2001) Cavitation Scale Effects - Empirically Found Relations and the Correlation of Cavitation Number and Hydrodynamic Coefficients. In: CAV 2001: Fourth International Symposium on Cavitation, June 20-23, 2001, California Institute of Technology, Pasadena, CA USA. (Unpublished)

[12] Sascha Hilgenfeldt, Michael P. Brenner, Siegfried Grossmann and Detlef Lohse, Analysis of Rayleigh–Plesset dynamics for sonoluminescing bubbles, J Fluids Mech, Volume 365, 25 June 1998, pp.171-204

[13] Martin Petkovˇsek, Matevzˇ Dular, Simultaneous observation of cavitation structures and cavitation erosion, Wear 300(2013):55–64

[14] Coutier-Delgosha O, Stutz B, Vabre A, Legoupil S (2007) Analysis of cavitating flow structure

by experimental and numerical investigations. J Fluids Mech 578:171–222

[15] Dular M, Bachert B, Stoffel B, Sirok B (2004) Relationship between cavitation structures and cavitation damage. Wear 257:1176–1184

[16] Atsushi Okajima, Strouhal numbers of rectangular cylinders, J Fluids Mech (1982), vol:123, pp.379-398

[17] Sveen J K. An introduction to MatPIV v. 1.6. 1[J]. Preprint series. Mechanics and Applied Mathematics http://urn. nb. no/URN: NBN: no-23418, 2004.

[18] Foeth, E.J.; Van Doorne, C.W.H.; Van Terwisga, T.; Wieneke, B. Time resolved PIV and flow visualization of 3D sheet cavitation. Exp. Fluids 2006, 40, 503–513.

[19] Kravtsova, A.Y.; Markovich, D.M.; Pervunin, K.S.; Timoshevskiy, M.V.; Hanjalić, K. High-speed visualization and PIV measurements of cavitating flows around a semi-circular leading-edge flat plate and NACA0015 hydrofoil. Int. J. Multiph. Flow 2014, 60, 119–134.

[20] Vabre A, Gmar M, Lazaro D, Legoupil S, Coutier-Delgosha O, Dazin A, Lee WK, Fezzaa K (2009) Synchrotron ultra-fast X-ray imaging of a cavitating flow in a Venturi profile. Nucl Instrum Methods Phys Res A 607(1):215–217

[21] Coutier-Delgosha O, Vabre A, Hocevar M, Delion R, Dazin A, Lazaro D, Gmar M, Fezzaa K, Lee WK (2009) Local measurements in cavitating flow by ultra-fast x-ray imaging. In: Proceedings of FEDSM2009 2009 ASME fluids engineering division summer meeting, 2–5 Aug 2009, Vail, Colorado, USA

[22] Ilyass Khlifa1, Alexandre Vabre, Marko Hočevar, Kamel Fezzaa, Sylvie Fuzier1, Olivier Roussette, Olivier Coutier-Delgosha, Fast X-ray imaging of cavitating flows, Exp Fluids (2017) 58:157

[23] G Zhang, I Khlifa, O Coutier-Delgosha, Experimental investigation of internal two-phase flow structures and dynamics of quasi-stable sheet cavitation by fast synchrotron x-ray imaging, Physics of Fluids 32 (11), 113310

[24] Petkovšek M, Dular M. Simultaneous observation of cavitation structures and cavitation erosion[J]. Wear, 2013, 300(1-2): 55-64.

Chapter V. Conclusions, Contributions of this work and Perspectives for Future Work

During my 5-year Ph.D. work, I have mainly investigated small-scale cavitation by experimental methods. Unlike large scales, small-scale cavitation tends to be more complex and unstable, with higher stochasticity and lower reproducibility, to the extent that few previous researchers have ventured into or done quantitative studies.

Main contributions of this work：

1．Through the experimental method of high-speed PIV, the time-resolved cavitation flow field is measured, the whole process of cavitation inception to collapse is constructed, and some cavitation parameters are described quantitatively (such as cavity lengths and re-entrant velocities). A new model of cloud cavitation re-entrant jet is proposed, which provides a new idea for the in-depth study of the cloud cavitation mechanism. A new method for defining the non-dimensional cavitation number is proposed to improve the standardization and reproducibility of cavitation experiments.

2．The three-dimensional time-resolved cavitation flow field was captured using the high-speed 2D3C PIV technique, and the three-dimensional structure of venturi cloud cavitation was first obtained with an experimental method. The local details of the structure were described in detail. The side-jet phenomenon was discovered, its details and its subsidiary structures were analyzed, and a three-dimensional model of cloud cavitation was proposed, contributing to the study of the 3-dimensional structure of cavitation and providing a reference for subsequent simulations as well as experiments.

3．The scale effect has been investigated in depth through high-speed photography. Moreover, the cavitation of flat plate jets at sub-millimeter scales was observed with ultra-high-speed photographic captures over 200 kHz. The frequency is also quantified, and the local structure of the cavitation and the factors affecting the frequency are derived. The frequency characteristics of cavitation in small-scale clouds have been extensively investigated. Significant differences in

frequency due to different cavitation structures at different scales have been found, providing new ideas for further in-depth studies on frequency characteristics.

In the course of this investigation of the cavitation phenomena and the analysis of the frequencies, it was found that there was a large amount of noise in the experiment. This noise is present in a wide range of frequencies from a few Hz to several thousand Hz, and the frequency band division of the noise varies considerably for different flow conditions, z-directional positions, and experimental conditions stages. This is particularly the case for small cavitations.

Moreover, the same cavitation phenomenon in different location regions exhibits inconsistent dominant frequencies, or the existence of multiple different characteristic frequencies superimposed on each other at the exact location, as well as the lack of time scale resolution exposed due to the wide range of cavitation frequency divisions (from few Hz to several thousand Hz).

Furthermore, the existing image acquisition resolution does not allow the observation of individual bubbles produced by cloud cavitation at the micron scale. However, only macroscopic phenomena such as cavity clouds can be observed to derive macroscopic frequency (low frequency) and structural properties. In contrast, further studies of higher characteristic frequencies and the internal structural configuration of cloud cavitation are not possible.

Therefore, in future experimental studies, the following improvements can be made：

1. Increase the resolution or magnification of the split image and the frequency of image acquisition to investigate frequency characteristics and local structure further.
2. Use once formed sections to eliminate sideline-gap asymmetries and the resulting flow instability to make experimental data more reliable and reproducible.
3. Improve the surface roughness of the test section and the joint assembly gap to improve cavitation and reduce noise in the test data.
4. Use the new X-ray PIV technique to advance the visualization of cavitated internal structures.

CONCLUSION GENERALE ET PERSPECTIVES(FRANÇAIS)

Au cours de mes 5 années de doctorat, j'ai principalement étudié la cavitation des nuages à petite échelle (c'est-à-dire à l'échelle millimétrique et sub-millimétrique) par des méthodes expérimentales non intrusives basées sur l'image. Des caractéristiques spécifiques ont été détectées à petite échelle, comme des comportements plus complexes et instables, avec une plus grande stochasticité et une reproductibilité plus faible. Cependant, les principaux aspects de la cavitation des nuages, tels que le déversement périodique des nuages sous l'effet du jet rentrant sous la cavité, se sont révélés très similaires à ce qui est observé dans des sections d'essai plus grandes. Par conséquent, une étude détaillée des caractéristiques tridimensionnelles de l'écoulement, de la dynamique respective des deux phases, de la structure du jet rentrant, et des mécanismes d'instabilité de l'écoulement, a été étudiée en détail.

Principales contributions scientifiques de ce travail：

1. En utilisant la PIV stéréo à haute vitesse dans les deux phases, les champs de vitesse résolus dans le temps des flux de liquide et de bulles ont été mesurés avec une bonne précision, ce qui a permis de reconstruire et de discuter le cycle périodique de la cavitation du nuage et de discuter de la dynamique respective des deux phases. Un nouveau modèle du jet rentrant est proposé, qui explique le passage entre la cavitation à nuage unique et la cavitation à nuages multiples dans les écoulements habituels.

2. Le champ d'écoulement tridimensionnel a été capturé en appliquant une technique de PIV 2D3C à grande vitesse dans 9 plans longitudinaux verticaux, et la structure tridimensionnelle de l'écoulement pendant la cavitation en nuage a été décrite expérimentalement pour la première fois. Un fort jet latéral à l'extrémité amont de la cavité a été découvert, sa dynamique a été analysée en détail, et un modèle tridimensionnel de cavitation en nuage a été proposé.

3. L'effet d'échelle pour la cavitation nuageuse avec une dimension caractéristique comprise entre 0,3 mm et 3 mm a été étudié par photographie à grande vitesse à une fréquence allant jusqu'à 200 kHz. Les différentes fréquences liées à l'instabilité de la cavitation nuageuse ont été identifiées

et discutées, en fonction du modèle d'écoulement.

Au cours de cette étude de la cavitation des nuages, une analyse détaillée des fréquences locales obtenues à partir des signaux de vitesse a été menée. Bien qu'elle ait montré quelques caractéristiques intéressantes, comme la combinaison de la fréquence de déversement du nuage, la fréquence du jet rentrant (parfois plus élevée) et des fréquences beaucoup plus élevées à l'interface de la cavité, peut-être liées à des instabilités locales de Kelvin-Helmholtz, ce travail n'a pas été rapporté dans cette thèse, en raison de la grande quantité de bruit également détectée. Ce bruit est présent dans une large gamme de fréquences allant de quelques Hz à plusieurs milliers de Hz, et cette gamme varie considérablement avec les conditions d'écoulement, la position z de la feuille de lumière laser, et les conditions expérimentales en général. C'est particulièrement le cas pour les petites cavités en feuille. De plus, à certains endroits, non seulement une mais plusieurs fréquences dominantes ont été identifiées, ce qui a rendu l'analyse encore plus complexe.

Une autre limitation importante de ces expériences est liée à la résolution spatiale et temporelle : elle ne permet pas d'observer les bulles individuelles produites par la cavitation en nuage à l'échelle du micron. Par conséquent, seuls les phénomènes macroscopiques tels que les nuages de vapeur peuvent être observés et analysés pour en déduire certaines basses fréquences dominantes. Inversement, l'étude des fréquences caractéristiques plus élevées liées à la structure interne de la cavitation est plus difficile.

Par conséquent, dans les futures études expérimentales, les améliorations suivantes pourraient être apportées:

1. Augmenter la résolution ou le grossissement des images et la fréquence d'acquisition des images pour étudier davantage les caractéristiques de fréquence et la structure locale.

2. Améliorer les sections d'essai à petite échelle pour éviter la dissymétrie observée au chapitre 3, lors de l'étude des effets tridimensionnels.

3. Combiner la PIV avec l'imagerie par rayons X, qui peut être réalisée à une fréquence beaucoup plus élevée (270 000 Hz) et une meilleure résolution (micron) pour mieux caractériser la structure de

l'écoulement, et capturer les fluctuations caractéristiques à haute fréquence liées à la cavitation des nuages.

4. Utiliser la vélocimétrie par suivi de particules (PTV) en plus de la PIV, pour améliorer la résolution spatiale et obtenir des résultats plus précis au voisinage des parois. Cela permettra également de reconstruire le champ de pression avec une bonne précision, ce qui aidera grandement à la discussion des mécanismes de la cavitation des nuages.